# Satellite Infrared Limb Sounding of Ozone in the Upper Troposphere and Lower Stratosphere

A thesis submitted for the degree of Doctor of Philosophy

Mark Parrington
Linacre College, University of Oxford

Department of Physics
Atmospheric, Oceanic and Planetary Physics

Michaelmas term, 2003

# Satellite infrared limb sounding of ozone in the upper troposphere and lower stratosphere

Mark Parrington, Linacre College
Thesis submitted for the degree of Doctor of Philosophy at the
University of Oxford, Michaelmas term, 2003

Observations of ozone in the upper troposphere and lower stratosphere (UTLS) are central to our understanding of the chemical, dynamical and radiative properties of this important region of the Earth's atmosphere. Satellite infrared limb sounder measurements can provide the required global coverage at relatively high vertical resolution required due to steep vertical gradients of ozone in the UTLS. The scope of this thesis is to assess the potential for sounding ozone in the UTLS through retrievals from two such instruments: the Improved Stratospheric And Mesospheric Sounder (ISAMS) experiment, and the Michelson Interferometer for Passive Atmospheric Sounding (MIPAS).

The importance of ozone and the processes occurring in the UTLS, satellite observations of ozone, a description of the ISAMS and MIPAS instruments, and the aspects of retrieval theory used in this thesis is provided in chapters 1 to 4 respectively. Chapter 5 presents ozone retrievals in the Arctic lower stratosphere from ISAMS data during the 1991-92 winter, compared to MLS and ozonesonde data from the same period. The results show that, despite the limitations of the ISAMS radiometer data, there is information on ozone in the lower stratosphere which could be further exploitable with an instrument such as MIPAS.

Simulated ozone retrievals from MIPAS are performed with the RAL radiative transfer model (FM2D), the performance of which is validated in 1-D and 2-D against the Oxford University RFM in chapter 6, with results showing good agreement between the two models. One of the most efficient ways for retrieving information from the MIPAS data is through the selection of microwindows using the concept of information content, and chapter 7 shows how retrievals in the UTLS can be improved by selecting microwindows that only span that altitude range. The optimum microwindows for the ozone in the UTLS are shown to be close to the centres of the ozone fundamental bands at 701 and 1042cm$^{-1}$. One of the most significant sources of systematic uncertainty in UTLS ozone retrievals is shown to be neglect of horizontal temperature gradients of order 1 K per 100 km along the instrument line-of-sight.

Chapter 8 presents results for tomographic (2-D) retrievals from measurements in the MIPAS special observing mode S6. The results show that improvements over 1-D are made in the retrieval random errors if the horizontal spacing of the retrieval grid is sufficiently wide enough. Retrievals of horizontal structure in the atmosphere with a 2-D non-linear retrieval are shown to be an exciting prospect for the future.

# Acknowledgements

First and foremost I would like to thank my supervisors Drs Clive Rodgers, Brian Kerridge and John Remedios for their support, encouragement and enthusiasm throughout the duration of this research. I am indebted to Professor Fred Taylor, for allowing me the opportunity to read for this doctorate, and the Natural Environment Research Council and Rutherford Appleton Laboratory for their financial support in the first three years.

A huge debt of gratitude is owed to Jolyon Reburn, Victoria Jay, Richard Siddans and Barry Latter, in the Remote Sensing Group at the Rutherford Appleton Laboratory, without whose expertise and advice much of the work presented in this thesis would not have been possible. Thanks are also due to various members of the Earth Observation Data Group in AOPP for help and advice in understanding atmospheric remote sounding and retrieval theory.

Many other people, in Oxford and elsewhere, have made some contribution to this work one way or another, however profound, over the last few years and to acknowledge them all would be a thesis in itself. In particular, thanks have to go to the various people I have known through Linacre College, OUCCC and the Mansfield Road Runners for providing more than enough distractions from retrieval theory.

Finally, thanks go to my family without whose love and support none of this would have been possible in the first place.

# Contents

# Chapter 1

# Ozone in the Upper Troposphere and Lower Stratosphere

## 1.1 Introduction

Life on Earth is sustainable due to a relatively thin atmosphere (approximately 120 km thick) of nitrogen (78%), oxygen (21%), argon (0.93%), carbon dioxide (0.036%) and a large number of other, less abundant, trace gases (of which ozone and water vapour are two of the most important). This atmosphere regulates the surface temperature of the Earth and provides some protection from the space environment through which the planet moves. The atmosphere is divided into layers based on the distribution of its vertical temperature structure as shown in Figure 1.1. The layer of the atmosphere closest to the surface is the troposphere, extending to an altitude of between 8 and 17 km depending on latitude and season. The temperature decreases with altitude in the troposphere due to solar radiation at visible wavelengths being absorbed by the surface and re-emitted at infrared wavelengths, thus heating the atmosphere from below. Above the troposphere, the stratosphere extends to approximately 50 km and the temperature increases

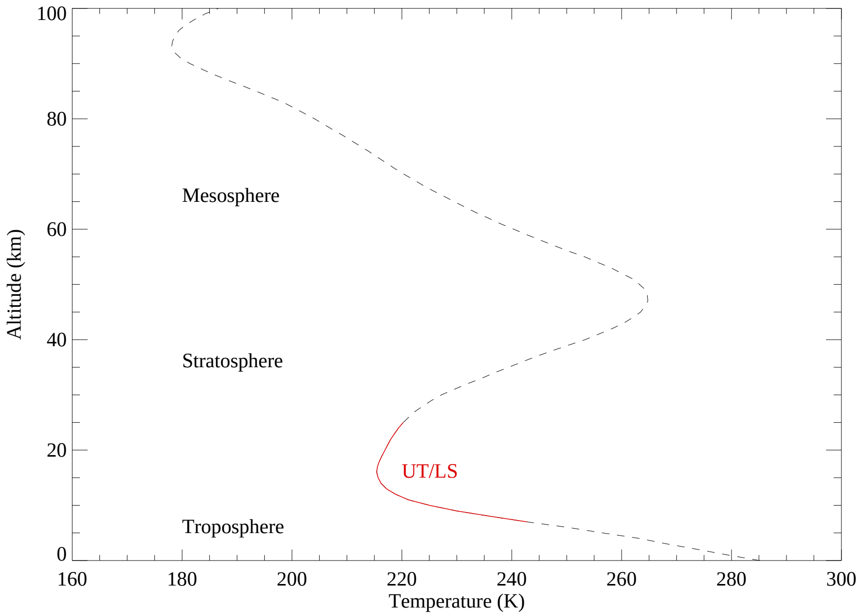

Figure 1.1: Vertical temperature structure of the Earth's atmosphere typical of mid-latitudes. The red section of the profile shows the altitude range of the UTLS region.

due to the dissociation of molecular oxygen and ozone by solar radiation at ultraviolet wavelengths. Above the stratosphere, and extending to approximately 90 km, is the mesosphere where the temperature decreases again due to radiative cooling by carbon dioxide.

The upper troposphere and lower stratosphere (UTLS) region of the atmosphere can be defined as a layer that extends across the tropopause between approximately 7 and 25 km, shown by the red section of the temperature profile in Figure 1.1. The UTLS is characterised by steep vertical gradients in temperature and concentrations of a variety of trace gases (especially ozone and water vapour). Ozone is one of the most important trace gases in the UTLS as decreases in the abundance of ozone in the lower stratosphere leads to increased levels of ultraviolet radiation at the Earth's surface, while in the upper troposphere, increased levels of ozone have implications for global warming due to strong absorption/emission lines in the infrared.

## 1.2 The Role of Ozone in the UTLS

Most of the ozone in the atmosphere is located in a stratospheric layer, between approximately 20 and 50 km, formed by the photolysis of molecular oxygen at ultraviolet wavelengths. The ozone layer is especially important as it attenuates the amount of this high energy radiation from reaching the Earth's surface environment where it is damaging to living cells in plants and animals. In the troposphere, ozone is important for two reasons: (i) it is a greenhouse gas, due to strong emission lines in the infrared, and (ii) it controls the chemistry of the troposphere through the formation of hydroxyl radicals in the presence of water vapour. Figure 1.2 shows monthly zonal mean ozone values (ppmv) for December 1992 (left-hand plot) and May 1993 (right-hand plot) as a function of pressure and latitude.

Observed negative trends in stratospheric ozone since the 1970s are of concern as they directly correlate with observed mean increases in the UV flux at the surface. Global mean total column ozone between 1997 and 2001 was approximately 3% below pre-1980 average values (WMO, 2003). The trends in total column ozone between the Northern Hemisphere (NH) and Southen Hemisphere (SH) have differences depending on latitude and season. At NH and SH mid-latitudes (35° to 60°) the average total column ozone decreases (between 1997 and 2001) are approximately 3% and 6% relative to pre-1980. In the NH, larger ozone decreases are observed during winter-spring (approximately 4%) whereas summer-autumn decreases are about half as large. In the SH, long-term ozone decreases are of a similar magnitude at all seasons (approximately 6%) (WMO, 2003).

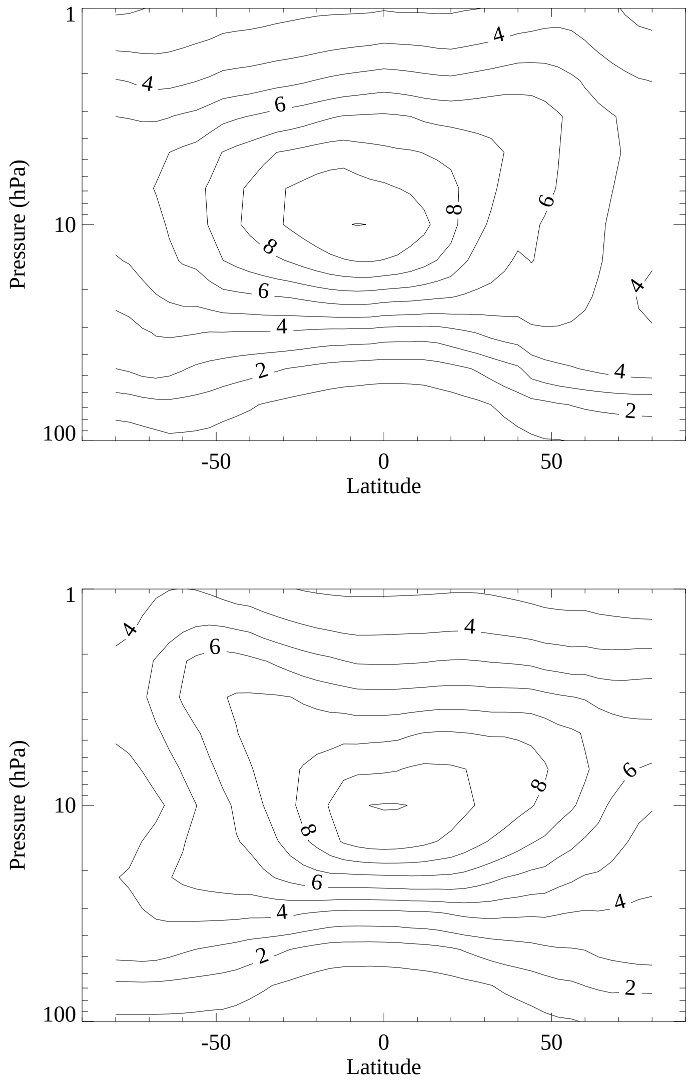

Figure 1.2: Monthly zonal mean distribution of ozone (ppmv) for December 1992 (upper plot) and May 1993 (lower plot). These zonal means are derived from measurements made by the HALOE and MLS instruments on the NASA UARS platform (see section 2.3) and are available from the UARS Reference Atmosphere Project (Wang et al., 1999).

Figure 1.3 shows the negative trend in stratospheric ozone (percent per decade) derived, as a function of altitude, from the SAGE I (1979 to 1981) and SAGE II (1984 to 2000) datasets (WMO, 2003). This shows that between 1979 and 2000, there has been between a -1 and -3% per decade significant trend in ozone in the lower stratosphere (20 to 25 km) at mid-latitudes. Ozonesonde measurements at NH mid-latitudes show a continuous decrease in ozone between 20 and 27 km during the period 1980 to 2000. Figure 1.4 shows the annual mean trends in ozone profiles calculated for eight NH ozonesonde stations (located between 36°N and 59°N) for two time periods (1980 to 1996 and 1980 to 2000). In the UTLS region, the trend has a peak of almost -10% per decade at about 14 km in the period 1980 to 1996 (with a peak of approximately 5% per decade over the longer period).

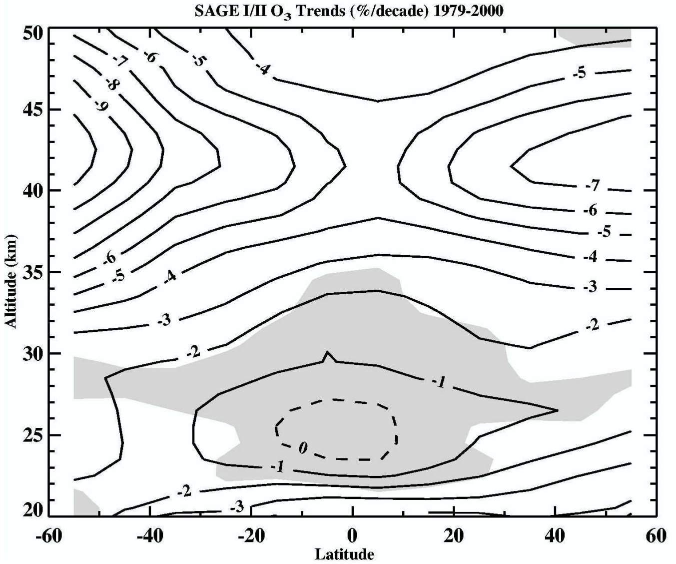

Figure 1.3: Meridional cross-section of ozone profile trends derived from the combined SAGE I and SAGE II datasets. The trends are calculated as percent per decade relative to the overall time average. The shaded region indicates that the trends are statistically insignificant at the $2\sigma$ (95%) level (WMO, 2003).

Trends in the abundance of tropospheric ozone are difficult to quantify as suitably continuous observations are only available since 1970 from ozonesondes launched at nine different sites. No trends are observable in the ozonesonde record from 1980 to 1996, although all stations show an increase from 1970 to 1996 (Logan et al., 1999). Figure 1.5 shows the trend in tropospheric ozone abundance in ppb from 1970 to 1996. The increase in the ozone abundance between 1970 and 1996 is approximately 4 ppb.

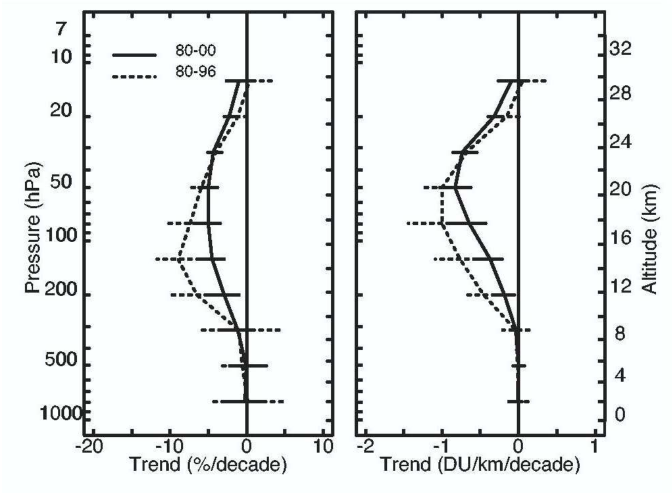

Figure 1.4: Annual mean trends in ozone profiles at eight NH ozonesonde stations located between 39 and 56° for time periods 1980 to 1996 and 1980 to 2000. The trends are shown as percent per decade (left) and (DU/km/decade) (right). The error bars show the $2\sigma$ (WMO, 2003).

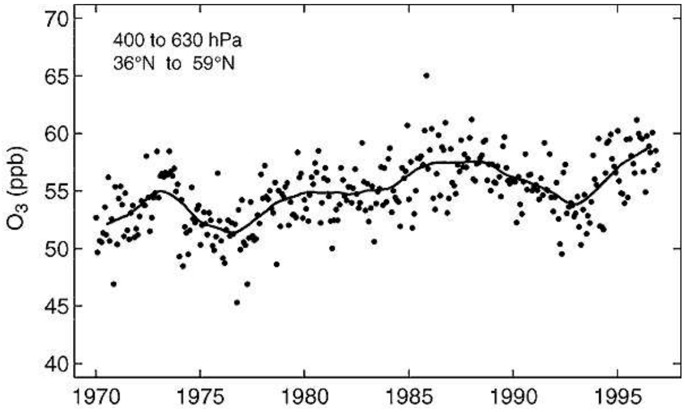

Figure 1.5: The abundance of mid-tropospheric ozone (ppb) in Northern mid-latitudes (36°N to 59°N) for the years 1970 to 1996. Observations between 630 and 400 hPa are averaged from nine ozonesonde stations, following the analysis of (Logan et al., 1999). Values are derived from the residuals of the trend fit with the trend added back to allow for discontinuities in the instruments. Monthly data (points) are shown with a smoothed 12-month running mean (solid line) (IPCC, 2001).

### 1.2.1 Chemistry

#### Stratospheric ozone chemistry

In the stratosphere, ozone ($O_3$) is chemically produced in the gas phase through the photolysis of molecular oxygen ($O_2$), at wavelengths less than 242 nm, via reaction (1.1) to produce atomic oxygen which can react with other oxygen molecules through reaction (1.2). Ozone is then destroyed through photolysis (reaction (1.3)), at wavelengths between 300 and 325 nm, and also through reaction with atomic oxygen (reaction (1.4)).

$$\mathrm{O_2} + h\nu \rightarrow \mathrm{2O} \tag{1.1}$$

$$\mathrm{O_2 + O + M} \rightarrow \mathrm{O_3 + M} \tag{1.2}$$

$$\mathrm{O_3} + h\nu \rightarrow \mathrm{O_2 + O} \tag{1.3}$$

$$\mathrm{O_3 + O} \rightarrow \mathrm{2O_2} \tag{1.4}$$

This is the mechanism proposed by Chapman in 1930 and although it provides the basis for ozone chemistry in the stratosphere it overestimates the ozone abundance in the tropics and underestimates the abundance at higher latitudes compared to observations.

The most important chemical loss mechanisms for ozone in the stratosphere are catalytic cycles:

$$\mathrm{X + O_3} \rightarrow \mathrm{XO + O_2} \tag{1.5}$$

$$\mathrm{O + XO} \rightarrow \mathrm{O_2 + X} \tag{1.6}$$

where, X can represent nitrogen, hydrogen, chlorine or bromine species. The effectiveness of a catalytic cycle in destroying ozone is limited by the chain length of the cycle (i.e. the number of termination steps in the catalytic cycle before the catalyst at the chain centre is destroyed) and the abundance of the catalyst at the chain centre. The species involved in ozone destruction all have natural as well as anthropogenic sources in the Earth system. Catalytic cycles are further complicated as cycles for different species can interact, and in the lower stratosphere, the most important catalytic loss cycles for ozone are those involving interactions between $\mathrm{BrO/ClO}$, $\mathrm{HO_2/BrO}$ and $\mathrm{ClO/ClO}$ (Lary, 1997). The net result of a catalytic cycle is the conversion of an ozone molecule into two oxygen molecules ($\mathrm{O_3 + O \rightarrow 2O_2}$). There are also null cycles, which do not result in the net loss of odd oxygen, in which reaction (1.6) is replaced by,

$$\mathrm{XO} + h\nu \rightarrow \mathrm{X} + \mathrm{O} \tag{1.7}$$

This is the case in the lower stratosphere where photolysis is the most efficient reaction.

After sunset, reaction (1.7) cannot take place and reactive radicals are converted into relatively unreactive reservoir species. Reservoir species are eventually converted back to the reactive radical through either photolysis or other reactions. The effect of reservoir species is to reduce ozone loss through the temporary removal of reactive radicals from the atmosphere. The main reservoir species of nitrogen and chlorine in the stratosphere are nitric acid ($\mathrm{HNO_3}$) and hydrochloric acid (HCl) respectively, both of which have long lifetimes. Other important reservoir species are chlorine nitrate ($\mathrm{ClONO_2}$) and dinitrogen pentoxide ($\mathrm{N_2O_5}$) which, along with $\mathrm{HNO_3}$ and HCl, play an important role in large-scale ozone loss over the polar regions.

Since the discovery of the Antarctic ozone hole (Farman et al., 1985), large-scale ozone depletion of ozone over the polar regions has been largely attributed to increases in the abundance of halogens due to the anthropogenic activities (for example, CFC production). Ozone destruction in the gas phase is triggered by heterogeneous chlorine and bromine activation on the surfaces of reactive aerosols, stratospheric sulphate aerosols (SSAs) and polar stratospheric clouds (PSCs). In the polar atmosphere, very low temperatures in the polar vortex allow the formation of PSCs. The threshold temperature for PSC formation is approximately 195 K and there are three main types, dependent on temperature and atmospheric composition. The three main types of PSC are: type Ia - solid $HNO_3$ (nitric acid trihydrate or NAT); type Ib - liquid $H_2SO_4/HNO_3/H_2O$ (super ternary solution or STS); and type II - solid $H_2O$. In addition to chlorine activation, there are two further key processes which make the role of PSCs so important in polar ozone depletion:

- the temporary removal of nitrogen species, or denoxification, which occurs as all types of PSC take up $HNO_3$.
- the permanent removal of nitrogen species, or irreversible denitrification, which occurs due to the growth of PSC particles to the point where they are removed from the atmosphere by sedimentation.

The removal of nitrogen species in this way is especially important as it means that chlorine cannot be tied up in the reservoir species $ClONO_2$, leading to further ozone depletion.

Stratospheric ozone depletion is believed to have contributed to a cooling of the lower stratosphere in the last two decades. For the late 1990s, the global and annual mean temperatures in the lower stratosphere are approximately 1 K lower than values in the late 1970s (WMO, 2003). Figure 1.6 shows the vertical profile of the trend in stratospheric temperatures at 45°N between 1979 and 1994 with the $2\sigma$ errors. In the lower stratosphere a trend of between 0.5 and 1.0 degree per decade has been observed (WMO, 1999). Decreases in stratospheric temperatures lead to an increase in the occurrence of PSCs, thus potentially increasing further ozone depletion (Rosier and Shine, 2000).

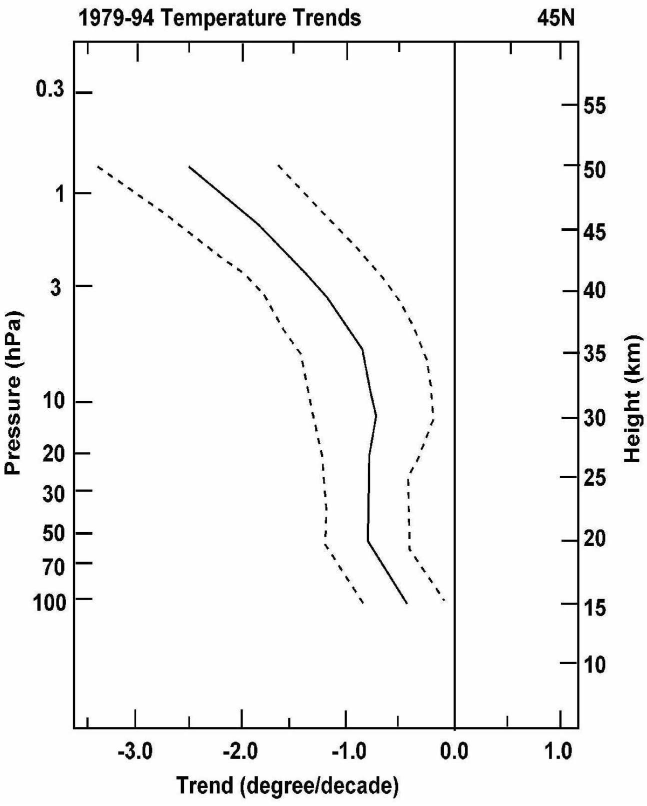

Figure 1.6: Vertical profile of the trend in stratospheric temperature in the period 1979 to 1994, compiled using radiosonde and satellite measurements. The dashed lined show the $2\sigma$ uncertainties (WMO, 1999).

### Tropospheric ozone chemistry

Ozone in the troposphere accounts for approximately 10% of the ozone in the atmosphere, sources of which are transport from the stratosphere and *in-situ* chemical production. The most important mechanism for the chemical production of ozone in the upper troposphere is the photolysis of nitrogen dioxide ($NO_2$) at wavelengths less than 400 nm to produce $NO$ and atomic oxygen (Wayne, 2000):

$$NO_2 + h\nu \rightarrow O + NO \tag{1.8}$$

Ozone is produced through the subsequent reaction of $O$ with $O_2$. $NO_2$ is recycled by reaction of $NO$ with $O_3$. $NO_x$ ($NO + NO_2 + NO_3$) in the troposphere has natural sources (Wayne, 2000): microbial reactions in soil; oxidation of biogenic $\mathrm{NH_3}$, initiated by $\mathrm{OH}$; and lightning. The abundances of $\mathrm{NO}_x$ in the upper troposphere are enhanced, especially over the North Atlantic, by aircraft emissions, potentially leading to greater ozone production (Brasseur et al., 1998; Penner et al., 1999).

Ozone production is enhanced in the presence of peroxy radicals ($\mathrm{RO_2}$), such as hydrogen peroxide ($\mathrm{HO_2}$) and methyl-peroxide ($\mathrm{CH_3O_2}$), as this means that $\mathrm{NO_2}$ can be recycled from $\mathrm{NO}$ without the loss of $\mathrm{O_3}$:

$$\mathrm{RO_2 + NO \rightarrow RO + NO_2} \tag{1.9}$$

where $\mathrm{RO}$ are oxy radicals, for example $\mathrm{OH}$ if the peroxy radical is $\mathrm{HO_2}$. Two of the most important sources of peroxy radicals, and hence ozone production, in the troposphere are the oxidation of carbon monoxide ($\mathrm{CO}$) and methane ($\mathrm{CH_4}$) (Crutzen et al., 1999). Other important reactants influencing ozone production in the upper troposphere are acetone (Jacob et al., 2002) and other volatile organic compounds (VOCs) transported from the lower troposphere, the photolysis of which are a source of $\mathrm{HO}_x$ and peroxyacetylnitrate or PAN ($\mathrm{CH_3COONO_2}$). The role of PAN in ozone production is as a source of $\mathrm{NO_2}$ although this process is relatively slow due to PAN being relatively stable at low temperatures (such as those in the upper troposphere) and $\mathrm{NO_2}$ is released as it is transported from cooler to warmer regions (Wayne, 2000).

Ozone loss in the upper troposphere is through transport to other regions rather than *in situ* chemical reactions. However, ozone production competes with other chemical processes involving (e.g. $\mathrm{NO_2}$ and $\mathrm{HO_2}$) (Seinfeld and Pandis, 1998):

$$\mathrm{OH + NO_2 + M \rightarrow HNO_3 + M} \tag{1.10}$$

$$\mathrm{HO_2 + HO_2 \rightarrow H_2O_2} \tag{1.11}$$

$$\mathrm{RO_2 + HO_2 \rightarrow ROOH + O_2} \tag{1.12}$$

Reaction (1.10) is the predominant reaction, for $\mathrm{NO_2}$, except in low $\mathrm{NO}_x$ conditions.

The chemical role of ozone in the troposphere is important as its photolysis, at wavelengths shorter than 340 nm to produce atomic oxygen in the excited state ($\mathrm{(O(^1D))}$), is a precursor to the formation of $\mathrm{OH}$ radicals, which in turn control the chemistry of the troposphere.

The future abundance of ozone in the troposphere is dependent on the emissions of $\mathrm{CH_4}$, $\mathrm{CO}$, $\mathrm{NO}_x$ and VOCs. The amount of ozone in the troposphere has increased by 30% since pre-industrial times, and modelling studies based on an emission scenario defined by the IPCC, which doubles $\mathrm{CH_4}$ and triples $\mathrm{CO}$ and $\mathrm{NO}_x$ abundances, indicate that levels of ozone will increase by 50% over current levels (IPCC, 2001).

### 1.2.2 Dynamics

The troposphere and stratosphere have fundamentally different characteristics and are separated by the tropopause which is defined, by the World Meteorological Organisation, to be the lowest level at which the temperature lapse rate decreases to 2 K km$^{-1}$ or less, and the lapse rate averaged between this level and any level within the next 2 km does not exceed 2 K km$^{-1}$ (Holton et al., 1995). In the tropics, the tropopause approximately corresponds to an isentropic (constant entropy) surface with a potential temperature of 380 K while in the extra-tropics, it corresponds to a surface with constant potential vorticity of 2 PVU (potential vorticity units). The UTLS region is important as it is a layer in which air from the troposphere and stratosphere air is exchanged across the tropopause and mixed. This exchange of air masses is commonly referred to as Stratosphere-Troposphere Exchange (STE), and has a considerable influence on atmospheric composition and its variability. This mixing takes place as a result of a number of processes occurring at a variety of scales from the global down to the smallest (turbulence). Figure 1.7 shows the schematic representation of STE as described in Holton et al. (1995) and reviewed by Stohl et al. (2003). The mean meridional circulation of the atmosphere is controlled by the Brewer-Dobson circulation which lifts air from the tropical troposphere into the stratosphere where it is transported polewards. It exists due to gravity and Rossby waves breaking and exerting a drag force on the westerly winter-time stratospheric jet. Through thermal wind balance, the wave forcing induces poleward motion leading to warmer, mid-latitude,

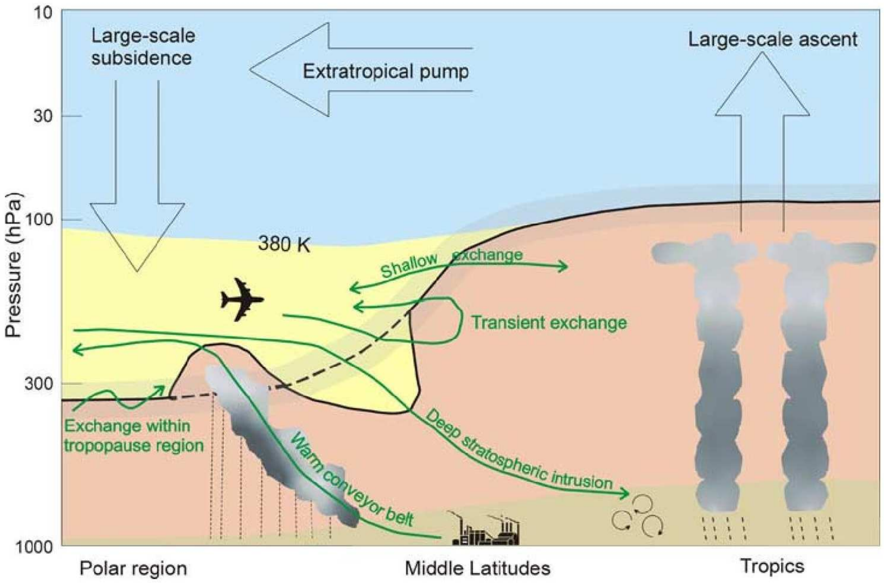

Figure 1.7: Global aspects of STE from Holton et al. (1995) and updated by Stohl et al. (2003). The thick black line shows the average position of the tropopause with the shaded regions showing different atmospheric regions: the blue region is the stratospheric “overworld”, the yellow region is the lowermost stratosphere, the pink region is the free troposphere, and the brown region is the atmospheric boundary layer. The global circulation is shown by the broad arrows, with smaller scale aspects of STE shown by the green trajectories (Stohl et al., 2003).

air intruding into the polar regions and creating a thermodynamically imbalanced situation which in turn leads to a radiative cooling of the polar stratosphere. As the air cools it starts to sink (as its density increases) leading to a downward mass flux toward the mid and high-latitude troposphere, with the mass balance maintained by upward motion across the tropical tropopause.

In the tropics, exchange is mainly from the troposphere to the stratosphere where updraughts in tropical convection rapidly lift humid and ozone-poor air up to the upper troposphere. In the extra-tropics, there is mainly downward transport of ozone-rich stratospheric air into the troposphere due to a variety of meso- and small-scale processes. At mid-latitudes, the tropopause is intersected by isentropic surfaces allowing exchange between the lowermost stratosphere and troposphere to occur through shallow and transient exchange processes. An important process is folding of the tropopause along local wind maxima of the polar, mid-latitude and subtropical jets streams. This results in the tropopause being folded downward and equator-ward with ozone-rich stratospheric air becoming irreversibly transported to the troposphere by deep stratospheric intrusions. Air from the boundary layer (which could potentially be polluted and rich in, for example, $\mathrm{NO_2}$ or PAN) can be transported to the lowermost stratosphere via the warm conveyor belt. Another important process at mid-latitudes is the exchange of ozone via deep convection in the cores of cut-off lows where the vertical stability is small. Other mechanisms for STE in the extra-tropics include mixing by turbulence and waves, and by radiative heating and cooling associated with inhomogeneous distributions of clouds, aerosols and greenhouse gases. At polar latitudes, there may be some smaller-scale interchange within the tropopause region.

### 1.2.3 Radiative effects

Ozone is one of the most radiatively active trace gases in the atmosphere, and the climate system is sensitive to perturbations in the distribution of the ozone abundance. The impact of changes in ozone (and other trace gases) on the climate system is quantified by its radiative forcing, which is defined as the change in net downward radiative flux at the tropopause resulting from any process that acts as an external agent to the climate system (IPCC, 2001).

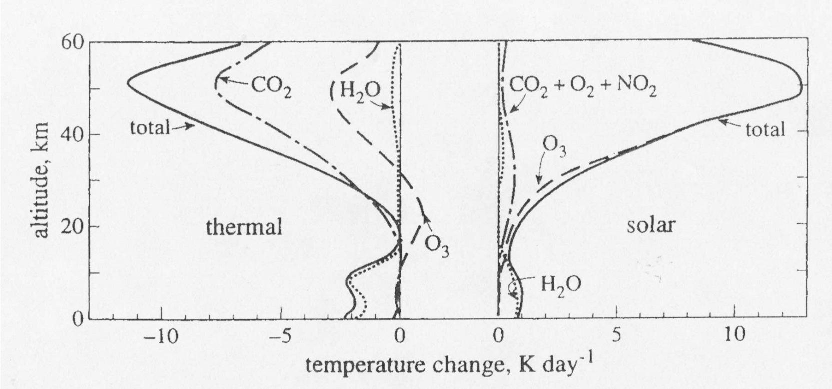

Figure 1.8: Contributions to the total radiative heating rates (K day$^{-1}$) of the principal radiatively active gases in the atmosphere as a function of altitude. The heating rates are separated into thermal cooling and solar heating. The solid line shows the total temperature change compared to $CO_2$ (dot-dash line), $H_2O$ (dotted line) and $O_3$ (dashed line) (Harries, 1997).

Figure 1.8 shows the contribution of ozone, relative to water vapour and carbon dioxide, to the total thermal cooling and solar heating of the atmosphere per day as a function of altitude (Harries, 1997). As shown in Figure 1.6, stratospheric ozone depletion has led to a cooling of the lower stratosphere of between 0.5 and 1.0 degrees per decade at Northern mid-latitudes in the time period 1979 to 1994. This is also reflected in the radiative forcing due to stratospheric ozone of $-0.15 \pm 0.10$ Wm$^{-2}$ between 1979 and 1997 (IPCC, 2001). In the troposphere, increases in the ozone abundance since pre-industrial times have provided a global

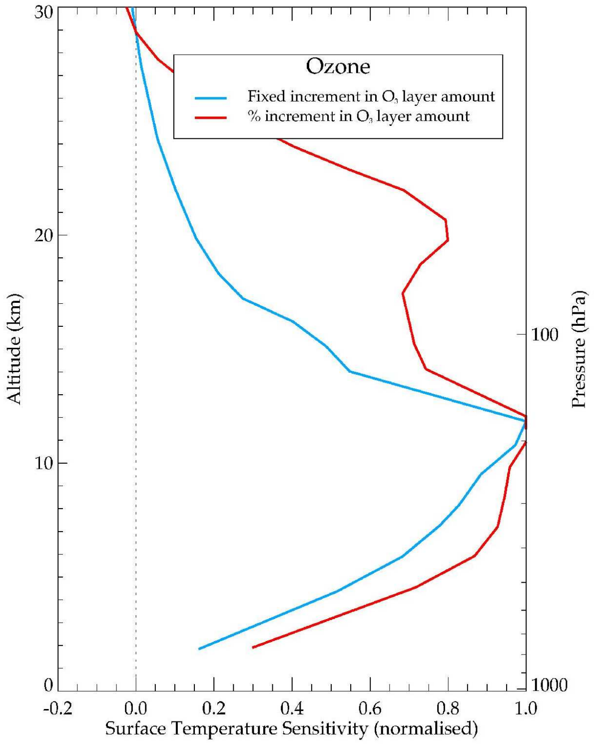

Figure 1.9: Surface temperature response to perturbations in the ozone abundance as a function of height. The blue curve shows the surface temperature response to adding a 10 DU increment to each 1 km layer, and the red line shows the surface temperature response to a 10% increase in the amount of ozone in each 1 km layer. In each case the surface temperature response has been normalised. The results are from a radiative-convective model for the global mean atmospheric profile with no atmospheric feedbacks included. This figure is adapted from Forster and Shine (1997).

average radiative forcing estimated to be[1] +0.35 ± 0.15 $\mathrm{Wm}^{-2}$.

The climate response (in terms of surface temperature change) is sensitive to the altitude at which perturbations to the ozone abundance occurs (Forster and Shine, 1997). The red curve in Figure 1.9 shows the surface temperature response to be most sensitive to a 10 DU perturbation in the ozone concentration in the tropopause region, equivalent to a 400% increase in ozone (Forster and Shine, 1997). The blue curve in Figure 1.9 shows the surface temperature response to be sensitive to a 10% change in the ozone concentration at in the tropopause region

---

[1] Compared to a radiative forcing of 2.43 $\mathrm{Wm}^{-2}$ over the same time period due to the well mixed greenhouse gases.

but also at the ozone maximum in the lower stratosphere at approximately 20 km.

Predicted changes to ozone concentrations over the next 100 years have been shown by Gauss et al. (2003) to increase the radiative forcing by between[2] 0.40 and 0.78 $Wm^{-2}$, compared to 5.6 $Wm^{-2}$ due to all well mixed greenhouse gases. When changes in stratospheric ozone are also included, the radiative forcing increases to 0.82 $Wm^{-2}$.

## 1.3 Summary

The upper troposphere and lower stratosphere is a complex region of the Earth's atmosphere where a number of chemical, dynamical and radiative processes occur. Ozone is one of the most important trace species in the UTLS with its distribution of importance to understanding two of the key issues affecting the Earth system: stratospheric ozone layer recovery and global climate change.

Ozone levels in the lower stratosphere have decreased globally over the last two decades, with the most extreme losses observed at polar latitudes during springtime. Model studies predict that recovery of the Antarctic ozone layer will begin within the next decade, and in the Arctic within the next two decades, with recovery to pre-1980 levels anticipated by 2050 (WMO, 2003). This is due to the reduction in the abundance of chlorine and bromine in the lower stratosphere leading to a reversal of halogen-induced ozone depletion. At NH and SH mid-latitudes, the recovery of ozone column values to pre-1980 values are expected between 2025 and 2050. Uncertainties in the recovery of ozone at mid-latitudes arise as effects of stratospheric cooling on gas phase chemistry may accelerate ozone recovery although mixing of polar air, where lower temperatures could lead to enhanced

---

[2] Related to increases in tropospheric ozone of between 11.4 and 20.5 DU.

ozone depletion, may slightly offset this. These predictions are further limited due to possible future changes to stratospheric aerosol loading due to volcanic activity and future changes in stratospheric circulation and transport (WMO, 2003).

Emissions of ozone and its precursors in the troposphere are not very well quantified due to their localised nature (e.g. photochemical smog, urban pollution, biomass burning). Although tropospheric ozone abundances have increased in the last two decades, and are expected to increase further in the future, ground-based observations are sparse and largely restricted to the Northern hemisphere. Current understanding in our knowledge of the global distribution of ozone in the upper troposphere and lower stratosphere is a limiting factor on estimates of radiative forcing by ozone.

The distribution of the ozone abundance in the UTLS is sensitive to a number of complex and interacting physical and chemical processes. Our understanding of ozone in the UTLS is dependent on our ability to make measurements in this region of the atmosphere. The next chapter outlines the techniques that can be applied to measure the UTLS, with particular emphasis on satellite observations, as these provide measurements over the temporal and spatial time scales required for monitoring the ozone distribution.

# Chapter 2

# Observations of Ozone

As has been highlighted in chapter 1, the UTLS region of the atmosphere is very complex with many different, and interacting, processes affecting the chemical, dynamical and radiative balance. The role of ozone in maintaining these processes is highly important and it is therefore important that the distribution of the ozone abundance in the UTLS is well understood in order to fully quantify these processes.

Due to its relative inaccessibility, observations of the UTLS to date are sparse, although there have been a number of extensive measurement campaigns utilising several different observing techniques. Measurements of the composition of the atmosphere can be undertaken *in situ* or remotely, with passive or active techniques, in several different ways, each with their own particular attributes. Measurements from the ground (e.g. lidar, Dobson spectrophotometers), balloons (e.g. ozonesondes) and aircraft are of great importance but can only provide limited spatial and temporal coverage. Observation from satellites, although requiring high initial investment and long preparation times (of the order a decade), are well suited to providing almost continuous measurements with global coverage.

Satellite observations utilise one of two different viewing geometries: (i) limb viewing, and (ii) nadir viewing. Limb viewing observes layers of the atmosphere above the horizon and provides good vertical resolution. Nadir viewing looks through the atmosphere directly at the surface and provides good horizontal resolution. As the UTLS is a region with strong vertical gradients (especially in the ozone concentration), the limb viewing geometry is preferred as it can provide the relatively high vertical resolution required.

## 2.1 Satellite Limb Sounding

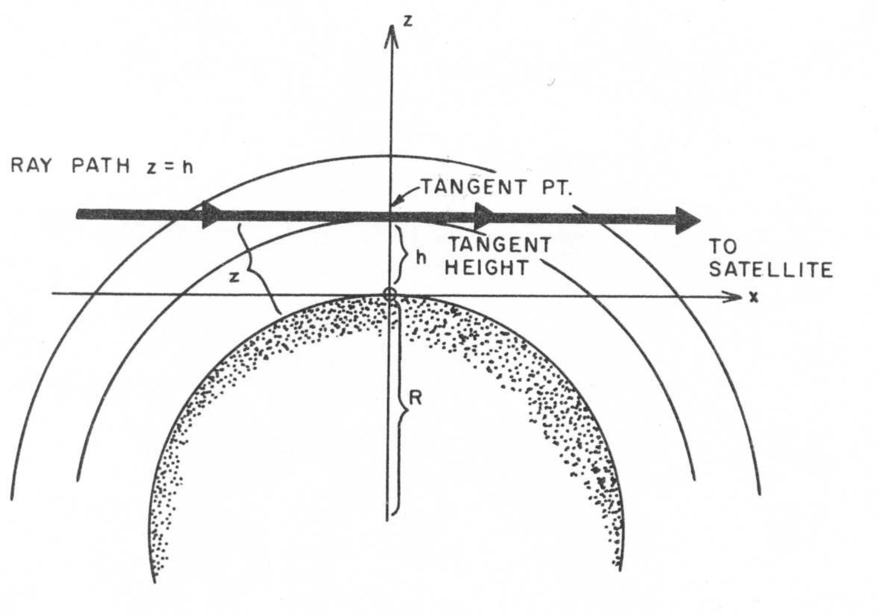

Figure 2.1: Satellite limb viewing geometry (NASA, 1978)

Two of the ways in which limb viewing geometries can be used to make atmospheric measurements are:

- Solar occultation, which views the Sun (although a bright star can also be used, i.e. stellar occultation) through the atmospheric limb, measuring absorption at infrared and visible wavelengths. This technique is limited as only two profiles (sunrise and sunset) can be measured per satellite orbit leading to restricted spatial coverage.

- Limb emission, which views cold space through the atmospheric limb, measuring long wave thermal emission at infrared and microwave wavelengths. This technique provides much better spatial coverage than solar occultation as measurements can be made at many latitudes per orbit under both daytime and nighttime conditions.

The altitude of the atmosphere nominally viewed by a limb sounder is referred to as the tangent height, and is the point at which the line of sight of the instrument passes closest to the surface. In infrared sounding, all of the signal detected by an instrument originates from above the tangent height and is an accumulation of the radiation emitted along a long horizontal path between the tangent height and the instrument (Gille and House, 1971). Most of this signal originates close to the tangent height as atmospheric density decreases exponentially above it. This leads to the weighting functions peaking very sharply at the tangent height, providing good vertical resolution. Vertical profiles are obtained by scanning the instrument field-of-view (FOV) through the atmosphere.

A long horizontal path provides a large amount of emitting material, which can be greater than 60 times that along a vertical path (Gille and House, 1971), increasing the sensitivity to trace gases with low mixing ratios. This does, however, provide poor horizontal resolution of the measurements, although this may not be a significant limitation in the stratosphere (Kidder and Vonder Haar, 1995). Another limitation is the presence of clouds and the finite FOV of an instrument. Clouds in the line of sight of the instrument act as grey bodies of significant opacity at visible and infrared wavelengths and significantly alter the emerging radiation, thus limiting the lowest level in the atmosphere which may be viewed (Gille and

House, 1971). Limb sounding measurements are therefore useful in the upper troposphere and above.

The coverage achievable by a satellite limb sounding instrument is influenced by the orbit of the satellite and the direction in which the instrument points. To obtain maximum coverage Low Earth Orbits (LEO) with typical altitudes of between 600 and 1000 km (corresponding to orbital periods of between 100 and 105 minutes) are used. The altitude of a LEO is affected by the size of the telescope, orbital decay, swath width at the equator, orbit repeat time and the launch vehicle. The inclination of the orbit is also an important factor as orbits will precess due to the Earth being non-spherical. The direction in which the instrument points can be either along track (i.e. in the same direction the velocity vector of the satellite) or cross track (i.e. to the side, perpendicular to the velocity vector). When pointing either across or along track (forwards or rearwards), Doppler shifts of the measurements, due to the satellite velocity and winds, need to be taken into account.

## 2.2 Radiative Transfer Theory

### 2.2.1 Introduction

Remote sounding observations are possible due to the transfer of radiation through the atmosphere and to the instrument:

$$\frac{dI(\nu)}{ds} = -\mu(\nu)I(\nu) + \rho j(\nu) \tag{2.1}$$

where $I(\nu)$ is the radiation intensity at frequency $\nu$, $s$ is the coordinate along the radiation path, $\mu(\nu)$ is the extinction coefficient, $\rho$ is the mass density and $j(\nu)$

is the emission coefficient per unit mass. In the mid-infrared it is reasonable to assume a pure gas atmosphere with negligible scattering, allowing the extinction coefficient to be equal to the gas absorption coefficient $\alpha(\nu)$. In the absence of scattering and assuming local thermodynamic equilibrium (LTE)[1], the emission source function can be written:

$$\rho j(\nu) = \alpha(\nu) B(\nu, T) \tag{2.2}$$

where $B(\nu, T)$ is the Planck function at frequency $\nu$ and temperature $T$. Equation (2.1) can be rewritten:

$$\frac{dI(\nu)}{ds} = -\alpha(\nu) I(\nu) + \alpha(\nu) B(\nu, T) \tag{2.3}$$

This equation is integrated to provide the integral equation of radiative transfer. The basic purpose, for a given observing geometry and atmospheric model, of a radiative transfer model is the solution of the radiative transfer equation, which, for the monochromatic radiance emerging from a path through the atmopshere, can be written:

$$I(\nu, s_{\mathrm{obs}}) = I(\nu, s_0)\tau(\nu, s_0, s_{\mathrm{obs}}) + \int_{s_0}^{s_{\mathrm{obs}}} B(\nu, T(s))\alpha(\nu, s)\rho_{\mathrm{a}}(s)\tau(\nu, s, s_{\mathrm{obs}})\, ds \tag{2.4}$$

where, $s$ is a distance along the path ($s_0$ and $s_{\mathrm{obs}}$ are the distances of the start of the path and the observer respectively), $I(\nu, s)$ is the radiation intensity at wavenumber $\nu$, $B(\nu, T(s))$ is the Planck function at temperature $T(s)$, $\alpha(\nu, s)$ is the monochromatic absorption coefficient, $\rho_{\mathrm{a}}(s)$ is the absorber number density,

---

[1] This is reasonable in the UTLS, where the relative populations of the lower and upper molecular energy levels are determined by the Boltzmann distribution. At higher altitudes, non-LTE conditions (i.e. $\rho j(\nu) \neq \alpha(\nu)B(\nu, T)$) can exist, where the excitation temperature of each molecule is different from the thermal atmosphere (Dudhia, 1996).

and $\tau(\nu, s_1, s_2)$ is the transmittance between $s_1$ and $s_2$:

$$\tau(\nu, s_1, s_2) = e^{-\int_{s_1}^{s_2} \alpha(\nu,s)\rho_{\mathrm{a}}(s)\,ds} \tag{2.5}$$

The absorption coefficient $\alpha(\nu, s)$ is a sum over all absorbers:

$$\alpha_l(\nu, s) = \sum_{i=1}^{N_{\mathrm{abs}}} \sigma_i(\nu, l) X_i(l) \tag{2.6}$$

where, $X_i(l)$ is the volume mixing ratio, and $\sigma_i(\nu, l)$ is the absorption cross-section of absorber $i$:

$$\sigma_i(\nu, l) = \sum_{j=1}^{N_{\mathrm{lin}}} S_{i,j}(T_l) A_{i,j}(\nu - \nu_{i,j}, T_l, p_l) \tag{2.7}$$

where, for $N_{\mathrm{lin}}$ spectral lines, $S_{i,j}(T_l)$ and $A_{i,j}(\nu - \nu_{i,j}, T_l, p_l)$ are the line strength and the line shape of spectral line $j$ of absorber $i$ respectively. The strength of a spectral line is dependent on the population of the energy levels of the absorbing molecule and is calculated:

$$S = \int_0^\infty \sigma(\nu) d\nu = \left(\frac{N_1 B_{12} h \sigma(0)}{c}\right)\left(1 - \frac{g_1 N_1}{g_2 N_2}\right) \tag{2.8}$$

where, $N_1$ and $N_2$ are the number densities of atoms in the lower and upper levels of the transition in question and $g_1$ and $g_2$ are the degeneracies of those levels, $\sigma(0)$ is the frequency of the transition, $B_{12}$ is the Einstein coefficient describing the probability per unit time of absorption resulting in a transition from level one to level two, $h$ is the Planck constant and $c$ is the speed of light.

Spectral lineshapes of absorbers in the UTLS, where the lineshape is subject to broadening by temperature and pressure, are generally defined by the Voigt line-shape:

$$A_{i,j}(\nu - \nu_{i,j}, T_l, p_l) = \frac{K(x,y)}{\gamma_{\mathrm{D}}}\sqrt{\frac{\ln 2}{\pi}} \tag{2.9}$$

where, $\gamma_{\mathrm{D}}$ is the Doppler half width and $K(x,y)$ is the Voigt function:

$$K(x,y) \equiv \frac{y}{\pi}\int_{-\infty}^{+\infty}\frac{e^{-t^2}}{y^2 + (x-t)^2}dt \tag{2.10}$$

$x$ and $y$ are the ratio of the Lorentz to Doppler half widths and the frequency scale in units of Doppler half width respectively:

$$x \equiv \frac{\nu - \nu_{i,j}}{\gamma_{\mathrm{D}}}\sqrt{\ln 2}, y \equiv \frac{\gamma_{\mathrm{L}}}{\gamma_{\mathrm{D}}}\sqrt{\ln 2} \tag{2.11}$$

### 2.2.2 Radiative transfer in emission

For measurements of limb thermal emission, $I(\nu, s_0)$ is the emission of cold space and, in the infrared, can be considered as negligible. Equation (2.4) may be written:

$$I(\nu, s_{\mathrm{obs}}) = \int_{s_{\mathrm{b}}}^{s_{\mathrm{obs}}} B(\nu, T(s))\alpha(\nu, s)\rho_{\mathrm{a}}(s)\tau(\nu, s, s_{\mathrm{obs}})\, ds \tag{2.12}$$

where, $s_{\mathrm{b}}$ is the effective edge of the Earth's atmopshere on the far side of the tangent point.

### 2.2.3 Rotational-vibrational spectroscopy of ozone

The interaction of electromagnetic radiation with matter produces an energy spectrum which is characteristic to a particular molecule. For the interaction to occur, the molecule must have, or be able to acquire, a dipole or quadropole moment. The amount of energy of the radiative emission (i.e. the position of the spectral lines) depends on energy transitions - electronic, vibrational and rotational - of individual molecules. Rotational energy transitions occur in the far infrared and microwave regions of the spectrum (from approximately 1 to 500 cm$^{-1}$) with vibrational transitions in the near to far infrared (500 to 10$^4$ cm$^{-1}$), and electronic transitions in the ultra-violet and visible (10$^4$ to 10$^5$ cm$^{-1}$). The energy of vibrational transitions is much greater than that of rotational transitions, and this leads to the formation of rotation-vibration bands of lines due to simultaneous rotational and vibrational transitions.

The geometrical structure of molecules, and the moments of inertia along the three principal axes ($I_A$, $I_B$ and $I_C$), determines the position of rotational spectral lines. There are four main types of rotating molecules (Stephens, 1994):

- Linear molecules (e.g. $CO_2$, $N_2O$, all diatomic molecules): $I_A$ = 0, $I_B$ = $I_C \neq 0$
- Symmetric top molecules (e.g. $NH_3$): $I_A \neq 0$, $I_B$ = $I_C \neq 0$
- Spherical symmetric top molecules ($CH_4$): $I_A$ = $I_B$ = $I_C$
- Asymmetric top molecules (e.g. $H_2O$, $O_3$): $I_A \neq I_B \neq I_C$

Rotational transitions are classified by the angular momentum quantum number ($J$), with allowed transitions given by the selection rule: $\Delta J = 0, \pm 1$. For tri-atomic molecules[2], there are three fundamental modes of vibration which are represented by quantum numbers $\nu_i$ ($i = 1, 2, 3$): symmetric stretching ($\nu_1$), bending ($\nu_2$), and asymmetric stretching ($\nu_3$). The rotation-vibration bands are divided into three branches depending on the selection rules for the rotation and vibration quantum numbers. These are classified as the P-branch ($\Delta J = -1$), the Q-branch ($\Delta J = 0$) and the R-branch ($\Delta J = +1$).

---

[2] For a non-linear molecule containing $N$ atoms, there are $(3N - 6)$ degrees of freedom for vibrational modes.

The ozone molecule, in its electronic ground state, is an asymmetric top molecule with three normal vibrations $\nu_1$ (symmetric stretching), $\nu_2$ (bending) and $\nu_3$ (asymmetric stretching), see Figure 2.2, approximately located at 1103, 701 and 1042 cm$^{-1}$ respectively[3]. The energy levels of the ozone molecule can be described by a set of three rotational quantum numbers ($J$, $K_a$ and $K_c$)[4] with the conditions $K_a \leq J$, $K_c \leq J$ and $K_a + K_c = J$ or $J + 1$, and three vibrational quantum numbers ($\nu_1$, $\nu_2$ and $\nu_3$). The spectroscopy of the ozone molecule at infrared and microwave wavelengths is well characterised and these measurements are reviewed in Ivanov and Panchenko (1994) and Flaud and Bacis (1998). In recent years the ozone molecule has been the subject of extensive laboratory studies, especially in the 10 $\mu$m spectral region (the $\nu_3$ transition), to determine the

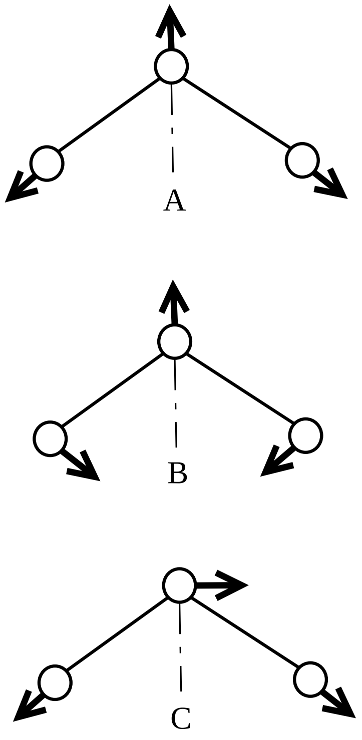

Figure 2.2: Normal modes of vibration for an asymmetric top molecule. Diagrams A, B and C represent the $\nu_1$, $\nu_2$ and $\nu_3$ transitions respectively.

---

[3] The location of these modes are for the $^{16}O^{16}O^{16}O$ confirguration of the ozone molecule, which accounts for approximately 99% of the ozone in the atmosphere.

[4] $J$ for the total angular momentum, and $K_a$ and $K_c$ for the projection of the total angular momentum onto the axes of the minimum and maximum moments of inertia, respectively.

absolute line position and intensities in this region. For the processing of ozone data from MIPAS observations, further improvements have been made to ozone, and other trace species, emission lines in the HITRAN96 spectroscopic database through comparisons with spectral data from the ATMOS instrument (Flaud et al., 2003).

## 2.3 Ozone Remote Sounding Instruments

### 2.3.1 Previous measurements

There have been a large number of satellite-based instruments designed to measure atmospheric ozone in the last 40 years. A summary of the instruments that have been used to measure ozone in the atmosphere is given in Table 2.1. Previous reviews of historical satellite instruments for sounding atmospheric ozone are given by Krueger et al. (1980) and Miller (1989).

The Nimbus series of satellites in the 1970s carried a number of instruments that utilized both backscattered ultraviolet and infrared emission. Nimbus 7 was the first satellite to obtain global profiles of ozone. Instruments which utilized backscattered ultraviolet were the Solar Backscattered Ultraviolet (SBUV) radiometer experiment and the Total Ozone Mapping Spectrometer (TOMS). In the infrared, the earlier Nimbus satellites (3 and 4) observed in the nadir, and hence measured total column ozone, with an InfraRed Interferometer Spectrometer (IRIS). The first satellite measurements of limb infrared emission were made by the Limb Radiance Inversion Radiometer (LRIR) on Nimbus 6 with profiles measured between approximately 15 and 60 km at 3 km vertical resolution. An improved version of LRIR, the Limb Infrared Monitor of the Stratosphere (LIMS), on Nimbus 7 measured ozone profiles from 10 to 65 km at a vertical resolution of

| Technique | Instrument | Vertical range (resolution), km |
|---|---|---|
| emission | IRIS[1] | Column |
| | LRIR[2] | 16-60 (3) |
| | LIMS[3] | 10-65 (2.8) |
| | TOVS[4] | Column |
| | CLAES[5] | 10-60 (2.5) |
| | ISAMS[5] | 15-40 (2.36) |
| | MLS[5] | 15-80 (3) |
| | IMG[9] | Column |
| occultation | HALOE[5] | 15-100 (2) |
| | SAGE I[7] | 10-55 (3) |
| | SAGE II[8] | 10-65 (3) |
| | POAM II[10] | 8-50 (1) |
| | ILAS[9] | 8-70 (2-3.5) |
| backscatter uv | BUV[1] | Column |
| | SBUV[3] | 25-55 (8) |
| | TOMS[3] | Column |
| | SBUV2[4] | 25-55 (8) |
| | GOME[6] | 0-80 (4-6) |

Table 2.1: Satellite instruments that have provided long term observations of atmospheric ozone. Satellite platforms: 1 = Nimbus 4; 2 = Nimbus 6; 3 = Nimbus 7; 4 = NOAA operational satellites; 5 = UARS; 6 = ERS-2; 7 = AEM-2; 8 = ERBS; 9 = ADEOS; 10 = SPOT 3.

2.8 km (Remsberg et al., 1984).

The US National Oceanic and Atmospheric Administration (NOAA) has been launching operational satellites since the late 1970s, providing measurements of total column ozone and ozone profiles. Modified versions of the SBUV experiment (SBUV/2) have been providing measurements, as described above, since 1985 and 1989 to the present. Measurements of total ozone by infrared emission have been made using the Tiros Operational Vertical Sounders (TOVS) since 1978. TOVS is composed of three separate instruments of which infrared measurements are made by the High resolution Infrared Radiation Sounder (HIRS).

Measurements using solar occultation have been made by the Stratospheric Aerosol and Gas Experiments (SAGE I, 1979 to 1981, and SAGE II, 1984 to 2001). SAGE II is a Sun photometer which measures solar extinction through the atmospheric limb in seven wavelength channels between 0.385 and 1.02 $\mu$m. Ozone was measured at 0.385, 0.453, 0.525, 0.6 and 1.02 $\mu$m. Ozone profiles from SAGE II are measured from 10 to 65 km, with a vertical resolution of 1 km (Cunnold et al., 1989).

In 1991, NASA launched the Upper Atmosphere Research Satellite (UARS) which was a mission aimed specifically at improving knowledge of the atmosphere. There were two limb sounders that made measurements of infrared emission. The Improved Stratospheric And Mesospheric Sounder (ISAMS) experiment, which is described in more detail in chapter 3, measured ozone from about 15 to 40 km with a vertical resolution of 2.36 km. The Cryogenic Limb Array Etalon Spectrometer (CLAES) measured ozone from about 15 to 60 km with a vertical resolution of 2.5 km. The CLAES measurements were made by Fabry-Perot etalon interferometers in nine discrete spectral bands between 2843 and 780 cm$^{-1}$ (3.5 to 12.9 $\mu$m) (Bailey et al., 1996). Measurements of ozone were also made by the Microwave Limb Sounder (MLS) which measured thermal emission at microwave wavelengths from about 15 to 50 km with a vertical resolution between 3 and 5 km (Froidevaux et al., 1996). An instrument designed to measure in solar occultation was also on UARS: the HALogen Occultation Experiment (HALOE) uses gas filter and broadband radiometry to measure absorption by the atmospheric limb at infrared wavelengths (ozone was measured by a radiometer at 9.6 $\mu$m), and ozone profiles are retrieved from about 15 to 100 km with a vertical resolution of about 2 km (Bruhl et al., 1996).

The US Naval Research Laboratory has developed the Polar Ozone and Aerosol Measurement (POAM II and III) instruments which have operated on the French Centre Nationales d'Espace Spatiales (CNES) SPOT series of satellites: SPOT 3 (1993 to 1996) and SPOT 4 (1998 to present). These instruments perform solar occultation measurements in nine narrow band optical channels, between 350 and 1030 nm, from 15 to 50 km at 1 km vertical resolution (Rusch et al., 1997).

The Japanese Advanced Earth Observing Satellite (ADEOS) provided measurements of ozone profiles from two instruments operating in the infrared between November 1996 and June 1997. Firstly, the Improved Limb Atmospheric Spectrometer (ILAS) was a solar occultation sensor, consisting of two grating spectrometers covering a spectral range from 6.21 to 11.77 $\mu$m, and ozone profiles were measured from 8 to 70 km with a vertical resolution of 2 to 3.5 km (Sugita et al., 2002). Secondly, the Interferometric Monitor of Greenhouse gases (IMG), the first high spectral resolution spectrometer measuring infrared emission to fly in space, was a nadir viewing Fourier transform spectrometer with a spectral range between 714 and 3030 cm$^{-1}$ at 0.1 cm$^{-1}$ resolution.

The Global Ozone Monitoring Experiment (GOME) on the ESA ERS-2 satellite measures scattered radiation over a large spectral range (240 to 790 nm) using a differential optical absorption spectroscopy (DOAS) measuring system. GOME has been used to retrieve both total ozone and ozone profiles. Ozone profiles have been retrieved from 0 to 80 km at a vertical resolution of between 4 and 6 km (Siddans et al., 1997).

### 2.3.2 Current and future measurements

Table 2.2 lists the satellite instruments currently providing and scheduled to provided ozone data. At present, measurements of ozone from satellite platforms are provided by a number of instruments on different platforms. In February 2001, the Odin satellite was launched by the Swedish space agency with two instruments for atmospheric chemistry applications: the Submillimetre Microwave Radiometer (SMR) and the Odin Spectrometer and InfraRed Imager System (OSIRIS). The SMR makes measurements with five radiometers at 119 GHz and between 486 to 580 GHz (Baron et al., 2001), while the OSIRIS instrument makes measurements with a grating spectrometer covering a spectral range from 200 to 800 nm (von Savigny et al., 2003). The two instruments are co-aligned and observe the atmospheric limb at tangent altitudes between 10 and 80 km with a 3 km vertical spacing (Baron et al., 2001).

In March 2002 the European Space Agency (ESA) launched the polar orbiting ENVISAT-1 platform which has three instruments with the capability to measure ozone. The Michelson Interferometer for Passive Atmospheric Sounding (MIPAS) is a Fourier transform spectrometer measuring high resolution gaseous emissions in the near to mid infrared and is discussed in more detail in chapter 3. The SCanning Imaging Absorption SpectroMeter for Atmospheric CHartographY (SCIAMACHY) is an imaging spectrometer and measures solar radiation transmitted, backscattered and reflected by trace gases in the troposphere and stratosphere employing both nadir and limb geometries. SCIAMACHY is a development of GOME with a larger wavelength range (240-1700 nm, contiguous plus additional bands up to 2.35 $\mu$m, with a resolution of 0.2-0.5 $\mu$m) (Noel et al., 2002). GOMOS (Global Ozone Monitoring by Occultation of Stars) works on the same principle as the SAGE instruments, except by using stars, many more

| Technique | Instrument | Vertical range (resolution), km |
|---|---|---|
| emission | SMR[4] | 10-80 (3) |
| | MIPAS[5] | 6-68 (3) |
| | AIRS[6] | Column |
| | *IASI*[9] | Column |
| | *HIRDLS*[10] | 8-80 (1) |
| | *TES*[10] | 0-33 (2.3) |
| occultation | POAM III[1] | 8-50 (1) |
| | SAGE III[2] | 6-85 (0.5) |
| | GOMOS[5] | 15-100 (1.7) |
| | ILAS-II[7] | 12-60 (1) |
| | ACE-FTS[8] | 10-100 (3-4) |
| | MAESTRO[8] | 10-100 (1) |
| backscatter uv | TOMS[3] | Column |
| | OSIRIS[4] | 10-80 (3) |
| | SCIAMACHY[5] | 0-90 (3) |
| | *GOME-2*[9] | Column |
| | *OMI*[10] | 20-45 (6) |

Table 2.2: Current and future satellite instruments for measuring atmospheric ozone. Satellite platforms: 1 = SPOT 4; 2 = Meteor-3M; 3 = Earthprobe; 4 = Odin; 5 = ENVISAT-1; 6 = EOS Aqua; 7 = ADEOS-II; 8 = SCISAT; 9 = MetOp; 10 = EOS Aura. Instruments in italics are those scheduled for launch in the next few years.

profile measurements can be made (Ratier et al., 1999). Also in 2002, NASA launched the EOS Aqua platform aboard which the nadir viewing Atmospheric InfraRed Sounder (AIRS) makes measurements of thermal emission between 650 and 2674 cm$^{-1}$ (Aumann et al., 2003). The Japanese ADEOS-II platform with another ILAS instrument was launched in 2002.

In August 2003, the Canadian Space Agency launched its SCISAT mission with two occultation instrments: the Atmospheric Chemistry Experiment Fourier Transform Spectrometer (ACE-FTS) and the Measurements of Aerosol Extinction in the Stratosphere and Troposphere Retrieved by Occultation (MAESTRO). The ACE-FTS instrument has a spectral range of 2 to 13 $\mu$m and the MAESTRO is a dual spectrometer covering a spectral range of 0.285 to 1.03 $\mu$m. Both instruments effectively share the same field of view and measure vertical profiles from approximately 10 to 100 km with a vertical resolution of 3 to 4 km for ACE-FTS and 1 km for MAESTRO (Bernath, 2000).

Continuation of the ozone column dataset is provided by the TOMS instrument on the Earthprobe platform, and the SAGE dataset is continued by the SAGE III instrument on the Russian/US Meteor-3M mission launched in 2001, with plans for another SAGE III instrument on the International Space Station in 2005.

Scheduled for launch in the near future are the NASA EOS Aura platform which will have a payload of four instruments that will make complementary measurements of chemistry and dynamics in the lower and middle atmosphere. The High Resolution Dynamics Limb Sounder (HIRDLS) will measure ozone and water vapour at infrared wavelengths, as well as transport. Another MLS will be on Aura to measure ozone and upper tropospheric water vapour. The Ozone Monitoring Experiment (OMI) will measure backscattered solar radiation at UV and visible wavelengths providing global total ozone amounts in one day. The Tropospheric Emission Spectrometer (TES) will use both limb and nadir viewing geometries to measure infrared emission at high wavelength resolution to measure water vapour and tropospheric ozone. More information on these instruments can be found inthe EOS Reference Handbook (NASA, 1999). A second GOME instrument is also scheduled to be launched aboard an operational meteorology platform in the near future.

Two of the distinctive aspects of some of these future measurements (and especially the MIPAS instrument) are the ability to sound into the troposphere with reasonable vertical resolution and the use of high spectral resolution instruments.

## 2.4 Summary

This chapter has provided an overview of the range of observing geometries and techniques available for sounding the atmosphere from satellite platforms. There have been a significant number of satellite instruments dedicated to measuring the distribution of atmospheric ozone since the early 1970s. At present there are several instruments in operation with others scheduled for launch in the very near future. Improvements in technology have led to increased levels of sophistication in the design of such instruments and provide the potential to be able to sound the UTLS region of the atmosphere to a high degree of accuracy.

The radiative transfer equation is critical to being able to perform remote sounding observations of the atmosphere as it calculates the radiance that the satellite instrument should measure. The equation of radiative transfer forms the basis for forward model calculations, and approaches to the integration of the radiative transfer equation for an infrared limb sounder, such as MIPAS, are discussed in further detail in chapter 6.

# Chapter 3

# The ISAMS, MLS and MIPAS Instruments

## 3.1 ISAMS

The Improved Stratospheric And Mesospheric Sounder (ISAMS) experiment on the NASA Upper Atmosphere Research Satellite (UARS) provided approximately 180 days of atmospheric temperature and composition data with almost global coverage between September 26 1991 and July 29 1992. The instrument was an infrared spectroradiometer which means that, although it has absolute radiometric calibration and high spectral resolution, measurements are made in fixed channels which do not scan the spectrum. Figure 3.1 shows the position of the ISAMS experiment on the UARS platform relative to the other instruments.

Measurements of thermal emission from the atmospheric limb were obtained by pressure modulator radiometers (Taylor, 1983), allowing for high selectivity of spectral lines of the target gas in each pressure modulator cell or PMC (ISAMS had cells containing $CO_2$, $CO$, $CH_4$, $NO$, $N_2O$, $NO_2$ and $H_2O$). Emission lines

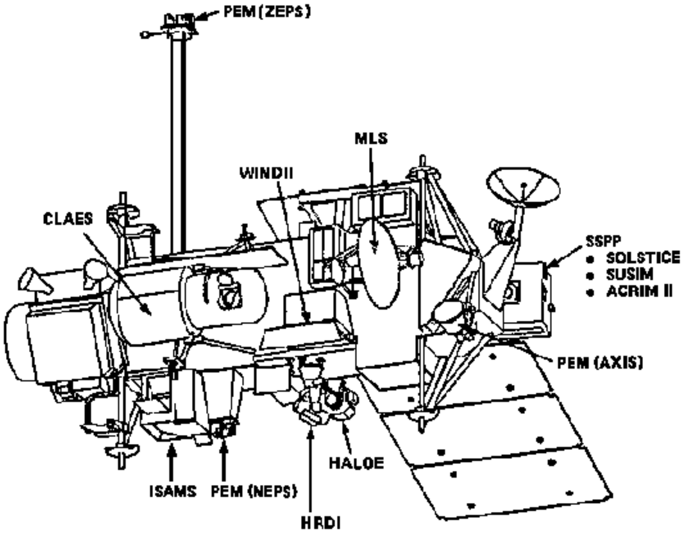

Figure 3.1: Layout of the UARS platform showing the relative positions of each of the instruments.

of other gases are rejected, except where the lines overlap. This occurs because the detected signal originates in or near the line centres of the target gas in the cell. These ‘pressure modulated’ signals were obtained for all species contained in each ISAMS PMC. A ‘wideband’ signal, providing a relatively wide spectral band (defined by the interference filter) radiance measurement, which allowed for extended vertical coverage as the atmosphere is partially transparent to the wideband signal at lower altitudes, was also obtained for each PMC.

Table 3.1 shows the eight ISAMS spectral channels with their associated central wavelength and target gas to be measured. For each channel there was a detector array with four elements arranged vertically with each detector element measuring 2.36 km vertically by 16.6 km horizontally when projected onto the atmospheric limb. The eight channels occupied two fields of view, with four channels in each, arranged vertically and separated by 2.36 km, to provide eight detector images uniformly spaced on the limb. Channels 3 and 7 (i.e. one in each field of view) were further sub-multiplexed by filter wheels each containing four filters to provide the wideband measurements. These provide information on the trace species unable to be contained in pressure modulator cells (i.e. $\mathrm{O_3}$, $\mathrm{HNO_3}$ and $\mathrm{N_2O_5}$). In Table 3.1, the first number shows the channel number and in channels 3 and 7, the second number represents the filter wheel position (i.e. 3.3 denotes channel 3 and filter wheel position 3). These channels were chosen to minimise the contribution of overlapping lines of unwanted gases and at the same time maximise the signal by including many strong lines. The 'window' channel at 12.1 $\mu$m is relatively free of molecular band absorption and was designed to assist with the retrieval of aerosol extinction (Taylor et al., 1993).

| Channel number | Wavelength ($\mu$m) | Gas |
|---|---|---|
| 0 | 4.6 | $\mathrm{CO}$ |
| 1 | 6.8 | $\mathrm{H_2O}$ |
| 2 | 7.9 | $\mathrm{N_2O}$ |
| 3.0 | 15.5 | $\mathrm{CO_2}$ |
| 3.1 | 16.3 | $\mathrm{CO_2}$ |
| 3.2 | 11.3 | $\mathrm{HNO_3}$ |
| 3.3 | 10.3 | $\mathrm{O_3}$ |
| 4 | 5.3 | $\mathrm{NO}$ |
| 5 | 6.3 | $\mathrm{NO_2}$ |
| 6 | 7.4 | $\mathrm{CH_4}$ |
| 7.0 | 15.5 | $\mathrm{CO_2}$ |
| 7.1 | 16.3 | $\mathrm{CO_2}$ |
| 7.2 | 8.1 | $\mathrm{N_2O_5}$ |
| 7.3 | 12.1 | Window |

Table 3.1: Central wavelength of and target gas measured by each of the ISAMS spectral channels (Taylor et al., 1993).

Figure 3.2 shows the scan pattern employed by ISAMS up until January 13 1992 and illustrates the projection of the detector elements in each field of view onto the limb. The repeat time of the scan pattern (Engineering Major Frame or EMAF) was 65.536 s and comprised of 32 ISAMS measurement periods (IMPs)

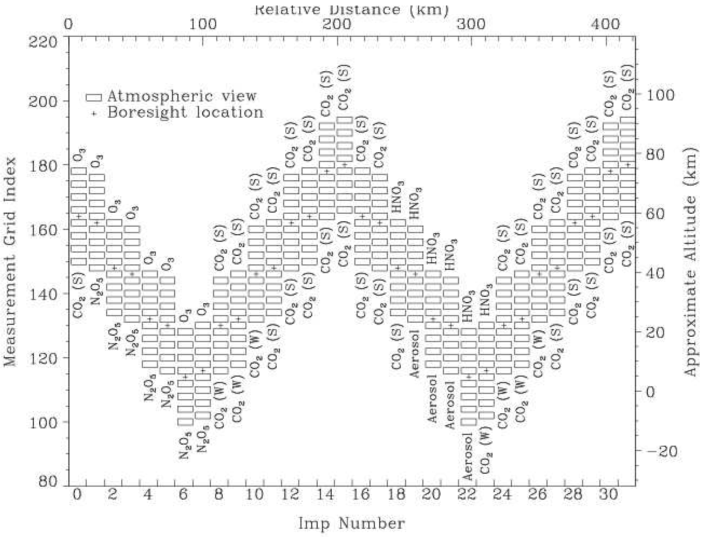

Figure 3.2: ISAMS limb scan pattern for one engineering major frame, used up until January 13 1992. The box indicates the nominal field of view of the channel and the plus indicates the bore sight of the instrument. The four detectors in each detector array are shown above and below the bore-sight location. The constituent selected by each filter wheel are shown above and below the pattern (Rodgers et al., 1996).

of 2.048 s. In every fourth EMAF, one quarter of the time was spent on a radiometric calibration sequence (Rodgers et al., 1996).

The UARS platform was delivered into an orbit inclined at 57° to the Equator which precesses approximately 5° per day relative to the Sun. For one day of data, local solar time around each orbit is more or less a constant function of latitude, although over a period of 72 days, the orbit precesses through a complete diurnal cycle. The ‘near global’ latitude coverage of the ISAMS measurements are from 80° S to 80° N, although the coverage of a single orbit is from 34° on one side of the Equator to 80° on the other side. This is due to measurements only being possible on the side of UARS pointing away from the Sun in order to maintain thermal stability and protect the infrared detectors[1]. A yaw manoeuvre of the UARS spacecraft, approximately every 36 days, allowed for the complete

---

[1] ISAMS also has the ability, when the Sun-satellite geometry places the instrument in the Earth’s shadow, to view the orbits on the reverse side of the spacecraft, allowing the potential coverage to be from 80° N to 80° S for either satellite flight direction (Rodgers et al., 1996).

‘global’ coverage. A full technical description of the ISAMS experiment and the measurements are given by Taylor et al. (1993).

## 3.2 MLS

The Microwave Limb Sounder (MLS) instrument, also on the NASA UARS platform, was operational between September 1991 and December 1999 (Livesey et al., 2003), providing approximately eight years of geophysical data with almost global coverage. The instrument comprised of three radiometers measuring thermal emission at microwave wavelengths near 63, 183 and 205 GHz. The radiometers combine the signal from the atmospheric limb with a local oscillator signal in non-linear mixers employing Schottky diodes, yielding an intermediate frequency (IF) signal. The IF signals are divided into six bands, chosen to observe emission lines for molecular oxygen (63 GHz), water vapour (183 GHz), ozone (183 and 205 GHz) and chlorine monoxide (205 GHz). The radiances in each band are measured by six nominally identical spectrometer filter banks, each consisting of 15 channels, covering up to ±255 MHz away from the line centre. The channels vary in width from 2 MHz near the line centre to 128 MHz in the wings.

In normal operation, the MLS performs a scan of the Earth’s limb, at tangent altitudes between 1 and 90 km, every 65.536 s, or one MLS Major Frame (MMAF). Each MMAF consists of 32 MLS Minor Frames (MMIFs). Most of the 2.048 s duration of each MMIF is dedicated to limb observations with the remainder used to step between each tangent view. In each scan, six MMIFs are used to view space or a calibration target and/or antenna retrace activities.

The MLS instrument viewed the limb from the same side of the UARS spacecraft as the ISAMS and as such the latitude coverage of the MLS measurements are the same as for ISAMS: 34° on one side of the equator to 80° on the other side with UARS undergoing a yaw manoeuvre of 180° approximately every 36 days. This is important for the comparison of ozone profiles retrieved from ISAMS and MLS in chapter 5. A full description of the MLS instrument is given by Barath et al. (1993).

## 3.3 MIPAS

The Michelson Interferometer for Passive Atmospheric Sounding (MIPAS) experiment was launched aboard the ESA ENVISAT-1 platform on March 1 2002 and is a high spectral resolution Fourier Transform Spectrometer (FTS) designed to measure concentration profiles of several atmospheric constituents on a global scale. Figure 3.3 shows the schematic layout of the ENVISAT-1 platform and the relative positions of each of the instruments.

An FTS is a Michelson interferometer with a movable mirror, and interference patterns are produced by moving the mirror over some distance. The produced interference pattern is then the Fourier transform of the spectrum of the measured signal. One of the main advantages of an FTS over grating spectrometers is the multiplex advantage, whereby a spectrum can be measured with an advantage of $t^{1/2}$ in the time $t$ required to obtain a given signal-to-noise ratio, providing the noise is detector-limited. A Michelson interferometer consists of two mirrors (one fixed and one movable) oriented at right-angles to each other with a beam-splitter placed at the vertex of the right-angle and oriented at 45° relative to the two mirrors.

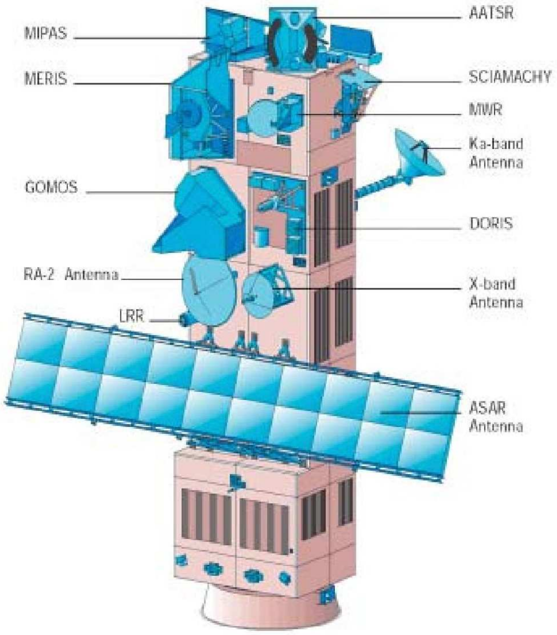

Figure 3.3: Layout of the ENVISAT-1 platform showing the positions of each of the instruments.

The optical layout of the MIPAS instrument is shown in Figure 3.4. Atmospheric radiance enters the instrument through the Front End Optics, comprising of azimuth and elevation scan units, which provide line-of-sight selection, as well as an internal blackbody source for calibration purposes. The field stop inside the telescope is to determine the instrument field of view (which is rectangular with dimensions of 30 km horizontal by 3 km vertical when projected onto the atmospheric limb). The radiation is then directed from the telescope into a dual-port interferometer.

In the interferometer, a beam-splitter divides the incoming radiance into two signals which are directed toward two cube corners which are moving over a 100 mm path at a constant velocity of 25 $\mathrm{mm\,s^{-1}}$. When the signals are recombined, the light waves interfere and result in an intensity-modulated signal as a function of optical path difference to provide the interferogram. From the interferometer, the

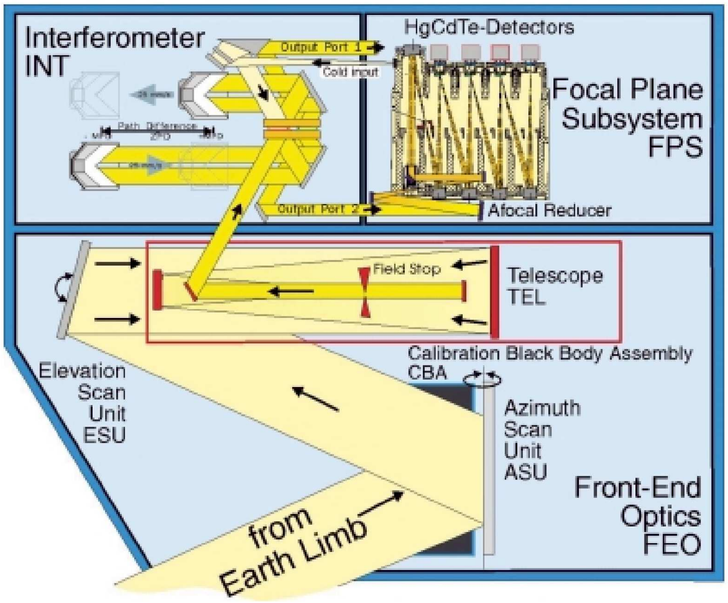

Figure 3.4: Optical layout of the MIPAS instrument (Endeman et al., 2000).

two output beams are passed to the focal place subsystem where they are reduced in size by two off-axis Newton telescopes and directed into eight HgCdTe detectors cooled to approximately 70 K by a pair of synchronised Stirling cycle coolers.

The MIPAS instrument nominally scans the atmospheric limb at tangent altitudes of 68, 60, 52, 47 km and 42 to 6 km in 3 km steps. At full spectral resolution, one complete scan of the spectrum will take 4.6 s, and a complete scan of the limb (measuring 16 spectra) will take 75 s (Endeman et al., 2000). The full, apodised, spectral resolution of each interferogram is 0.035 $cm^{-1}$ and is achievable by a maximum optical path difference of the MIPAS instrument of 200 mm (i.e. the total distance moved by the two corner cubes: 100 mm each). There are also some more specialised observing modes, discussed below, which utilise different scan patterns and reduced spectral resolution.

Spectra measured by the MIPAS instrument cover the complete thermal infrared from 685 to 2410 cm$^{-1}$ (14.6 to 4.15 $\mu$m), and are divided into five spectral bands (see Table 3.2), with each band covered by one or two of the detectors in the focal plane subsystem allowing overlap in case of detector failure. These spectral regions have strong emission lines from a number of key atmospheric species (especially carbon dioxide, ozone and water vapour), and the high spectral resolution is necessary to resolve individual emission lines. Figure 3.5 shows simulated total emission spectra in the five MIPAS spectral bands indicating the trace gases that provide the principal emission. For ozone, the strongest emission features are found in spectral bands A, AB and D.

| Band | Spectral range (cm$^{-1}$) |
|---|---|
| A | 685 - 970 |
| AB | 1020 - 1170 |
| B | 1215 - 1500 |
| C | 1570 - 1750 |
| D | 1820 - 2410 |

Table 3.2: MIPAS spectral bands.

The ENVISAT-1 spacecraft is in a Sun-synchronous polar orbit with an inclination of 98°, mean altitude of 800 km and a repeat cycle of 35 days (Louet, 2001). The MIPAS instrument nominally views the limb rearward along the orbit track of the satellite and also has the ability to observe special events (e.g. volcanic eruptions) or diurnal trace gas cycles by viewing perpendicular to the orbit track (cross-track). As mentioned above, there are a number of special observing modes, viewing different tangent altitudes and with the possibility for reduced spectral resolution, which may also be employed. These special modes will be employed for short periods of time during the MIPAS lifetime and can be used to observe different atmospheric phenomenon (e.g. polar chemistry and dynamics, impact of aircraft emissions, diurnal changes etc.). Table 3.3 gives a summary of

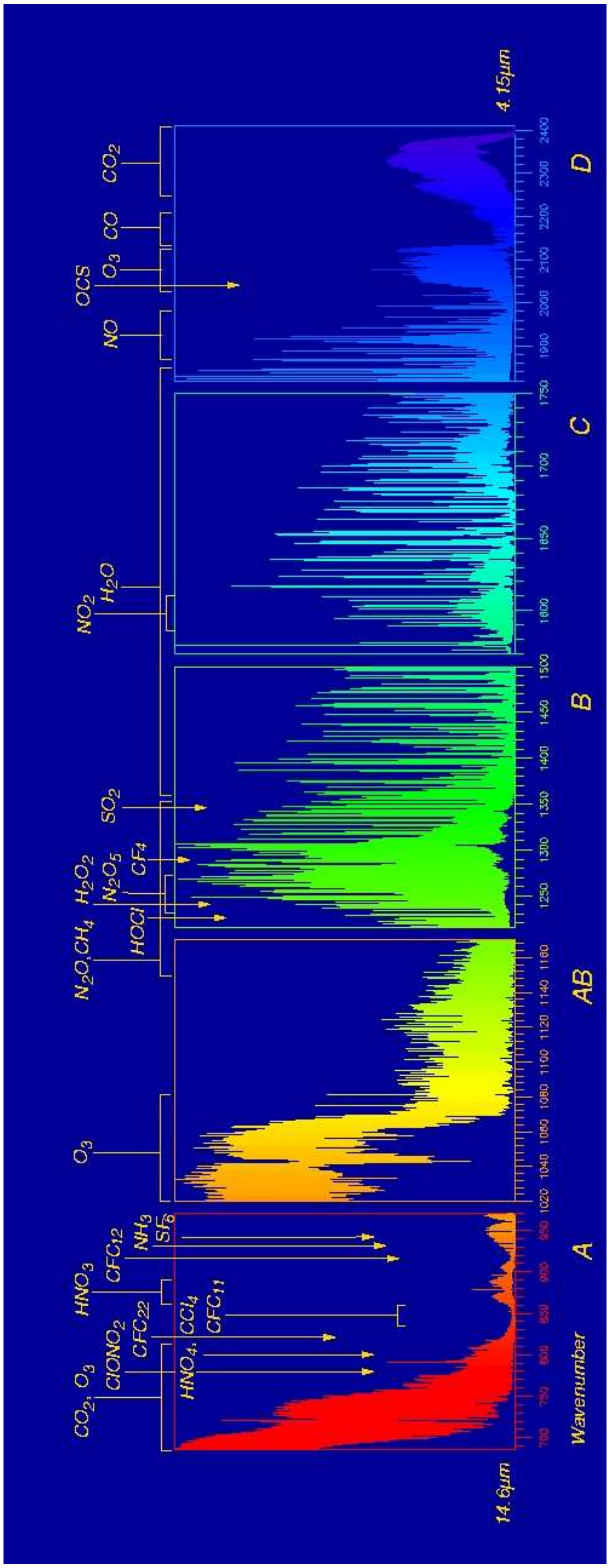

Figure 3.5: Simulated emission spectra from the atmospheric limb, calculated for each of the MIPAS spectral bands (taken from the AMIL2DA project website: http://www-imk.fzk.de:8080/imk2/ame/amil2da/).

the MIPAS observing modes available for stratospheric and UTLS applications.

| Observing mode | | Vertical spacing |
|---|---|---|
| N | r | 68, 60, 52, 47 km, 42-6 km in 3 km steps |
| S1 | r | 55, 45, 35, 30 km, 27-7 km in 2 km steps |
| S2 | r | 40, 30, 25 km, 20-5 km in 1.5 km steps |
| S3 | r/c | 40, 30, 23, 18 km, 15-6 km in 1.5 km steps |
| S4 | r | 53 km, 47-8 km in 3 km steps |
| S5 | c | 60-15 km in 3 km steps |
| S6 | r | 35, 28 km, 24-6 km in 2 km steps |

Table 3.3: Limb scan patterns employable by the MIPAS instrument. The scan patterns shown are the nominal observing mode (N) and the six special observing modes (Sx). The viewing geometry of each mode is denoted as being rearward (r) or cross-track (c).

## 3.4 Summary

In this chapter, the technical details of the three satellite instruments (ISAMS, MLS and MIPAS) of interest to this thesis have been outlined.

The main focus of this thesis is to assess the potential for retrieving information on ozone from infrared limb sounder measurements in the UTLS region of the atmosphere. Ozone retrievals from the ISAMS data are of interest for a number of reasons. Data from the ISAMS instrument were measured with a vertical spacing of 2.36 km and could provide ozone profiles with reasonable vertical resolution. The lowest tangent altitude observed by the ISAMS ozone channel was approximately 15 km, however, the extent (in terms of altitude and latitude) to which ozone can be retrieved from the ISAMS data is restricted due to contamination of the radiance signal by enhanced sulphate aerosol from the eruption of Mt. Pinatubo in mid-1991. As will be shown in chapter 4, the northern polar vortex was relatively free of aerosol during the 1991-92 winter period, and there are a large number of other data available from this time period which is useful for comparison purposes.

The limb scanning pattern of the MIPAS instrument has a lowest tangent altitude of 6 km and, therefore, provides considerable potential for retrieving information on ozone and other trace gases in the UTLS. The MIPAS instrument also has greater flexibility in the spectral regions from which information on ozone may be retrieved.

The viewing geometry of the MIPAS instrument (i.e. rearward along the satellite orbit track), indicates that it may be possible to perform 2-D retrievals on the data. A requirement for this type of retrieval is the horizontal sampling of the atmosphere that can be provided by the limb scan (i.e. the number of limb scans that lie within the instrument line-of-sight for a given tangent view). Most of the scan patterns shown in Table 3.3 have a horizontal profile spacing of between 400 and 510 km, but if the spectral resolution of each limb view is reduced, as in special observing mode S6, the horizontal spacing can be reduced to approximately 120 km. The potential for performing 2-D retrievals of ozone utilising this observing mode is assessed in chapter 7.

# Chapter 4

# Retrieval Theory

## 4.1 Introduction

Vertical profiles of geophysical parameters are derived from remote sounding observations through the inversion of the radiance signal measured by the satellite instrument (in the case of thermal emission observations). The theory and definitions used in this chapter follow Rodgers (1990, 2000). The measured signal, represented by the $m$ element *measurement vector* $\mathbf{y}$, is related to the actual state of the atmosphere, represented by the $n$ element *state vector* $\mathbf{x}$ through the *forward model* $\mathbf{F}(\mathbf{x})$, which describes the physics of the measurement process:

$$\mathbf{y} = \mathbf{F}(\mathbf{x}) + \epsilon \tag{4.1}$$

where $\epsilon$ is the measurement error. The forward model includes the physics of how the measured quantity is related to the atmospheric state as well as knowledge of how the instrument works. In order to examine the information content of a measurement it is useful to consider a linear problem[1], and equation (4.1) may be

---

[1] The problem is inherently non-linear but can be treated as linear for small departures from a defined state.

linearised about a reference state $\mathbf{x}_0$:

$$\mathbf{y} - \mathbf{F}(\mathbf{x}_0) = \frac{\partial \mathbf{F}(\mathbf{x})}{\partial \mathbf{x}}(\mathbf{x} - \mathbf{x}_0) + \epsilon = \mathbf{K}(\mathbf{x} - \mathbf{x}_0) + \epsilon \qquad (4.2)$$

This defines the $m \times n$ *weighting function* matrix $\mathbf{K}$ which represents the sensitivity of the measurement to a change in the state vector. In other words, $\mathbf{K}$ is the matrix of the derivatives of the $m$ forward model elements with respect to the $n$ state vector elements. This matrix may also be referred to as the Jacobian or the kernel matrix.

As the measured signal is subject to experimental error, the measurement error must be allowed for in a retrieval. Experimental errors can be described in terms of probability density functions (*pdf*s), using a Bayesian approach to probability, for which knowledge of the parameter under consideration is provided by the mean and variance. Different elements of a vector may be correlated, in the sense that

$$S_{ij} = E\{\epsilon_i \epsilon_j\} \neq 0 \qquad (4.3)$$

where $E$ is the expected value. The diagonal elements are the variances of the individual elements of $\mathbf{y}$ and the off-diagonal elements indicate correlations between different elements of $\mathbf{y}$. The measurement error covariance is denoted as $\mathbf{S}_\epsilon$.

It is often the case that knowledge about the state is available from, for example, climatology, in addition to the measurements. This knowledge is referred to as *a priori* information and has an associated *a priori* error covariance matrix $\mathbf{S}_a$. Since the atmospheric retrieval problem can often be ill-posed (i.e. either over or under-constrained, e.g. more measurements than unknowns and vice versa), the use of *a priori* can help constrain the problem to one that is well posed. In general, the problem does not have a unique solution and the optimal solution is selected from an infinite number of possible solutions. This optimal solution can be the 'most probable' or 'Maximum *a posteriori*' (MAP) solution:

$$\frac{\partial P(\mathbf{x}|\mathbf{y})}{\partial \mathbf{x}} = 0 \tag{4.4}$$

or the 'expected' state or the mean state averaged over its *pdf*:

$$\hat{\mathbf{x}} = \int \mathbf{x} P(\mathbf{x}|\mathbf{y}) d\mathbf{x} \tag{4.5}$$

where $P(\mathbf{x}|\mathbf{y})$ is the probability of $\mathbf{x}$ given $\mathbf{y}$. Assuming Gaussian statistics, the most probable state is the same as the the expected state since the *pdf* is symmetric about its maximum. Equation (4.2), with the origins set to $\mathbf{x}_0$ and $\mathbf{F}(\mathbf{x}_0)$ can be simplified:

$$\mathbf{y} = \mathbf{K}\mathbf{x} + \epsilon \tag{4.6}$$

If there is prior knowledge of the state and measurements are made with measurement error covariance $\mathbf{S}_\epsilon$, assumed to be Gaussian, then the expected solution of the state is derived to be:

$$\hat{\mathbf{x}} = (\mathbf{K}^T \mathbf{S}_\epsilon^{-1} \mathbf{K} + \mathbf{S}_a^{-1})^{-1} (\mathbf{K}^T \mathbf{S}_\epsilon^{-1} \mathbf{y} + \mathbf{S}_a^{-1} \mathbf{x}_a) \tag{4.7}$$

with total error covariance $\hat{\mathbf{S}}$:

$$\hat{\mathbf{S}} = (\mathbf{K}^T \mathbf{S}_\epsilon^{-1} \mathbf{K} + \mathbf{S}_a^{-1})^{-1} \tag{4.8}$$

where $\mathbf{x}_a$ is the *a priori* state vector with error covariance matrix $\mathbf{S}_a$. This solution which minimises a joint cost function which includes the measurements and *a* *priori* information:

$$\chi^2 = (\mathbf{y} - \mathbf{F}(\hat{\mathbf{x}}))^T \mathbf{S}_\epsilon^{-1} (\mathbf{y} - \mathbf{F}(\hat{\mathbf{x}})) + (\mathbf{x}_a - \hat{\mathbf{x}})^T \mathbf{S}_a^{-1} (\mathbf{x}_a - \hat{\mathbf{x}}) \tag{4.9}$$

is called the ‘Optimal Estimation’ retrieval.

## 4.2 Error Analysis and Characterisation

As mentioned above, there is no unique solution for an ill-posed retrieval problem and the optimal solution is chosen from the infinite number of possible solutions. The usefulness of a retrieval should be assessed to show how the solution relates to the true state of the atmosphere and to identify characteristics of the retrieval that can be optimised. The approaches to the characterisation and error analysis of a retrieval shown here follow the methods of Rodgers (1990, 2000). Error analysis involves evaluating the sensitivity of the retrieval to all the sources of error that can affect the retrieval: the noise in the measurement, error in the non-retrieved parameters, error in the forward model etc:

$$\frac{\partial \hat{\mathbf{x}}}{\partial \epsilon} = \mathbf{G}_\epsilon \tag{4.10}$$

where $\mathbf{G}_\epsilon$ is known as the contribution function or gain. If there is *a priori* information,

$$\mathbf{G}_\epsilon = (\mathbf{K}^T \mathbf{S}_\epsilon^{-1} \mathbf{K} + \mathbf{S}_a^{-1})^{-1} \mathbf{K}^T \mathbf{S}_\epsilon^{-1} \tag{4.11}$$

The contribution function represents how the solution is affected by a change in the measurement vector $\mathbf{y}$ since,

$$\hat{\mathbf{x}} = \mathbf{x}_a + \mathbf{G}_\epsilon (\mathbf{y} - \mathbf{K}\mathbf{x}_a) \tag{4.12}$$

Characterisation requires evaluation of the sensitivity of the retrieval to the true state:

$$\frac{\partial \hat{\mathbf{x}}}{\partial \mathbf{x}} = \mathbf{A} \tag{4.13}$$

where $\mathbf{A}$ is the *Averaging Kernel* matrix

$$\mathbf{A} = \mathbf{G}_\epsilon \mathbf{K} \tag{4.14}$$

The retrieved state is a smoothed version of the true state with smoothing functions given by the rows of $\mathbf{A}$, plus error terms:

$$\hat{\mathbf{x}} = \mathbf{x}_a + \mathbf{A}(\mathbf{x} - \mathbf{x}_a) + \mathbf{G}_\epsilon \epsilon = (\mathbf{I} - \mathbf{A})\mathbf{x}_a + \mathbf{A}\mathbf{x} + \mathbf{G}_\epsilon \epsilon \tag{4.15}$$

The rows of $\mathbf{A}$ can be regarded as smoothing functions and are generally peaked functions, with maxima at the appropriate levels and half-widths which are a measure of the spatial resolution on the observing system. The averaging kernel also has an area, approximately unity at levels where the retrieval is accurate, which can be considered as a measure of the fraction of the retrieval that comes from data (rather than the *a priori*).

The error in the retrieval consists of two parts: the noise error and the smoothing error. The noise error represents the (random) measurement noise and is given by:

$$\mathbf{S}_n = \mathbf{G}_y \mathbf{S}_\epsilon \mathbf{G}_y^T \tag{4.16}$$

The smoothing error represents the loss of fine structure in the retrieved state as a consequence of the observing system and its covariance is given by

$$\mathbf{S}_s = (\mathbf{A} - \mathbf{I}_n)\mathbf{S}_a(\mathbf{A} - \mathbf{I}_n)^T \tag{4.17}$$

where $\mathbf{S}_a$ is the error covariance of an ensemble of states about the *a priori* state. To estimate the smoothing error, the true covariance of an ensemble of states about the true state should be known. If $\mathbf{S}_a$ is a reasonable representation of the climatological covariance, then this can be used.

## 4.3 Choice of Retrieval Grid

The atmosphere and its fine structure should be represented by as fine a retrieval grid as possible. However, this will require considerable computation and there may not be enough information in the measurements to retrieve on a fine grid with sufficient accuracy. A coarse retrieval grid is faster and more efficient but 'representation errors' due to the loss of fine structure is introduced. In order to compare representation errors and choose an optimum retrieval grid, it is necessary to be able to transform between different grids.

Consider a state vector $\mathbf{x}$ on a fine grid of $n$ levels, and a reduced vector $\mathbf{z}$ on a coarser grid with $l$ levels. The state vector on the fine grid is related to the one on the coarse grid through an interpolation operator $\mathbf{W}$ ($n \times l$ matrix):

$$\mathbf{z} = \mathbf{W}\mathbf{x} \tag{4.18}$$

To transform from a general $\mathbf{z}$ to $\mathbf{x}$,

$$\mathbf{x} = \mathbf{W}^{*}\mathbf{z} \tag{4.19}$$

where $\mathbf{W}^{*}$ is a pseudo inverse of the interpolation matrix[2] $\mathbf{W}$. The $\mathbf{W}^{*}$ that minimises the loss of fine structure for an atmosphere described by $\mathbf{S}_a$ can be

---

[2] $\mathbf{W}^{*}\mathbf{W} = \mathbf{I}$, but $\mathbf{W}\mathbf{W}^{*} \neq \mathbf{I}$ as fine structure in $\mathbf{x}$ cannot be restored.

expressed as, for example:

$$\mathbf{W}^* = (\mathbf{W}^T\mathbf{S}_a^{-1}\mathbf{W})^{-1}\mathbf{W}^T\mathbf{S}_a^{-1} \tag{4.20}$$

The *a priori* error covariance matrix must also be transformed:

$$\mathbf{S}_{za} = \mathbf{W}^*\mathbf{S}_a\mathbf{W}^{*T} = (\mathbf{W}^T\mathbf{S}_a^{-1}\mathbf{W})^{-1} \tag{4.21}$$

## 4.4 Iterative Retrievals and Convergence

As noted earlier, an optimal estimation retrieval finds the most probable solution which is consistent with both the measurements and the *a priori* knowledge. The MAP solution minimises a cost function, which for Gaussian statistics is given by:

$$-2\ln P(\mathbf{x}|\mathbf{y}) = (\mathbf{y}-\mathbf{F}(\mathbf{x}))^T\mathbf{S}_\epsilon^{-1}(\mathbf{y}-\mathbf{F}(\mathbf{x})) + (\mathbf{x}_a-\hat{\mathbf{x}})^T\mathbf{S}_a^{-1}(\mathbf{x}_a-\hat{\mathbf{x}}) + \mathrm{constant} \tag{4.22}$$

using a Bayesian approach. At the minimum the gradient of the cost function is zero:

$$\nabla_\mathbf{x}\{-2\ln P(\mathbf{x}|\mathbf{y})\} = -[\nabla_\mathbf{x}\mathbf{F}(\mathbf{x})]^T\mathbf{S}_\epsilon^{-1}[\mathbf{y}-\mathbf{F}(\mathbf{x})] + \mathbf{S}_a^{-1}(\mathbf{x}_a-\hat{\mathbf{x}}) = 0 \tag{4.23}$$

Since $\nabla_\mathbf{x}\mathbf{F}(\mathbf{x}) = \mathbf{K}(\mathbf{x})$, the equation to be solved is:

$$-\mathbf{K}^T\mathbf{S}_\epsilon^{-1}[\mathbf{y}-\mathbf{F}(\hat{\mathbf{x}})] + \mathbf{S}_a^{-1}(\mathbf{x}_a-\hat{\mathbf{x}}) = 0 \tag{4.24}$$

If, in the idealised case, the forward model is linear (i.e. $\mathbf{F}(\hat{\mathbf{x}}) = \mathbf{K}\hat{\mathbf{x}}$), then the solution for $\hat{\mathbf{x}}$ simply follows as equation (4.7). If the forward model is nearly linear then it is possible to linearise the problem about some state and find a solution as above. For a non-linear problem it is necessary to numerically and iteratively find a solution which fits the measurements. The retrieval iteratively steps toward the solution until a suitable convergence criterion is reached. A suitable convergence criterion can make use of, e.g., the reduction in cost function $\chi^2$ or the gradient of the cost function. For steepest descent,

$$\mathbf{x}_{i+1} = \mathbf{x}_i - \gamma^{-1} \nabla_{\mathbf{x}} \chi_i^2 \tag{4.25}$$

where, $\gamma^{-1}$ is the step size between iterations. The Levenberg-Marquardt approach (Rodgers, 2000) uses:

$$\mathbf{x}_{i+1} = \mathbf{x}_i + (\mathbf{K}\mathbf{K}^T + \gamma_i \mathbf{I})^{-1} \mathbf{K}^T [\mathbf{y} - \mathbf{F}(\mathbf{x}_i)] \tag{4.26}$$

As $\gamma \rightarrow 0$, this tends to the Newton iteration method (Jay, 2000; Rodgers, 2000), and as $\gamma \rightarrow \infty$, this tends to the steepest descent method. Values of $\gamma$ are chosen to give steepest descent far from the solution, Newtonian iteration near the solution, and are assessed by monitoring $\chi^2$ (Jay, 2000). An example of a suitable convergence test is for the size of the step in state space to be small compared to the retrieval error (Jay, 2000):

$$\chi^2 = (\hat{\mathbf{x}}_n - \hat{\mathbf{x}}_{n+1})^T \hat{\mathbf{S}}^{-1} (\hat{\mathbf{x}}_n - \hat{\mathbf{x}}_{n+1}) << n \tag{4.27}$$

## 4.5 Applications to Satellite Observations

The approach to be adopted for performing retrievals from satellite observations is dependent upon the type of instrument making the measurement. In the case of a radiometer, such as the ISAMS experiment, measurements are made at fixed spectral regions or channels optimised for each target species. The new generation of remote sounding instruments, such as the Fourier transform or grating spectrometers MIPAS, AIRS, TES or IASI, will provide measurements that cover wide frequency ranges at high spectral resolution. The most effective and efficient way of using these large quantities of data requires the selection of the optimum spectral region, or regions, for the retrieval of each geophysical parameter. These spectral regions are referred to as *microwindows*, and the selection of microwindows is described in the following section.

## 4.6 Microwindow Selection

Fourier transform spectrometers, such as the MIPAS instrument, use a large number of channels, up to $10^6$ in some cases, to measure atmospheric spectra over wide frequency ranges at high spectral resolution. The computational effort required to invert large spectral regions is inefficient and impractical, and including spectral regions which are not well reproduced by the forward model could deteriorate the retrieval (von Clarmann and Echle, 1998). The most efficient way to use this data is to select the optimal spectral regions or *microwindows* for each target species to be retrieved. A microwindow contains a limited number of spectral points, and its width is limited by the presence of spectral lines of other traces species which do not contribute any significant information to the retrieval. Microwindows have advantages over the use of single spectral points, including more efficient forward model calculations, as convolution of a calculated spectrum with the instrument line-shape function requires that radiances are calculated at a number of consecutive spectral points.

### 4.6.1 Approaches to microwindow selection

Methods for the selection of microwindows have often been carried out on an ad hoc basis although in recent years more objective and reproducible methods have been developed. Selection of individual channels, which can also be extended to microwindows, can be based on the data resolution matrix (DRM) (Menke, 1984) or the characteristics of the Jacobian, although analysis of these two methods, compared to an iterative approach based on the information content (described below), for temperature retrievals from the IASI instrument showed that channels selected iteratively performed best (Rabier et al., 2002). The information content provides the best measure of the information available when using a particular measurement in the retrieval as it is a measure of how the retrieval error is improved when the measurement is included (see next section). The use of information content in selecting channels for the AIRS instrument, based on the retrieval random errors, was presented in (Rodgers, 1998). For the operational processing of the MIPAS data, sets of microwindows for each target species are selected, optimised in both the spectral and altitude domains. The set of microwindows selected for the operational processing of the MIPAS data are selected using the Oxford University developed software MWMAKE (see the MWMAKE user's guide (Dudhia, 2001)). This method selects a start point by calculating a *figure of merit*, based on the Shannon information content, taking into account the random and systematic errors and the CPU cost, for each measurement and selecting the best one. A microwindow is then grown by assessing the figure of merit of adjacent points and expanding the microwindow in the direction that provides the most improvement. A microwindow stops growing when the inclusion of further point results is a lower figure of merit or when some predefined size limit is reached (Dudhia et al., 2002; Jay, 2000).

### 4.6.2 Information content

The information content of a measurement may be defined as the reduction in the uncertainty of the retrieval when the measurement is used. For inverse methods, there are two widely used measures of information which are defined below: the Fisher information matrix and Shannon information content.

#### The Fisher information matrix

The Fisher information matrix arises in the theory of maximum likelihood estimation, where likelihood, as defined by Fisher, is the conditional *pdf* $P(\mathbf{y}|\mathbf{x})$, i.e. the probability of $\mathbf{x}$ given $\mathbf{y}$. A maximum likelihood estimator finds the value of $\mathbf{x}$ which maximises $P(\mathbf{y}|\mathbf{x})$. In the context of the Bayesian approach, it is the same as the posterior *pdf* $P(\mathbf{x}|\mathbf{y})$ when there is no prior information. It can be shown that the information matrix of a product of two independent likelihoods, i.e. $P(\mathbf{y}_1|\mathbf{x})P(\mathbf{y}_2|\mathbf{x})$, is the sum of the individual matrices, so that the information of two independent measurements is additive. More information on the nature of the Fisher information matrix is given in Rodgers (2000).

#### Shannon information content

In this thesis the information content is that defined by Shannon as being the reduction in the entropy of a probability density function (or *pdf*). A *pdf* is used as a measure of the knowledge of a system (e.g. *a priori* information), and the Shannon definition of entropy is similar to that of the Gibbs definition of thermodynamic entropy:

$$S(P) = -k \sum_i p_i \ln p_i \tag{4.28}$$

where $p_i$ is the probability of the system being in state $i$. In thermodynamics the variable $k$ is Boltzmann's constant, and in information theory it is equal to $1/\ln 2$.

For a continuous *pdf*, $p_i$ corresponds to $P(x)\,dx$ and the entropy is defined as

$$S(P) = -\int P(x)\log_2[P(x)/M(x)]\,dx \tag{4.29}$$

$M(x)$ is a measure function and taken to be a constant. The logarithm to the base 2 is used to express the entropy in ‘bits’. If the knowledge of the system before a measurement is $P_1(x)$, and knowledge afterwards is $P_2(x)$, the information content is the reduction in entropy:

$$H = S(P_1(x)) - S(P_2(x)) \tag{4.30}$$

It can be shown (e.g. Rodgers (2000)) that for Gaussian statistics, $S(P) = \frac{1}{2}\log_2|\mathbf{S}|$, so that the information content is:

$$H = \frac{1}{2}\log_2|\mathbf{S}_1| - \frac{1}{2}\log_2|\mathbf{S}_2| = \frac{1}{2}\log_2|\mathbf{S}_1\mathbf{S}_2^{-1}| \tag{4.31}$$

The Shannon information content provides a single value that describes the ‘quality’ of a measurement and has been used in previous studies to find optimal radiometer configurations (Peckham, 1974) and to compare the performance of instruments and combinations of instruments (Eyre, 1990) as well as for the selection of spectral channels as described in Rodgers (1998).

## 4.7 Summary

This chapter has briefly outlined the theory behind the inversion of radiance measurements required to retrieve information on the distribution of geophysical parameters. This theory is discussed in much greater detail in, for example, Rodgers (1990, 2000). Particular attributes of this theory when applied to satellite limb sounding observations have also been discussed with particular emphasis on the role of information theory for the optimised selection of channels/microwindows from high spectral resolution observations provided by the MIPAS instrument, amongst others. Selection of microwindows, using information theory, for the retrieval of ozone from the MIPAS instrument is discussed in more detail in chapter 7.

# Chapter 5

# UARS Observations of Ozone in the Lower Stratosphere

In the previous chapters, the importance of ozone, and the physical and chemical processes controlling its distribution, in the upper troposphere and lower stratosphere region of the Earth's atmosphere have been introduced. Satellite infrared limb sounder observations have the potential to provide continuous near-global measurements of trace gases in this region of the atmosphere. These observations are preferred as they can provide reasonable vertical resolution (approximately 2.36 km in the case of ISAMS), which is desirable in the UTLS where there are steep gradients in the vertical distribution of ozone. In this chapter the potential for sounding ozone in the lower stratosphere is assessed through the retrieval of ozone from data measured by the ISAMS instrument in the lowermost stratosphere during the 1991-92 Northern hemisphere winter.

## 5.1 The 1991-92 Northern Hemisphere Winter

The 1991-92 Northern hemisphere winter was a marginally cold winter with sporadic PSCs. It is an interesting period because, studies of ozone in the lower stratosphere polar vortex are facilitated by both the large number of measurements from the NASA Upper Atmosphere Research Satellite (UARS), launched on September 12 1991, and two extensive measurement campaigns: the European Arctic Stratospheric Ozone Experiment (EASOE) (Pyle et al., 1994), and the second Airborne Arctic Stratospheric Experiment (AASE-II) (Anderson and Toon, 1993). PSC activity in this winter was observed by ISAMS in two episodes during late December and early January, separated by approximately one week. Particular dates on which PSCs were observed by ISAMS are December 28 1991 and January 9 and 10 1992 (Taylor et al., 1994). These PSCs were observed at 46 hPa and were shown to occur over the North Atlantic and Scandinavia on each date.

Ozone measured by the ISAMS instrument on UARS during this winter provides a useful dataset for a number of reasons. Firstly, for assessing the potential for retrieving ozone information in the lower stratosphere from infrared limb sounder observations, data from the MLS instrument on UARS provides the best dataset to validate ISAMS ozone retrievals in the Arctic lower stratosphere. The MLS has provided a more or less continuous, and well validated (against, for example, SAGE II), ozone dataset from the launch of UARS until mid-2000, and ozone information from the MLS is also retrieved from limb thermal emission observations with the profiles being co-located spatially and temporally to the ISAMS profiles. Data from instruments such as SAGE II and HALOE are not useful for validating the ISAMS retrievals as they cannot provide the required latitudinal coverage due to the nature of solar occultation observations. Secondly, comparison of this ISAMS data to ozonesonde data from the EASOE and AASE-II campaigns will, as well as providing validation of the ISAMS data, provide an understanding of how best to use ozonesonde data with satellite limb sounder data which will be useful for future satellite missions.

The ISAMS experiment performed limb sounding observations of ozone spectrally-integrated radiance between 990 and 1010 cm$^{-1}$ (channel 33W, see chapter 2) with an intrinsic signal-to-noise ratio of approximately 1000:1 (Connor et al., 1996). As described in chapter 3, ozone measurements were made from a wide-band signal in one of the $\mathrm{CO_2}$ cells with a filter wheel employed to select between $\mathrm{CO_2}$, $\mathrm{HNO_3}$ and ozone. This led to ozone only being measured in the first quarter of each EMAF (see Figure 3.2). The tangent altitude range of these radiance measurements is 100 to 0.1 hPa. In an aerosol free atmosphere, the 33W radiance measurements should contain ozone information down to the lower stratosphere. However, the eruption in June 1991 of Mt. Pinatubo in the Philippines significantly increased sulphate aerosol levels in the lower stratosphere, which contaminated the radiance signals and reduced the sensitivity to ozone. In the Northern hemisphere winter of 1991-92, the polar vortex was relatively free of Pinatubo aerosol until mid-January (Rosen et al., 1992). This provides a good region in which to study ISAMS retrievals of ozone in the lower stratosphere.

## 5.2 Retrievals from the ISAMS Data

ISAMS constituent retrievals are performed using one of two retrieval schemes: LV2CON or LV2VMR. Radiances are measured by ISAMS every 2.048 s[1] (or Instrument Measurement Period (IMP), as described in chapter 3) and constituent retrievals are performed after temperature and pressure have been retrieved using a Kalman filter along the measurement track (Rodgers et al., 1996). The LV2CON retrieval scheme inverts pre-gridded radiances (provided by a separate routine:

---

[1] Ozone measurements share sampling time with temperature and $\mathrm{HNO_3}$ measurements via a programmable rotating filter wheel, with approximately 25% of the filter wheel cycle dedicated to ozone (Connor et al., 1996).

LV2RAD) to produce vertical profiles at regular intervals along the measurement track. Constituent profiles are then retrieved at each location individually. The LV2VMR retrieval scheme, on the other hand, uses a sequential method which, instead of gridding the radiances, employs the radiance available for each IMP to retrieve temperature and update the constituent profile. The latter is similar to the method used in the ISAMS temperature retrieval (Dudhia and Livesey, 1996). The retrievals presented in this chapter are performed with the LV2CON scheme.

The v10 operational ISAMS ozone retrievals were performed using the optimal onion-peeling technique (Connor and Rodgers, 1989; Marks and Rodgers, 1993). This technique steps down through the atmosphere, retrieving products at each tangent level using the radiances from just that level and the values of the already retrieved products above the tangent point (Marks and Rodgers, 1993). This prevents systematic errors (e.g. due to the aerosol correction) lower in the profile from propagating upward. A vector-vector technique, which is the process of updating a profile vector with a measurement vector (i.e. limb-scan) in one operation, should be more accurate than an optimal onion-peeling technique as it simultaneously fits all the radiances, combining information on a given level from all tangent heights (see section 5.3.2).

## 5.3 Low Aerosol Region

To determine ozone most accurately in the polar lower stratosphere from the ISAMS data, it is preferable to employ a vector-vector optimal estimation scheme in the relatively low aerosol region. A low aerosol region is defined using the ISAMS v12 12.1 $\mu$m aerosol extinction. This data was retrieved using the Marquardt vector-vector method (Marks and Rodgers, 1993) to invert radiances measured in an atmospheric window, i.e. a spectral region that is relatively free of molecular band emissions (Lambert et al., 1996). Figure 5.1 shows the zonal mean ISAMS v12 12.1 $\mu$m aerosol extinction ($\times 10^{-8}$ m$^2$ mol$^{-1}$) for December 6 1991 and January 9 1992. The zonal mean aerosol extinction varies between 2 and $8\times10^{-8}$ m$^2$ mol$^{-1}$ at high latitudes (70 to 80° N) between UARS pressure surfaces 6 and 12. In the lower stratosphere (UARS surfaces 6 to 9), the zonal mean aerosol extinction varies between 3 and $8\times10^{-8}$ m$^2$ mol$^{-1}$, and the threshold to define the low aerosol region is taken to be between these values, depending on the UARS pressure surface. Figure 5.2 shows the geographical extent and evolution of the 12.1 $\mu$m aerosol extinction, on alternate days from December 6 1991 through to January 13 1992, on UARS pressure surface 7 (68 hPa).

### 5.3.1 Aerosol correction in the ISAMS ozone retrieval

To assess the impact, if any, of correcting for sulphate aerosol on the ISAMS ozone retrievals in the low aerosol region, the optimal onion-peeling technique was used to retrieve ozone for January 9 1992 with and without aerosol correction. Figure 5.3 shows the zonal mean ratio of the ozone retrieval with and without aerosol correction for January 9 1992. The zonal mean of the ratio of the two ozone retrievals is calculated only for profiles at latitudes greater than 65° N and within the low aerosol region. The ISAMS data are flagged with negative errors if the recorded value should be treated with caution, e.g. large dependence on the *a priori* by the retrieval, and these data are not included in the zonal mean calculation. In the lower stratosphere at high latitudes the zonal mean ratio shows that the difference in the retrieval of ozone with and without an aerosol correction is 3% to 7% between UARS surfaces 7 and 9, and of the order of 10% at the lowest level. Figure 5.3 indicates that the aerosol correction does not have a signifcant effect on the ozone retrieval down to pressure surface 8 (46 hPa). The retrieval at

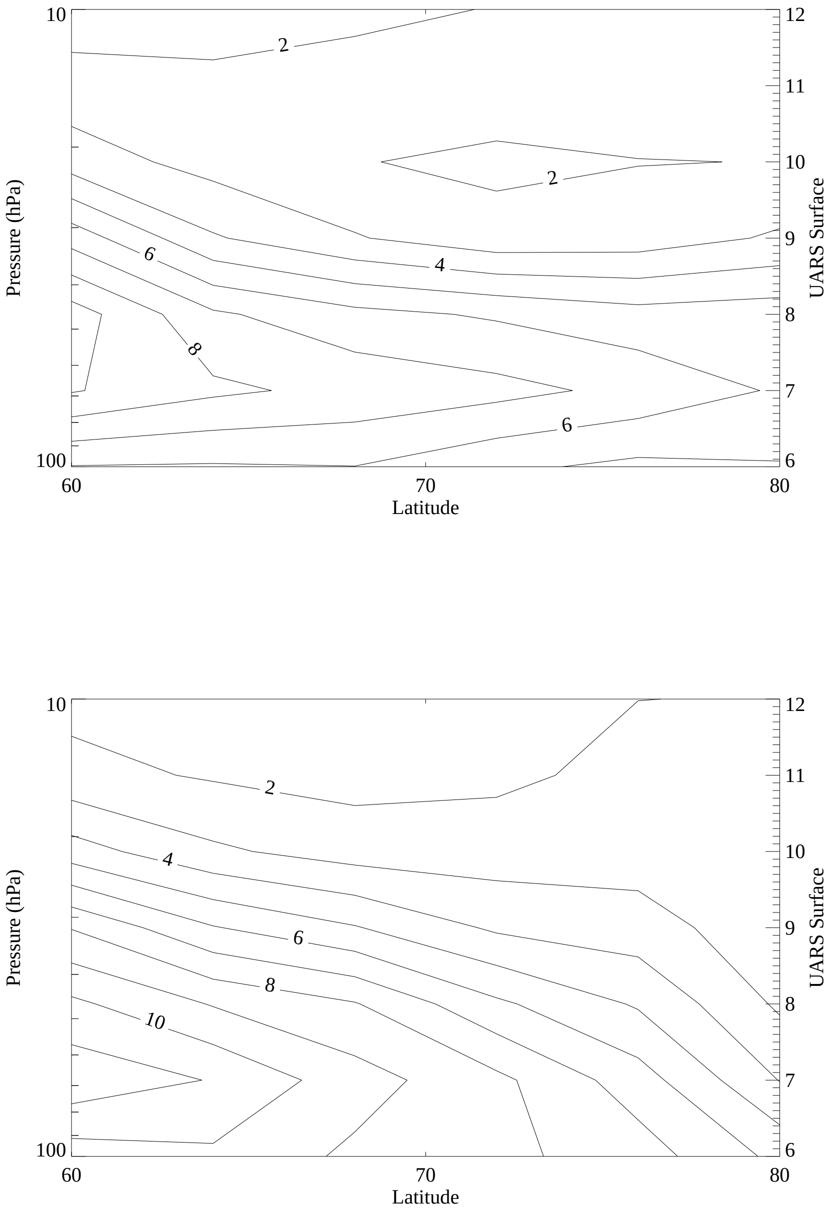

Figure 5.1: ISAMS zonal mean 12.1$\mu$m aerosol extinction ($\times 10^{-8}$ m$^2$ mol$^{-1}$) on December 6 1991 (upper plot) and January 9 1992 (lower plot).

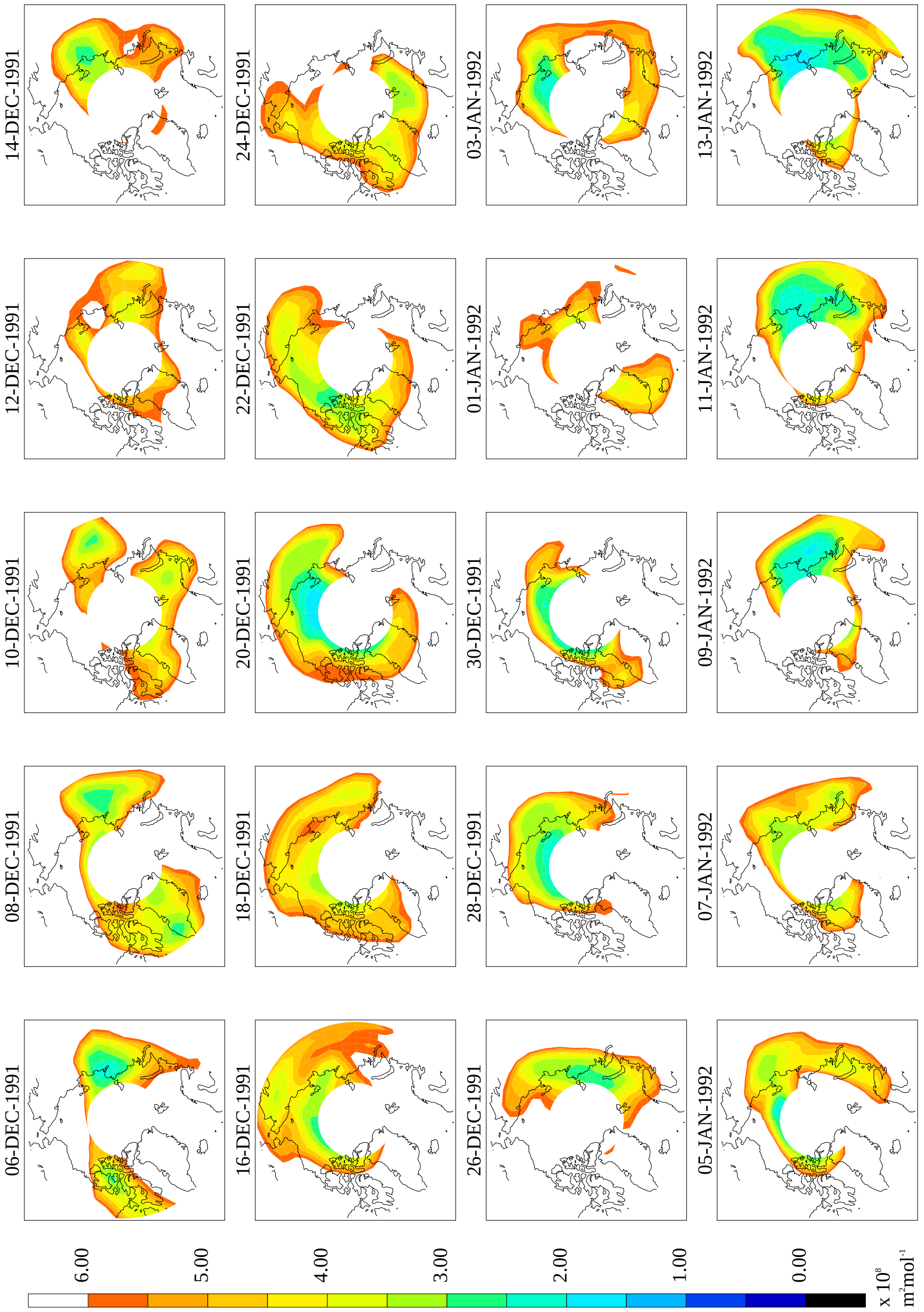

Figure 5.2: Evolution of the Arctic low aerosol region, defined by the ISAMS 12.1 $\mu$m extinction, on UARS pressure surface 7 (68 hPa) from December 6 1991 to January 13 1992 in two day intervals. Only aerosol values less than $6\times10^{-8}$ m$^{2}$ mol$^{-1}$ are shown to clearly indicate the geographical extent of the lowest aerosol values. Note that the ISAMS did not make any observations north of 80°.

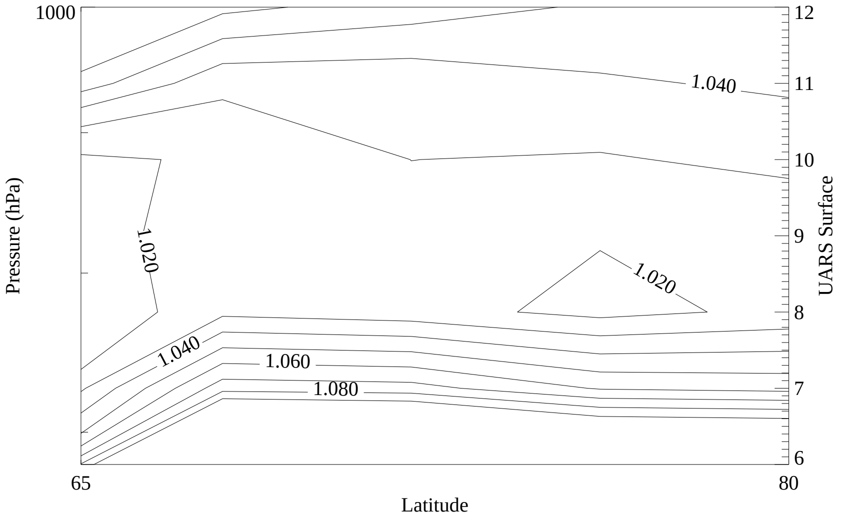

Figure 5.3: Zonal mean ratio of ozone retrievals from ISAMS with the optimal onion-peeling technique with:without aerosol correction in the low aerosol region on January 9 1992. These retrievals were both performed with the LV2CON retrieval scheme.

pressure surfaces 6 and 7 (100 and 68 hPa) is likely to show increasing aerosol effects. Down to 46 hPa it is reasonable not to include any aerosol correction in the ozone retrieval. This is desirable as the aerosol correction could itself be a source of uncertainty in the ozone retrieval. In all the retrievals performed in this chapter, aerosol correction is not included.

### 5.3.2 Vector-vector ozone retrieval

As mentioned above, it is desirable to use the vector-vector technique to perform ozone retrievals in the low aerosol region. This is due to the vector-vector technique retrieving at all profile levels simultaneously and hence preventing potential retrieval errors in the optimal onion-peeling technique from propagating to other retrieval levels. New ozone retrievals were performed from the ISAMS data from December 6 1991 to January 13 1992 using the vector-vector technique in the

LV2CON retrieval scheme. Figure 5.4 shows the zonal mean ratio of MLS ozone to the ISAMS vector-vector retrieval of ozone in the low aerosol region for January 9 1992. The ozone retrieved with the vector-vector technique is within 20%

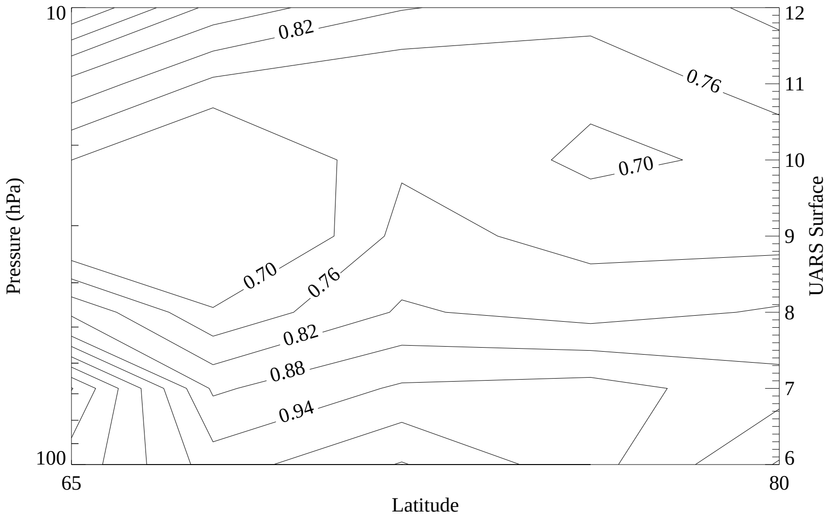

Figure 5.4: Zonal mean ratio of MLS v5 ozone to ISAMS ozone retrieved with the vector-vector technique in LV2CON on January 9 1992.

of the MLS v5 ozone at the highest latitudes and between UARS pressure surfaces 6 to 8. Given the known characteristics of the MLS v5 ozone at lower latitudes (where it has been extensively validated) (Livesey et al., 2003), this indicates that the vector-vector technique does a reasonable job of retrieving ozone at the lowest levels. The ISAMS ozone retrieval is characterized by its averaging kernels. Figure 5.5 shows averaging kernels for an ISAMS ozone profile retrieved on December 12 1991 at 79.66° N and 312.49° E. These averaging kernels are typical of an ISAMS ozone retrieval in the polar winter and provide an indication of the influence of the *a priori* on the retrieval as well as the vertical resolution intrinsic to the ISAMS retrievals in this particular region. An unrealistic *a priori* uncertainty of 75% is assumed in the ozone retrieval in order to minimize bias in the retrieval by the *a priori* (Connor et al., 1996). In the lower stratosphere (UARS pressure surfaces 6, 7, 8 and 9), the averaging kernels have peak values between approximately 0.45 and 0.5 with full width half maximum values between approximately 3 and 5 km. The ISAMS ozone retrieval validation paper (Connor et al., 1996) reported ozone averaging kernel peak values between 0.4 and 0.6 and vertical resolution of approximately 3 km in the stratosphere (between 10 and 1 hPa).

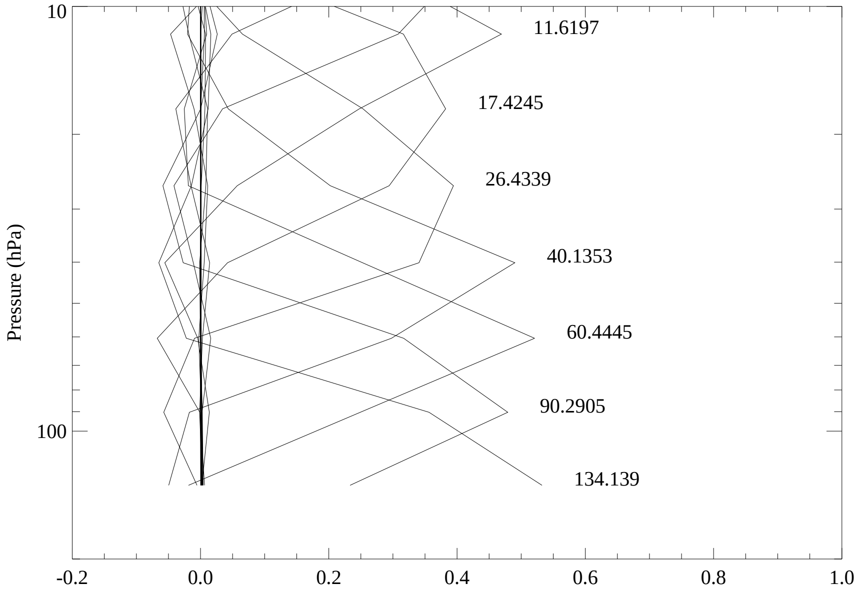

Figure 5.5: Averaging kernels for an ISAMS ozone profile retrieved by the LV2CON vector-vector scheme at 79.66° N and 312.49° E on December 12 1991.

## 5.4 Inter-comparison with Other Ozone Data

As noted above, a substantial amount of data is available in the lower stratosphere for the 1991-92 Arctic winter period. In this section the ozone retrievals performed from the ISAMS data are compared to ozonesonde data, available from the EASOE and AASE-II measurement campaigns, and MLS v5 ozone data.

### 5.4.1 Ozonesonde data

During the EASOE and AASE-II measurement campaigns, a large number of ozonesondes were launched throughout the winter period providing atmospheric ozone profiles with high vertical resolution. All of the ozonesondes launched during these campaigns were of the ECC type and provided by Atmospheric Environment Service (AES), Canada.

Ozonesondes are small, lightweight, balloon-borne instruments capable of making measurements from the surface up to altitudes of approximately 35 km. There are three main types of ozonesonde: Brewer-Mast, electro-chemical concentration cell (ECC) and Japanese (or carbon-iodine) ozonesonde. The principle of the ozone measurement by an ozonesonde is based on the titration of ozone in a potassium iodide (KI) solution according to the following redox reaction:

$$2\mathrm{KI} + \mathrm{O_3} + \mathrm{H_2O} \longrightarrow \mathrm{I_2} + \mathrm{O_2} + 2\mathrm{KOH} \tag{5.1}$$

A small electrically driven air sampling pump forces air through the sensing solution bringing the generated ‘free’ iodine ($I_2$) into contact with a platinum cathode where it is converted to $I^-$ through the uptake of two electrons. Therefore, each ozone molecule detected produces two electrons which can be detected as an electric current $I_M$ ($\mu$A). Knowing the background current $I_B$ ($\mu$A), gas volume flow rate $\phi_P$ (cm$^3$ s$^{-1}$) of the air sampling pump, its temperature $T_P$ (K) and the conversion efficiency of the ozone sensor $\eta_C$, the partial pressure of ozone $p(\mathrm{O_3})$ (mPa) can be determined:

$$p(\mathrm{O_3}) = 0.04307\eta_C \frac{T_P}{\phi_P}(I_M - I_B) \tag{5.2}$$

Ozone partial pressure is converted to ozone volume mixing ratio $r_{\mathrm{O}_3}$:

$$r_{\mathrm{O}_3} = \frac{p(\mathrm{O}_3)}{p} \tag{5.3}$$

More information on the principle of operation of the different types of ozonesonde instruments is given by Smit (2002).

The performance of the major types of ozonesonde have been assessed by the Juelich Ozonesonde Inter-comparison Experiment (JOSIE), in February/March 1996 (SPARC, 1998). In this experiment, ozonesonde measurements made in the environment simulation chamber at the Research Centre Juelich in Germany were compared to a reference UV-photometer measurement. The deviation of the AES ECC sondes from the UV-photometer was within 10%. However, there are two sources of uncertainty that can affect the ozone measured using ECC sondes, especially in the middle stratosphere: uncertainties in the pump efficiency of the sonde, and the amount of sensing solution that has evaporated. The efficiency with which air is pumped through the sensor is dependent on the temperature and ambient pressure encountered during a flight. Also, by the time a sonde reaches the middle stratosphere it has been operating for nearly 90 minutes. The sensing solution evaporates at a rate dependent on the temperature of the cell and the ambient pressure during the flight. Therefore, due to evaporation, the concentration of the sensing solution increases which affect the sensitivity of the sonde and, hence, the amount of ozone detected. There are other sources of uncertainty, e.g. due to pre-launch preparation, but the errors are not expected to be significant here. The precision of ozonesonde measurements is taken to be 3% (SPARC, 1998).

Figure 5.6 shows the geographical locations of the ozonesonde launch stations used in this comparison study. More precise information on the latitude, longitude and number of ozonesondes launched at each station between December 6 1991 and January 13 1992 is shown in Table 5.1.

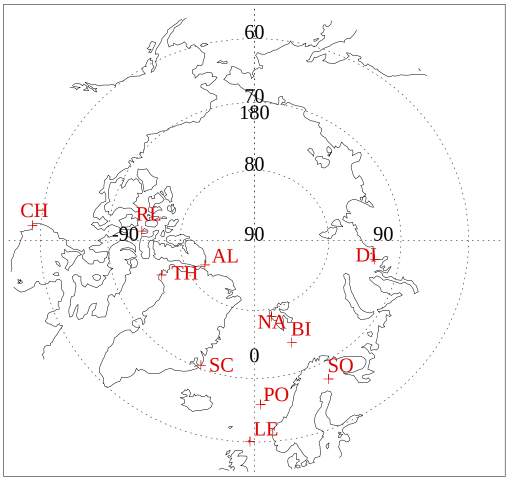

Figure 5.6: Geographical distribution of the ozonesonde launch stations providing data for comparison to the ISAMS retrievals presented in this chapter.

| Station name | Latitude (° N) | Longitude (° E) | Number |
|---|---|---|---|
| Alert (AL) | 82.5 | -62.3 | 19 |
| Bear Island (BI) | 74.5 | 19.0 | 9 |
| Churchill (CH) | 58.7 | -94.1 | 8 |
| Dikson Island (DI) | 73.5 | 80.4 | 4 |
| Lerwick (LE) | 60.1 | -1.2 | 10 |
| Ny Aalesund (NA) | 78.9 | 11.9 | 15 |
| Polarfront (PO) | 66.0 | 2.0 | 12 |
| Resolute (RL) | 74.7 | -95.0 | 8 |
| Scoresbysund (SC) | 70.5 | -22.0 | 9 |
| Sodankyla (SO) | 67.4 | 26.7 | 12 |
| Thule (TH) | 76.5 | -68.5 | 10 |

Table 5.1: Ozone sounding stations used during the EASOE and AASE-II campaigns and the number of sondes used for the comparison to the UARS data.

### 5.4.2 MLS v5 ozone data

As described in chapter 3, the Microwave Limb Sounder (MLS) (Barath et al., 1993) on UARS provided vertical profiles of geophysical data retrieved from observations of millimetre-wave thermal emission from the atmospheric limb. Ozone retrievals were performed on data measured by the 183 and 205 GHz radiometers. The data used here is that measured by the 205 GHz radiometer, which is recommended for studies of ozone in the stratosphere due to better calibration and accuracy over the 183 GHz radiometer (Livesey et al., 2003). The latest version of the MLS 205 GHz ozone is v5, for which ozone is retrieved at every UARS pressure surface (in the previous version retrievals were made on alternate pressure surfaces) and the recommended vertical range extends from 100 to 0.2 hPa. The data is in the UARS standard L3AT format, which provides profiles for specific times common for data from all UARS instruments. As with the ISAMS data, values with a negative error value are discarded. In the lower stratosphere (UARS surfaces 6 to 9), the MLS ozone retrieval has a vertical resolution of 3.5 to 4 km and an estimated precision of 8 to 20% (UARS surfaces 9 to 7) and 50% for surface 6 (Livesey et al., 2003).

### 5.4.3 Objective and methodology

The objective for inter-comparing ISAMS with MLS and ozonesonde data is to demonstrate the usefulness of the ISAMS data in providing ozone information in the Arctic lower stratosphere.

Figure 5.6 shows that the geographical distribution of ozonesonde stations is relatively sparse compared to the number of profiles measured by the UARS instruments. Figure 5.7 shows typical tangent point locations for the ISAMS (red crosses) and MLS (green crosses) instruments at latitudes greater than 65° N during one day.

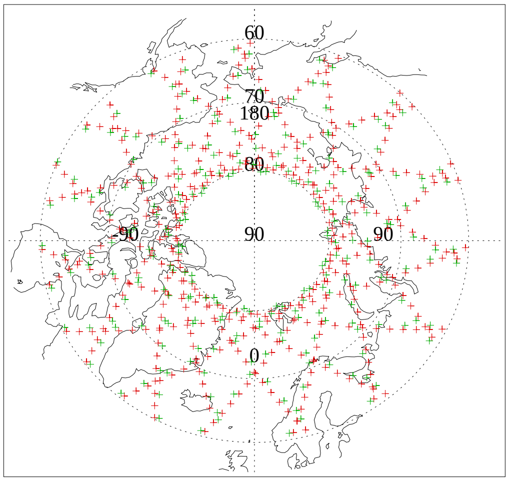

Figure 5.7: Profile locations for ISAMS (red crosses) and MLS (green crosses) at latitudes greater than 60° N on December 6 1991.

In order to compare the UARS data to each ozonesonde measurement, UARS profiles are selected within specified ranges to the latitude, longitude and time (i.e. date and time of day) of launch of each ozonesonde. When the latitude, longitude and time of the closest ISAMS profile(s) to the ozonesonde measurement has been determined, the ISAMS 12.1 $\mu$m aerosol at each pressure surface is compared to the aerosol threshold value of $6\times10^{-8}$ $m^2\,mol^{-1}$. This automatically removes any effects due to the formation of thick PSCs. Ozone values with a retrieved uncertainty greater than 50% are not included in the comparison as this indicates a large dependence by the ISAMS retrieval on the *a priori*.

### Vertical resolution

Retrieved products from the ISAMS and MLS data are gridded vertically onto standard UARS pressure surfaces, whereas ozonesonde measurements have considerably finer vertical resolution. For comparison purposes, it is necessary to degrade the vertical resolution of each ozonesonde profile to the same vertical resolution as the UARS profiles through convolution with the satellite averaging kernels. This allows the information contained in the vertical structure of the ozonesonde profile to be utilised in an optimum way. Comparison of the satellite data to the smoothed ozonesonde data allows the bias due to different vertical resolutions and the use of *a priori* data to be reduced (Hoogen et al., 1999). For a retrieval from satellite data, in the linear limit, the retrieved profile is related to the true profile and the *a priori* by, assuming $(\mathbf{x} - \mathbf{x}_a)$ is small enough for the linear approximation to hold (Rodgers, 1990):

$$\hat{\mathbf{x}} = \mathbf{x}_a + \mathbf{A}(\mathbf{x} - \mathbf{x}_a) \tag{5.4}$$

where, $\hat{\mathbf{x}}$ is the expected state, $\mathbf{x}_a$ is the satellite *a priori* state, $\mathbf{A}$ is the satellite averaging kernel matrix and $\mathbf{x}$ is the ‘true’ state. In equation (5.4), $\mathbf{x}$ is the ozonesonde profile interpolated onto the UARS pressure surfaces via the following operation (as detailed in chapter 4):

$$\mathbf{x} = \mathbf{W}^*\mathbf{z} \tag{5.5}$$

where, $\mathbf{z}$ is the ozonesonde profile on its original vertical grid and $\mathbf{W}^*$ is the pseudo-inverse interpolation matrix to transform between the high resolution ozonesonde grid and the coarser resolution UARS grid.

### 5.4.4 Results

Figures 5.8, 5.9, 5.10 show comparisons of ozone profiles measured by ISAMS, MLS and ozonesondes at different measurement locations on December 12 1991, and January 1 and 8 1992 respectively. In each figure, the top two plots show the ISAMS retrieved ozone (left) and temperature (right) at 68 hPa (UARS pressure surface 7) with blue crosses showing the geographical location of the profile comparisons in the lower four plots. The profile comparisons show the high resolution ozonesonde profile (dashed black line), the ozonesonde profile smoothed by the ISAMS averaging kernels (black diamonds) with error bars showing the quoted ozonesonde measurement precision of $\pm 3\%$, and the co-located ISAMS (red triangles) and MLS (green squares) profiles with their associated $1\sigma$ error bars. The latitude and longitude of the co-located UARS profiles are shown in the legend of each plot with the distance (km) and time (hours) difference between the UARS observation and the ozonesonde measurement.

In each of these figures, the profile comparisons show that at the lower pressure surfaces, there appears to be a reasonable agreement between the ozonesonde and UARS profiles to within the $1\sigma$ error bars. The plots in Figure 5.8 show data from an early stage of the winter period, with a minimum temperature (retrieved) of 200 K (i.e. higher than the threshold temperature for PSC formation). All of the profiles shown are within a maximum time difference of 7 hours and a maximum distance of 350 km. The profiles co-located to Alert show the best agreement at all pressure surfaces whereas the other profiles show some divergence at higher altitudes although the agreement in the lowermost stratosphere (100, 68 and 46 hPa) are within the $1\sigma$ error bars. The plots in Figure 5.9 show data from a more intermediate stage of the winter period with a minimum temperature of approximately 198 K, which is closer to the threshold temperature for PSC formation. The co-

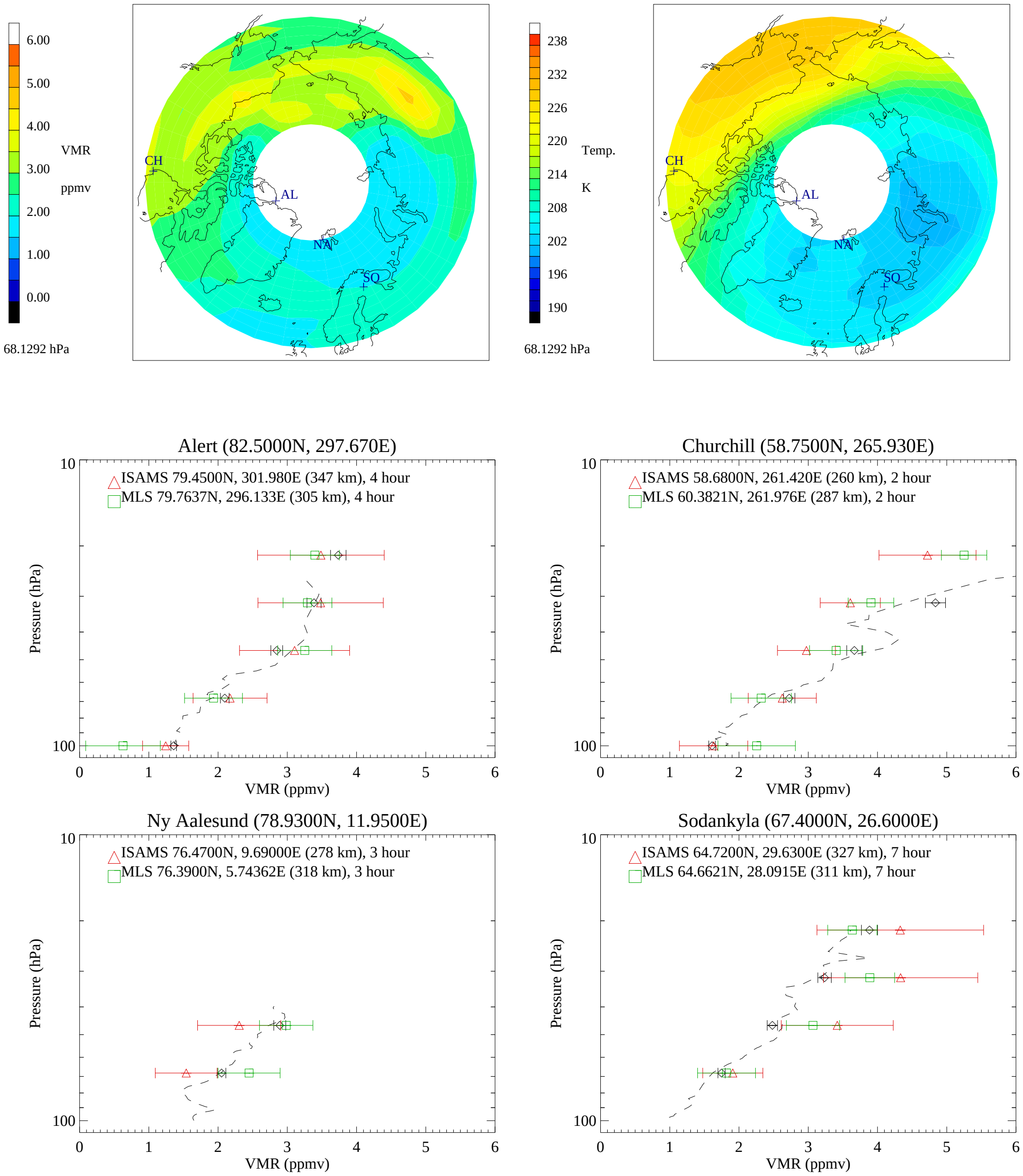

Figure 5.8: Comparison of co-located ISAMS, MLS and ozonesonde profiles on December 12 1991. The top two plots show the ISAMS retrieved ozone (left) and temperature (right) at 68 hPa (UARS pressure surface 7). The lower four plots show the profiles at the four stations marked on the maps with crosses: Alert, Churchill, Ny Aalesund and Sodankyla. The red triangles, green squares and black diamonds represent the ISAMS, MLS and smoothed ozonesonde profiles respectively, and the original ozonesonde profile is shown by the dashed black line.

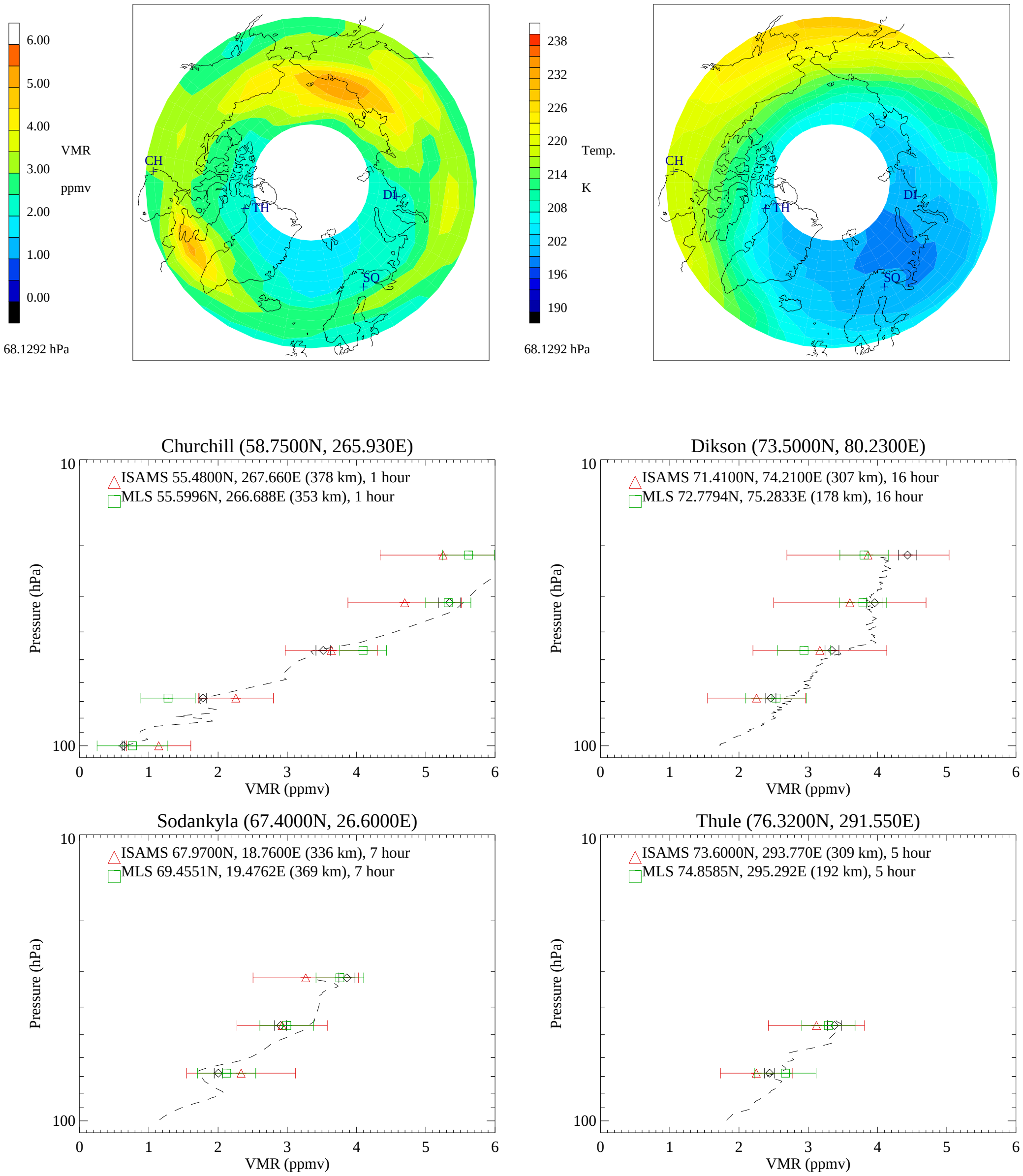

Figure 5.9: Comparison of co-located ISAMS, MLS and ozonesonde profiles on January 1 1992 at Churchill, Dikson, Sodankyla and Thule. The layout of the plots is the same as described in Figure 5.8.

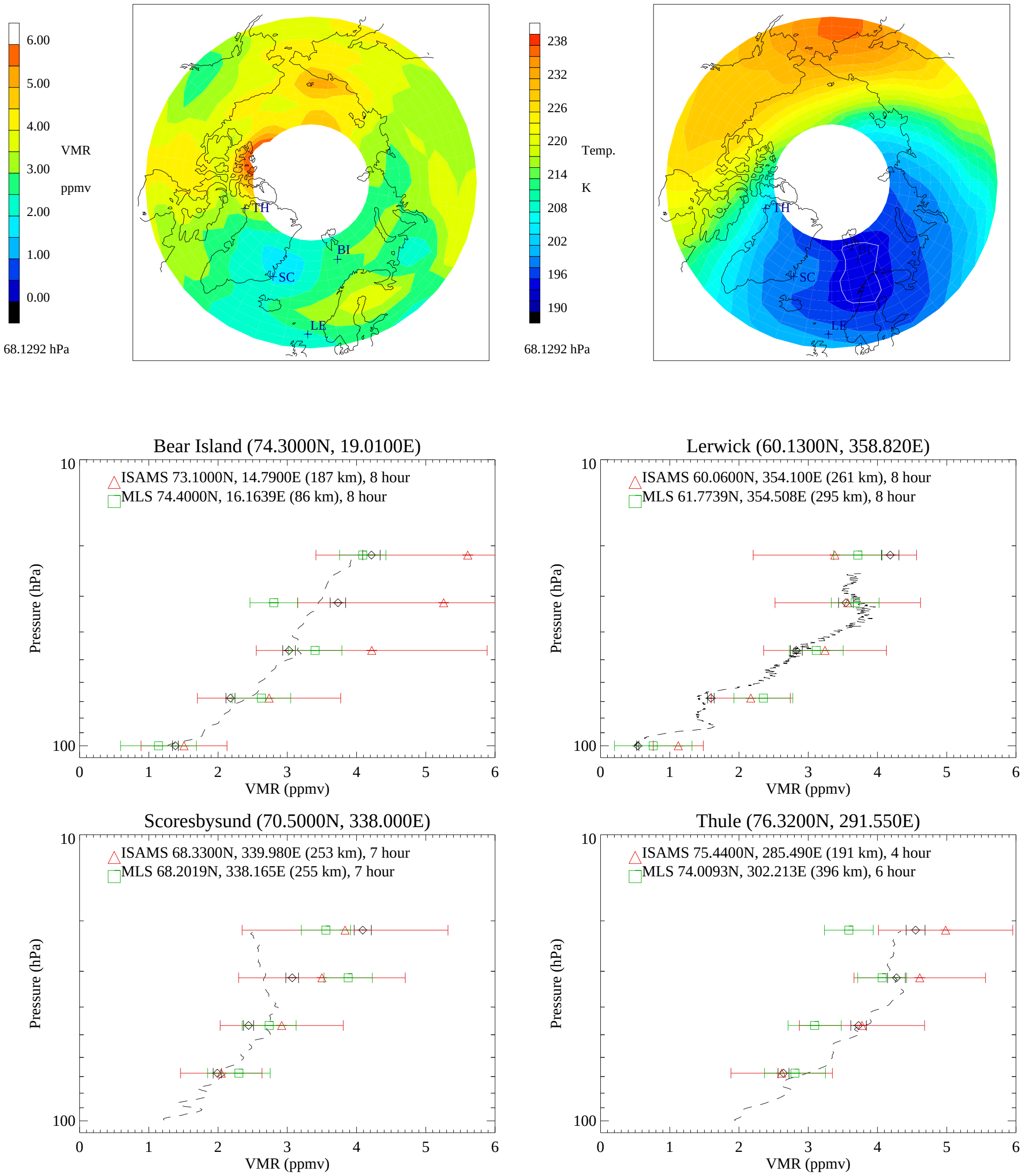

Figure 5.10: Comparison of co-located ISAMS, MLS and ozonesonde profiles on January 8 1992 at Bear Island, Lerwick, Scoresbysund and Thule. The layout of the plots is the same as described in Figures 5.8 and 5.9.

located profiles show similar agreements to the plots in Figure 5.8 although the time and distance differences are more varied (up to 369 km and 16 hours). Finally, the plots in Figure 5.10 show data at a slightly later stage in the winter period and there is now a region where the minimum temperature has fallen below the threshold temperature for PSC formation (indicated by the white contour line). In this case, the profiles outside this low temperature region (i.e. at Scoresbysund and Thule) show the best agreement at all surfaces although the profiles co-located to Bear Island and Lerwick, which are inside and close to the low temperature region respectively, show good agreement at the lower pressure surfaces and diverge higher up. The discrepancies in the profiles at Bear Island and Lerwick could also be explained by the relatively large time differences between the measurements (15 and 16 hours respectively).

Although the plots in Figures 5.8, 5.9, 5.10 appear to show that there is a reasonable agreement between the ISAMS, MLS and individual ozonesonde profiles over a range of geographical locations and with a range of time and distance differences between measurements, they are only representative of a relatively small selection of the data available during the 40 days of UARS data available during this winter period (there are a total of 116 ozonesonde profiles available from the stations shown in Table 5.1 during this time period). A more extensive comparison of the ISAMS, MLS and ozonesonde data is performed by plotting the scatter at different UARS pressure surfaces in the lowermost stratosphere: 100, 68, 46 and 32 hPa (UARS pressure surfaces 6, 7, 8 and 9 respectively). Figure 5.11 shows the scatter of ozonesonde versus the ISAMS data with different symbols representing different geographical distances (divided into 100 km bins between 0 and 400 km) between the ISAMS profiles and the latitude and longitude of each ozone sounding station. The different colours represent different time differences (in 5 hour bins from 0 to 15 hours) between the time of the ISAMS profiles and the time of launch of each ozonesonde. The dashed black line is the y equals x line. There appears to be a reasonable agreement between the ISAMS

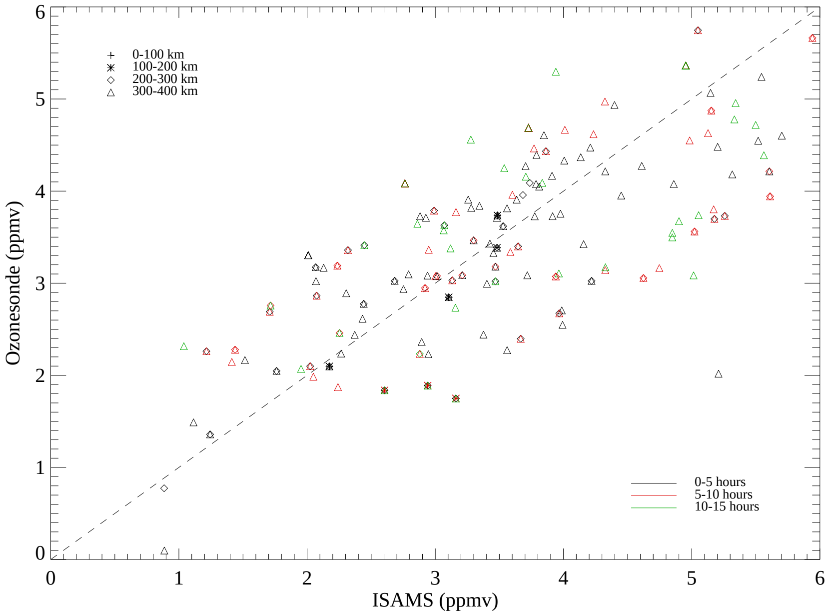

Figure 5.11: Ozonesonde versus co-located ISAMS ozone data in the low aerosol region on UARS pressure surfaces 6 to 9. Geographical distances of 0 to 100, 100 to 200, 200 to 300 and 300 to 400 km are represented by the +, *. diamond and triangle symbols respectively. Black, red and green represent time differences of 0 to 5, 5 to 10 and 10 to 15 hours respectively.

and ozonesonde data in the lower stratosphere, with the distribution of the scatter centred approximately on the y equals x line. Figure 5.12 shows the scatter of the ISAMS and ozonesonde data, geolocated to be within 200 km and 5 hours, binned according to UARS pressure surface with the black, red, green and blue data points representing UARS pressure surfaces 6, 7, 8 and 9 respectively. This shows more clearly than in Figure 5.11 the agreement between the ISAMS and ozonesonde data within relatively tight co-location criteria. Figures 5.13 and 5.14 show the scatter of the MLS v5 versus ozonesonde data, and the MLS v5 versus the ISAMS data respectively. The comparison of the UARS data to ozonesonde data presented here shows that the MLS v5 data fits the sonde data better than

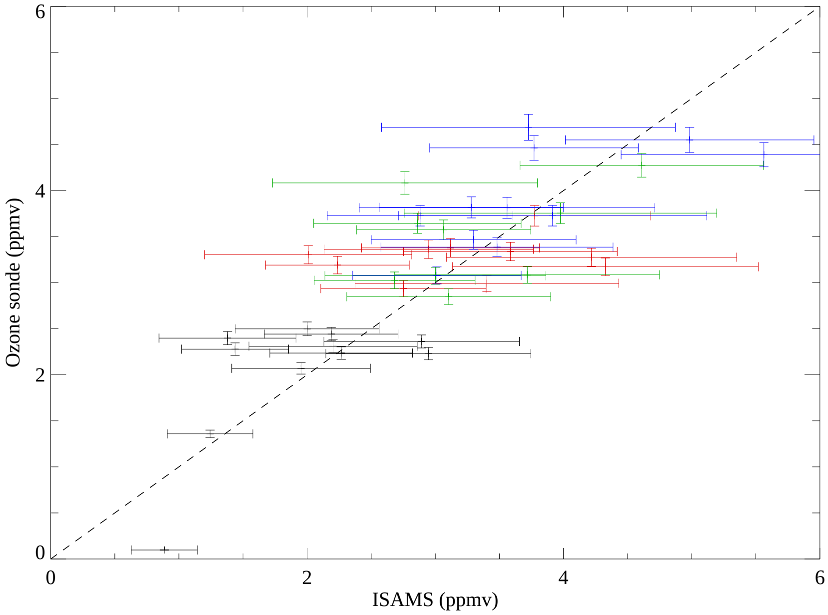

Figure 5.12: Ozonesonde versus co-located ISAMS ozone data, constrained to be within 200 km and 5 hours of each ozonesonde launched, on UARS pressure surfaces 6 to 9. The black, red, green and blue data points represent UARS pressure suarfaces 6, 7, 8 and 9 respectively. The vertical bars show the ±3% precision of the ozonesonde measurements and the horizontal bars show the $1\sigma$ errors on the ISAMS data.

ISAMS and especially on UARS pressure surfaces 7, 8 and 9. The ISAMS data shows similar features when compared to the ozonesonde and MLS v5 data. The scatter of the ISAMS data versus the other data is generally centred on the y equals x line although with considerably more variability than shown by MLS. Some of the variability in the plots showing all of the geolocated data is reduced when more restrictive constraints are imposed on the geolocation to the ozonesonde stations. However, the error bars on the ISAMS data are still large relative to the other data, expecially above pressure surface 6. One likely cause for the greater variability in the ISAMS data is temperature. The ISAMS retrieval is much more sensitive to temperature errors, and this is particularly the case in regions of low temperature (where $(1/B)(\partial B/\partial T)$ is largest) which is also where the ISAMS temperature retrieval will have the largest uncertainties. Table 5.2 shows how $(1/B)(\partial B/\partial T)$ changes as a function of temperature at infrared (10 $\mu$m) and mi-

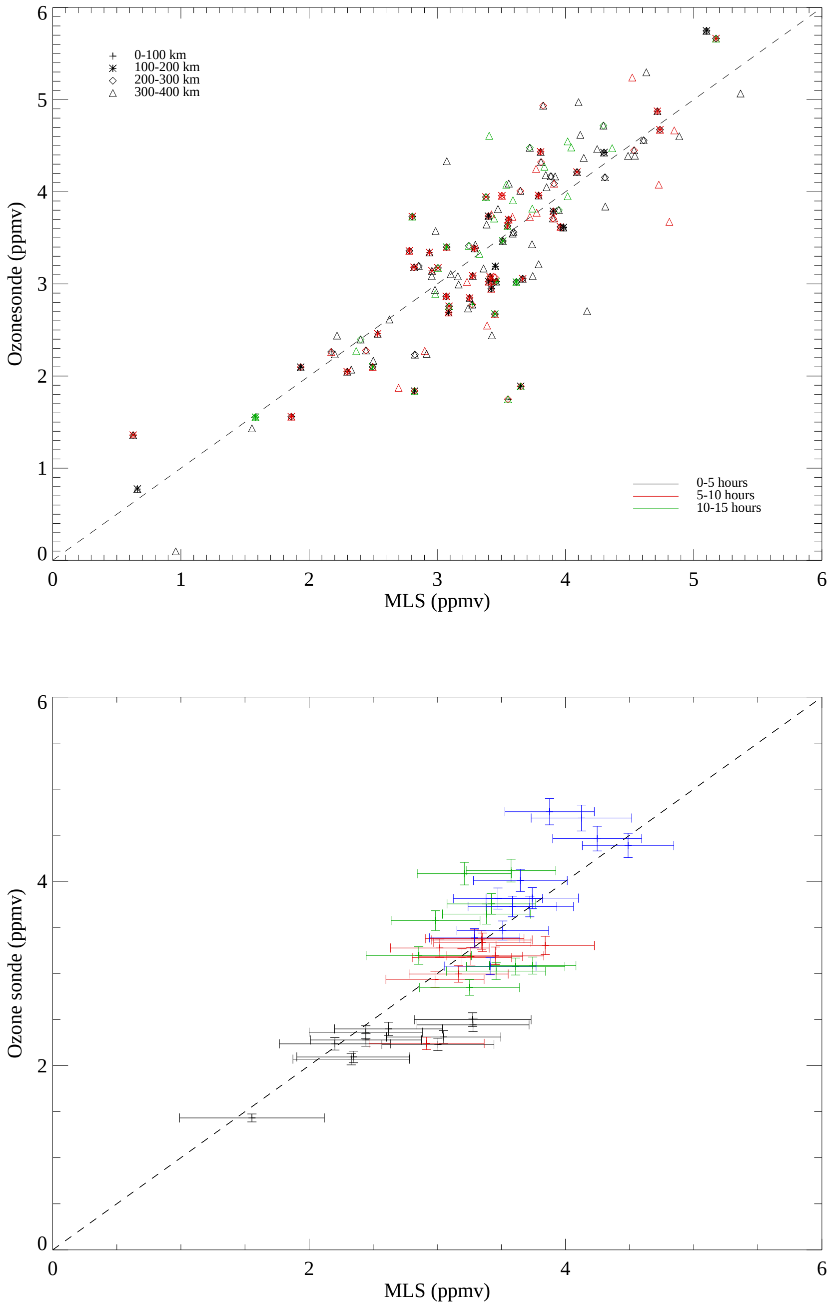

Figure 5.13: Ozonesonde versus co-located MLS v5 ozone data in the low aerosol region on UARS pressure surfaces 6 to 9. The upper plot shows the comparison of all the co-located data, and the lower plot shows the data co-located within 200 km and 5 hours of each other.

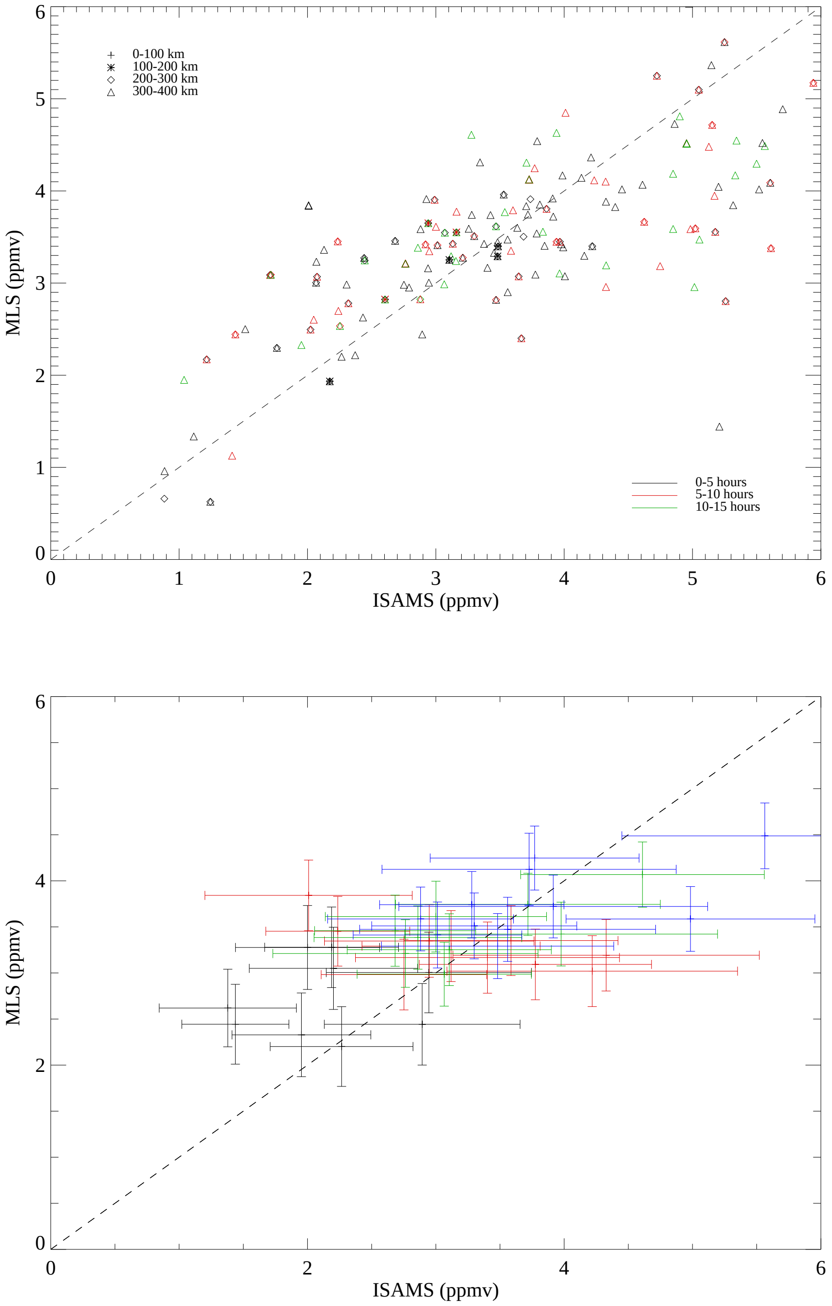

Figure 5.14: MLS v5 ozone data versus ISAMS ozone data in the low aerosol region on UARS pressure surfaces 6 to 9.

crowave (200 GHz $\equiv$ 1500 $\mu$m) wavelengths.

| Temperature (K) | 10 $\mu$m | 1500 $\mu$m |
|---|---|---|
| 180 | 0.0444 | 0.0057 |
| 190 | 0.0399 | 0.0054 |
| 200 | 0.0369 | 0.0051 |
| 210 | 0.0327 | 0.0049 |
| 220 | 0.0300 | 0.0046 |

Table 5.2: Evaluation of $(1/B)(\partial B/\partial T)$ as a function of temperature at infrared (10 $\mu$m) and microwave (1500 $\mu$m) wavelengths.

It is clear the the sensitivity at infrared wavelengths to $(1/B)(\partial B/\partial T)$ is considerably greater (by approximately a factor of 10) than at microwave wavelengths.

## 5.5 Discussion and Further Work

In this chapter, retrievals of ozone have been performed to cover the lowermost stratosphere, using a vector-vector optimal estimation approach to the ISAMS data measured during the 1991-92 Northern hemisphere winter. Sulphate aerosol from the eruption of Mt. Pinatubo did not enter into the Arctic polar vortex until after mid-January 1992. The time period of the ISAMS observations around the Arctic extends from December 6 1991 to January 13 1992. The effect of correcting for aerosol in the ozone retrieval is not significant above UARS pressure surface 8 (46 hPa) at high latitudes during this time (as shown in Figure 5.3). Correcting for aerosol in the retrieval is potentially more significant below this pressure surface. The ISAMS ozone retrievals have been compared to ozonesonde and MLS data, also available from the 1991-92 Arctic winter, with results showing reasonable agreement indicating that the ISAMS data contains information on ozone in the relatively aerosol free lower stratosphere. The level of agreement is dependent on the amount of aerosol present as the MLS measurement are relatively insensitive to the presence of PSCs. The ISAMS data shows more scatter than the MLS data implying that, for studies of ozone in polar winter, an infrared instrument with greater information content is required and with more accurate temperature retrievals. The temperature retrieval is important at low temperatures as the ISAMS data is more sensitive to temperature errors than the MLS, and at cold temperatures lead to a lower signal to noise ratio. The magnitude of the error bars on the ISAMS data could potentially be reduced if a more realistic *a priori* uncertainty is used in the retrieval. Although the comparison of the ISAMS ozone to the ozonesonde and MLS measurements appears to show reasonable agreement, there are a number of aspects that require further consideration and are discussed in the following sections.

### 5.5.1 Aerosol emissions in the infrared

One of the main criteria for retrieving ozone in the lower stratosphere from the ISAMS data has been the definition of a low aerosol region to avoid potential contamination of the measured radiance signal by sulphate aerosol from Mt. Pinatubo. The definition of the low aerosol region has been based on the ISAMS v12 12.1 $\mu$m aerosol extinction. However, as Taylor et al. (1994) showed, there were episodes of PSC activity during this winter period and the 12.1 $\mu$m aerosol extinction may not be sufficient for avoiding PSC emissions contaminating the radiance signal. Figure 5.15 shows radiance spectra calculated for stratospheric sulphate aerosol (SSA) and PSC aerosol (NAT and STS) across a spectral range that includes the ISAMS aerosol and ozone channels. The dominant signal is seen to come from SSA around both 12.1 and 9.6 $\mu$m indicating that the ISAMS v12 12.1 $\mu$m aerosol extinction is a suitable indicator for defining the low aerosol region in which to retrieve ozone.

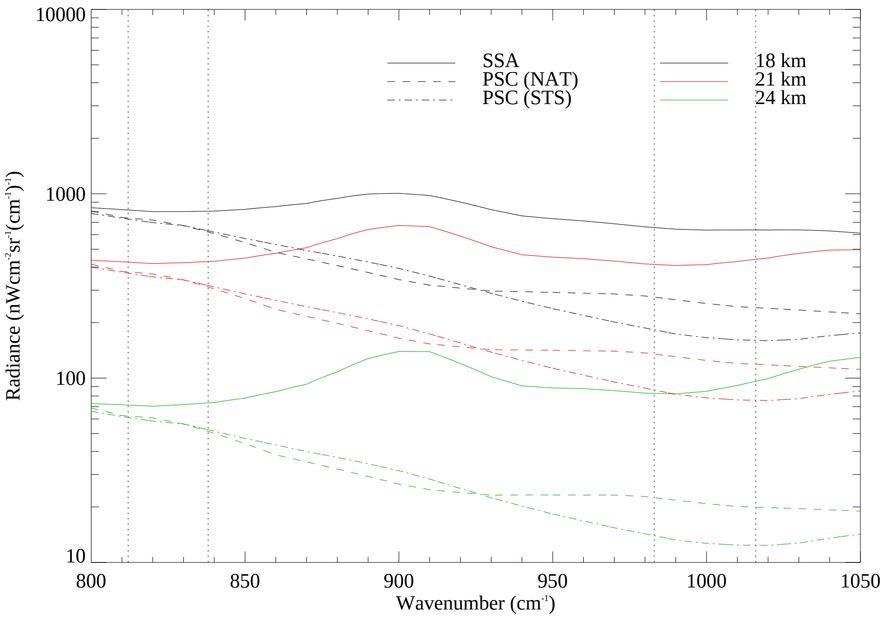

Figure 5.15: Radiance spectra calculated by the RFM for stratospheric sulphate aerosol (solid lines), NAT PSCs (dashed line) and STS PSCs (dot-dash line) for a spectral range from 800 to 1050 cm$^{-1}$ to cover the ISAMS aerosol (812 to 838 cm$^{-1}$) and ozone (983 to 1016 cm$^{-1}$) channels, indicated by the vertical dotted lines. The atmospheric profiles used in these calculations were for polar winter conditions. The black, red and green lines represent tangent altitudes of 18, 21 and 24 km respectively. Extinction and cross-section data for SSA provided by S. H. Marsh (personal communication).

### 5.5.2 Co-location errors

As described in section 5.4.3, UARS profiles are co-located to the latitude and longitude of each ozonesonde launch station used in the EASOE and AASE-II measurement campaigns, and the time of launch of each ozonesonde. Figure 5.11, and the upper plots in Figures 5.13 and 5.14 show the comparison of the different data sets co-located to be within 400 km and 15 hours of each ozonesonde station, and illustrate the variability of the data for different spatial and temporal constraints. Figure 5.12, and the lower plots in Figures 5.13 and 5.14 show the variability between the data sets if the constraints for the co-location are restricted to be within 200 km and 5 hours. In this case, the variability is much reduced and it can be argued that there is better agreement between the data, although the ISAMS data appears to slightly underestimate the amount of ozone. The MLS data shows better agreement with the sonde data and this could be due to radiance signal measured by the MLS instrument, and the MLS retrievals, being less sensitive to low temperatures compared to the ISAMS. There are other errors that are introduced to the comparison when the UARS and sonde profiles are co-located. Even if the UARS and ozonesonde profiles are exactly coincident, the ozonesonde measurement is only representative of a single point in the satellite field-of-view at each level. The signal measured by a satellite limb sounder is averaged over the volume of the FOV (the ISAMS field-of-view, projected onto the atmospheric limb, measured 2.36 km in the vertical by 16.6 km in the horizontal, with a line-of-sight distance of approximately 3000 km), and this provides a source of uncertainty before any spatial seperation between sonde and satellite measurements (McNally, 1990). The minimum error is determined by the horizontal variability of the atmosphere on the scale of the spatial seperation (Bruce, 1977). It is also important to remember that the radiance observed at the satellite is over a long line-of-sight path length through the atmosphere and an ozonesonde only samples the air it passes through as it ascends. There will be similar errors due to temporal separations between sonde and satellite measurements, which will be dependent on the variability of the atmosphere over the time scale. The error due to co-location of sonde and satellite profiles is reduced by tightening the co-location criteria but this also reduces the size of the data samples to be compared, which will reduce the representative nature of the statistics (McNally, 1990).

### 5.5.3 Line-of-sight gradients

One of the approximations made by the ISAMS retrievals is in the treatment of horizontal gradients along the instrument line-of-sight (Rodgers et al., 1996). Horizontal gradients in the distribution of temperature, pressure and absorber amount complicates the radiative transfer calculation especially as gradients in temperature and pressure affect the curvature of a ray path from the tangent point to the instrument (Marks and Rodgers, 1993). There are several approximations that can be applied for handling such gradients in a retrieval and are described in section 9.5.3 of Rodgers (2000). In the ISAMS retrievals, horizontal gradients are accounted for with a two-stage procedure which firstly sets the gradients to zero and the resulting retrieved profiles gridded so that simple central difference estimates can be made at each profile location. These are then used to produce a revised set of retrievals (Marks and Rodgers, 1993). In the MLS retrievals, microwave radiance emissions depends approximately linearly on temperature and errors from line-of-sight gradients are ignored (Fishbein et al., 1996), although this approximation is particularly poor in winter at high latitudes when there are periods of large wave activity and strong horizontal gradients (Froidevaux et al., 1997). The impact of horizontal gradients on radiative transfer calculations, and the potential for more accurate representation of such gradients in a retrieval scheme, are discussed in more detail in the following chapters.

### 5.5.4 Further work

To assess the amount of information that is actually available in the ISAMS data on ozone in the lower stratosphere, it would also be useful to calculate the information content over the lowermost stratosphere. Other useful considerations would be to compare the data to that recorded in subsequent years, which is only possible for the MLS data in the context of this study. Also, a comparison of the retrievals to those made at mid-latitudes would be useful, but again is not possible with the ISAMS data due to aerosol from the Mt. Pinatubo eruption. The ozonesonde profiles were smoothed with the ISAMS averaging kernels as described although for consistency in the comparison of MLS v5 ozone to the ozonesondes, the ozonesonde profiles should be smoothed with the MLS averaging kernels.

# Chapter 6

# Radiative Transfer Modelling for MIPAS

## 6.1 Introduction

The forward model is one of the most important components of a retrieval scheme as it provides a description of all of the physics in the measurement, which is required to relate the measured signal to the actual state of the atmosphere.

A 1-dimensional (1-D) representation of the state of the atmosphere often assumes spherical (horizontal) symmetry in the atmospheric parameters (i.e. temperature, pressure, trace gas concentration, etc.). This approximation can be unrealistic, especially in the case of a limb sounding geometry, where the tangent path of the instrument line-of-sight extends over several thousand kilometres. Assuming a horizontally symmetrical atmospheric state limits the quality of a retrieval in the following ways:

- Information on atmospheric horizontal structure along the instrument line-of-sight is not taken into consideration.

- The representation of the atmosphere may not be realistic enough to characterise the measurements, which will lead to significant forward model error propagating into the retrieval error (Siddans et al., 2000a).

To overcome these problems it is necessary to model the full horizontal structure of the atmosphere within the plane of the instrument line-of-sight, which requires a full 2-dimensional (2-D) treatment of the radiative transfer.

In this chapter, two forward models with the capability for modelling radiative transfer rigorously in 2-D as well as spherically symmetric approximation are considered:

- a 2-D thermal line-by-line radiative transfer model (referred to as the FM2D), developed at the Rutherford Appleton Laboratory under an ESA contract for the assessment of millimetre-wave atmospheric limb sounding (Siddans et al., 2000b).

- the MIPAS Reference Forward Model (RFM), which is also a line-by-line radiative transfer model, based on GENLN2, developed at Atmospheric, Oceanic and Planetary Physics, Oxford University under an ESA contract to provide reference spectral calculations for the MIPAS instrument (Dudhia, 1996).

## 6.2 Forward Model Physics

As described above, the main purpose of a forward model is the integration of the radiative transfer equation. In this chapter the mechanisms and approximations made in the integration of equation (2.12) by the FM2D and the RFM are described in more detail.

In general, the calculation of radiance spectra by a forward model is performed by dividing the atmosphere into several layers and defining the path followed by the radiation through the atmosphere (ray tracing). Atmospheric state parameters along the path (i.e. pressure, temperature and mixing ratios of an arbitrary number of gases and continuum parameters) are specified at the layer boundaries. Absorption coefficients and, hence, the transmittance for each layer are evaluated at a set of quadrature points, which in turn are used to calculate the radiance which would be observed at the satellite.

### 6.2.1 Definition of the atmospheric state

In the FM2D, atmospheric states in 1-D and 2-D may be defined as $S(z)$ and $S(a, z)$ respectively, where $S$ is the atmospheric state parameter (see above), $z$ is altitude, and $a$ is the distance along the line-of-sight away from the satellite nadir point along the line defined by the intersection of the plane containing the limb line-of-sights and the Earth's surface. In 1-D, $S(z)$ is defined for all $a$. Index arrays are used for the rapid linear interpolation of 1-D state parameters. In 2-D, a semi-regular grid (i.e. a rectangular grid such that for all $y$-coordinates, the grid is defined at the same set of $x$-coordinates and vice-versa, however the $x$ and/or $y$ values so defined need not be regularly spaced) is constructed by defining axes in $a$ and $z$ which contain all points on which the given state parameter has been defined. The parameters at the retrieval points are interpolated onto the semi-regular grid by triangulation of the retrieval points, followed by triangular interpolation. In this way an irregularly spaced field is converted into a semi-regular field which, by constructing index arrays for each dimension, can be repeatedly interpolated relatively rapidly.

In the RFM, atmospheric layer boundaries are chosen in such a way that the gas within the layer may be considered to be well represented by the Curtis-Godson absorber weighted mean parameters for temperature and pressure (the Curtis-Godson approximation allows the pressure, temperature and absorber amount to be calculated for a uniform path which is equivalent to a non-uniform path when the absorption is Lorentzian or weak, see section 6.2.2).

### 6.2.2 Ray tracing and refraction

In the FM2D, for a given viewing geometry, atmospheric state parameters are defined at a number of arbitrary points along the line-of-sight, together with the associated line-of-sight distances from the start of the path. The points at which the state parameters are defined defines the quadrature points used in the integration of the radiative transfer equation. The quadrature grid points are defined to include:

1. all of the intersections of the ray path with the vertical levels defined for the atmosphere.
2. the tangent point or the surface.
3. all of the intersections of the path with the semi-regular grid defined for the refractive index field (i.e. the intersections with the vertical and horizontal lines which make up the grid (see Figure 6.1)).

The state parameters are interpolated onto this quadrature grid using the rapid linear interpolation scheme mentioned above. Figure 6.1 shows the limb viewing geometry defined for the FM2D.

In the RFM, when the layer structure of the atmosphere has been determined, a path is defined for each gas within the layer. The ray paths through the layer are determined by the layer boundary altitudes and the local zenith angle at the lower boundary (which is calculated for each layer using Snell's law, equation (6.4)).

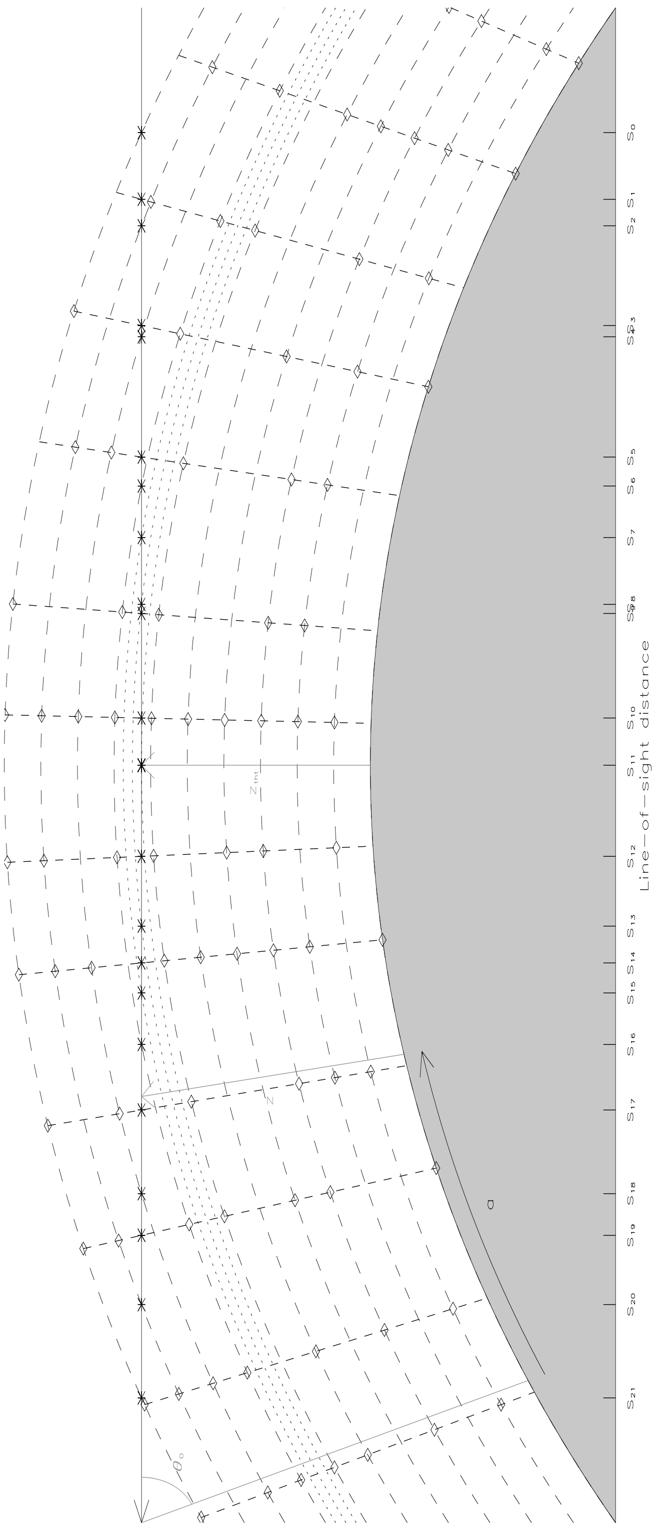

Figure 6.1: Limb viewing geometry for FM2D. The diamonds indicate the points where the 2-D field is defined, with the dashed lines showing the semi-regular grid. The dotted lines indicate the user-defined vertical grid, and the asterisks show the derived quadrature grid used for the integration of the radiative transfer equation (Siddans et al., 2000b).

When the ray paths are fully defined, the Curtis-Godson absorber weighted mean values are calculated for each path $l$ (Note:- each layer is sub-divided into layers to calculate the path through the layer). The integrated absorber amount ($u_l$), pressure ($p_l$) and temperature ($T_l$) for the ray path $s$ between vertical limits, $z_1$ and $z_2$, are calculated:

$$u_l = \int_{z_1}^{z_2} \left( \rho_a(z)_i \frac{ds}{dz} \right) dz \tag{6.1}$$

$$p_l = \frac{1}{u_i} \int_{z_1}^{z_2} p(z) \left( \rho_a(z)_i \frac{ds}{dz} \right) dz \tag{6.2}$$

$$T_l = \frac{1}{u_i} \int_{z_1}^{z_2} T(z) \left( \rho_a(z)_i \frac{ds}{dz} \right) dz \tag{6.3}$$

where, $\rho_a(z)_i$ is the local number density of gas $i$.

It is important to note that equations (6.1), (6.2) and (6.3) are for an atmosphere defined in 1-D. If the RFM radiance calculation is to be performed for an atmosphere defined in 2-D, the ray tracing utilises radial, as opposed to Cartesian coordinates (see section 9.4 of Rodgers (2000)).

The atmosphere is a refractive medium, and therefore it is important to take this into account when calculating radiative transfer in limb emission. Refraction in the atmosphere affects radiative transfer for limb emission in the following ways:

- the tangent point of a given line-of-sight is lowered
- the point at which the tangent point is reached is displaced away from the satellite nadir
- the distance travelled along the line-of-sight through an atmospheric layer is increased, which in turn increases the line-of-sight opacity to a given tangent point

In 1-D, Snell's law is conserved along the ray path in both the FM2D and the RFM:

$$C = n(r)r\sin\theta \tag{6.4}$$

where, $C$ is a constant along the ray path, $n(r)$ is the refractive index at the Earth's radius of curvature $r$ and $\theta$ is the local zenith angle.

In 2-D, refractive index contours need not be spherically symmetric, potentially complicating the system. A full ray tracing scheme, that computes limb-path loci to a high level of accuracy, taking fully into account the 2-D structure of the refractive index field, is computationally expensive and time consuming. An alternative ray tracing scheme, that assumes the refractive index field is spherically symmetric about the profile situated at the geometric tangent point (i.e. using equation (6.4)), is faster than the full ray tracing scheme and, for simulation purposes, does not lead to significant errors in the ray tracing (Siddans et al., 2000a). This second approach is the one utilised in the FM2D simulated radiance calculations presented in this and subsequent chapters. In the RFM, each path is defined by the zenith angle at the lower layer boundary, the zenith angle at the upper boundary and the path length within the layer with the refractive index defined at each boundary.

### 6.2.3 RTE integration

As shown in chapter 2, the measured radiation intensity from limb thermal emission is given in integral form by the radiative transfer equation (equation (2.12)). The numerical integration of the radiative transfer equation is discussed in this section with a comparison of the particular aspects of the FM2D and RFM radiative transfer calculations. The numerical calculation of the integration of the radiative transfer equation can be performed as:

$$I(\nu, L) = \sum_{l=1}^{N} B_l(\nu, T_l)(1 - \tau_l(\nu)) \prod_{k=l+1}^{N} \tau_l(\nu) \tag{6.5}$$

where $L$ is the total length of the radiation path, $N$ is the total number of path segments $l$. $B_l(\nu, T_l)$ and $\tau_l(\nu)$ are the Planck function and transmittance at path segment $l$. From equation (2.5) the transmittance can be calculated as:

$$\tau_l(\nu) = \exp(-\alpha_l(\nu)\rho_a(l)\Delta_l) \tag{6.6}$$

where $\Delta_l$ is the thickness of path segment $l$ and $\alpha_l(\nu)$ is the absorption coefficient at each path segment and is calculated using equations (2.6) and (2.7).

### Absorption coefficients

In the FM2D, absorption coefficients are calculated through the following steps:

- Temperature and pressure conversion of the line data supplied from a spectral line database (referenced to standard temperature and pressure).

- Evaluation of the Voigt spectral line-shape function accounting for Doppler and pressure broadening, for each line at all monochromatic grid points.

- Evaluation of continua (i.e. $N_2$, $O_2$ and $H_2O$), if required, according to the Clough et al. (1989) model.

- The contributions from all $N_{\text{abs}}$ lines for each of $N_{\text{abs}}$ gaseous constituents (plus continuum) are summed to obtain volume absorption coefficients:

$$k(\nu) = k_{\text{cont}}(\nu) + \sum_{i=1}^{N_{\text{abs}}} \sum_{j=1}^{N_{\text{lin}}} \alpha_{ij}(\nu)\rho_i(z) \tag{6.7}$$

where, $k_{\text{cont}}(\nu)$ is the continuum absorption coefficient, $\alpha_{ij}(\nu)$ is the monochromatic absorption coefficient of absorber $i$ and spectral line $j$ and $\rho_i(z)$ is the absorber density at altitude $z$.

The RFM employs a line-by-line calculation to calculate transmittance over the given spectral range for each absorber in several atmospheric layers. The monochromatic absorption of each line $i$ in the spectral range of path gas $j$ is calculated at each grid point over the entire spectral range is given by equation (2.6).

To reduce computation time, the absorption is calculated with a wide wavenumber grid employed in the wings of each line in the spectral range and a fine wavenumber grid used at each line centre, where the line profile is rapidly changing. Also, the calculation is only performed for lines of significant strength. The contribution of the far line wings and of lines that lie outside the given spectral range is important and also taken into consideration. All these various components are calculated at the fine wavenumber grid points for a path $j$, and the total monochromatic absorption coefficient is formed:

$$k(\nu)_j = k(\nu)_j^a + k(\nu)_j^b + k(\nu)_j^c \tag{6.8}$$

where, $k(\nu)_j^a$ is the contribution from the line wings, $k(\nu)_j^b$ is the contribution from the near lines and $k(\nu)_j^c$ is the broadband contribution which includes the gaseous continuum, molecular cross-section and aerosol contributions (see the RFM technical report (Dudhia, 1996) for a full description).

Line shape information for the results presented in this chapter is provided by the HITRAN96 database (Rothman et al., 1998).

### Radiance calculation

In the FM2D radiance calculation, for a given line-of-sight, the volume absorption coefficients $k_l$ are defined at a set of along line-of-sight distances $s_l$, and the transmittance of each path segment, between each of the along line-of-sight distances is calculated as follows:

$$\tau_l = \exp\left[\frac{1}{2}(k_l + k_{l+1})(s_{l+1} - s_l)\right] \tag{6.9}$$

The observed radiance is then calculated as the summation over all path segments as shown in equation (6.5).

In the RFM radiance calculation, the total optical depth $\chi_l(\nu)$ of each layer $l$, assuming that each layer is made up of $N_{\mathrm{path}}$ single gas paths, is[1]:

$$\chi_l(\nu) = \sum_{m=1}^{N_{\mathrm{path}}} k_m(\nu) u_m \tag{6.10}$$

$k_m(\nu)$ and $u_m$ are calculated using equations (6.8) and (6.1) respectively. The radiance is calculated layer by layer along the ray path through the atmosphere using equation (6.5).

## 6.2.4 Weighting functions

As shown in chapter 4, the ability to retrieve geophysical parameters requires computation of a weighting function matrix (e.g. equation (4.2)) which represents the sensitivity of the measurements (or radiance calculation in this case) to a change in the state vector.

---

[1] The optical path length is used to calculate the transmittance: $\tau_l(\nu) = \exp(-\chi_l(\nu))$

In the FM2D, derivatives of the absorption coefficient (i.e. equation (6.7) with respect to absorber amount, temperature and pressure are evaluated directly by evaluating explicit derivatives of the relevant equations (Siddans et al., 2000b)). After the equation of radiative transfer has been integrated, weighting functions of the radiance with respect to atmospheric state parameters are obtained by differentiating equation (6.5) with respect to the absorption coefficient, and Planck function, at each segment boundary. Once these derivatives have been evaluated, derivatives with respect to the atmospheric state parameters (defined at the LOS quadrature points) are obtained by using the already determined derivatives of the absorption coefficients with respect to the state parameters. Full details on the computation of weighting function matrices with the FM2D are given by Siddans et al. (2000b).

In the RFM, Jacobian spectra are calculated by perturbing the state vector at each tangent altitude and performing the radiance calculation over all tangent altitudes for each perturbation. Each row of the weighting function matrix is then the Jacobian corresponding to that tangent altitude (Jay, 2000).

### 6.2.5 Instrument effects

The MIPAS instrument is an interferometer with finite spectral resolution and a finite field of view (FOV) at the atmospheric limb, whereas the radiance calculation described above is essentially at the monochromatic fine grid resolution (typically 0.0005 $\mathrm{cm}^{-1}$) for an infinitesimally small instrument FOV (i.e. pencil-beam). To calculate radiance spectra at the instrument spectral resolution, the infinite resolution calculations must be convolved with the instrument spectral response, or Instrument Line Shape (ILS). To incorporate the MIPAS FOV, convolution is also necessary over a set of pencil-beam views.

In the FM2D, monochromatic pencil-beam radiances are convolved with the defined ILS and FOV functions by determining weights for each monochromatic grid based on the provided scan pattern, FOV function and ILS function. Matrix multiplication is then used to obtain the convolved radiances.

In the RFM, the FOV convolution is performed by calculating the intensities on each grid point of the provided FOV function. The ILS convolution is performed by interpolating the provided ILS function onto a regularly spaced fine-mesh (with a typical width of 0.0005 cm$^{-1}$).

### 6.2.6 Atmospheric profiles

Reference atmospheric profiles for the MIPAS RFM are provided for five different atmospheric scenarios: mid-latitude day and night, polar summer and winter, and tropical (daytime only). Figure 6.2 shows the reference mid-latitude day profiles of ozone, temperature and pressure which are used for the radiance calculations in section 6.3.

## 6.3 Numerical Comparison of Forward Models

### 6.3.1 Methodology

To quantify the differences between the two forward models, ozone radiance spectra (i.e. radiance for an ozone only atmosphere) are calculated with each model at tangent altitudes of 10, 20, 30, 40 and 50 km, as observed from a satellite altitude of 820 km. Radiance spectra are calculated for an arbitrarily chosen spectral range of 1073.800 to 1076.800 cm$^{-1}$ at 0.025 $^{-1}$ spectral resolution (corresponding to a microwindow selected for the operational retrieval of ozone for MIPAS).

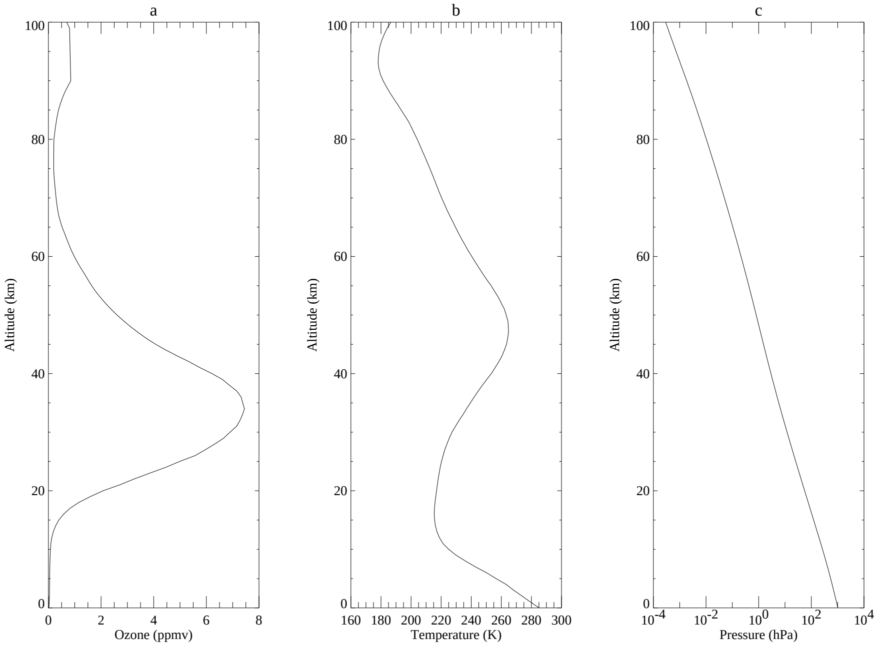

Figure 6.2: MIPAS reference mid-latitude daytime profiles for (a) ozone (ppmv), (b) temperature (K), and (c) pressure(hPa).

Reference atmospheric profiles of temperature, pressure and ozone which define the atmosphere in the forward models are typical of a mid-latitude (i.e. 45° latitude) daytime atmosphere between 0 to 100 km at intervals of 1 km (Figure 6.2). The atmospheric profiles are provided as reference profiles for MIPAS retrievals as described above.

Three different atmospheric scenarios are defined for each spectral calculation in the forward model comparison:

- 1-D - the atmospheric profiles are defined at the tangent point.
- 2-D flat field - the atmospheric profiles are defined at six distances along the satellite track from the instrument (1500, 2000, 2500, 3000, 3500 and 4000 km) to create a 2-D homogeneous atmosphere.

- 2-D field with horizontal gradients along the line-of-sight - a 2-D atmosphere is defined on the same along-track grid as for the 2-D flat field but multiplied by some scaling factor which increases the profile as the along-track distance increases (Note: the scaling factor is applied in such a way that the reference profile is the one at approximately the tangent point which is assumed taken to be approximately 3000 km).

Figure 6.3 shows the 2-D atmospheric fields with and without line-of-sight gradients for ozone, temperature and pressure.

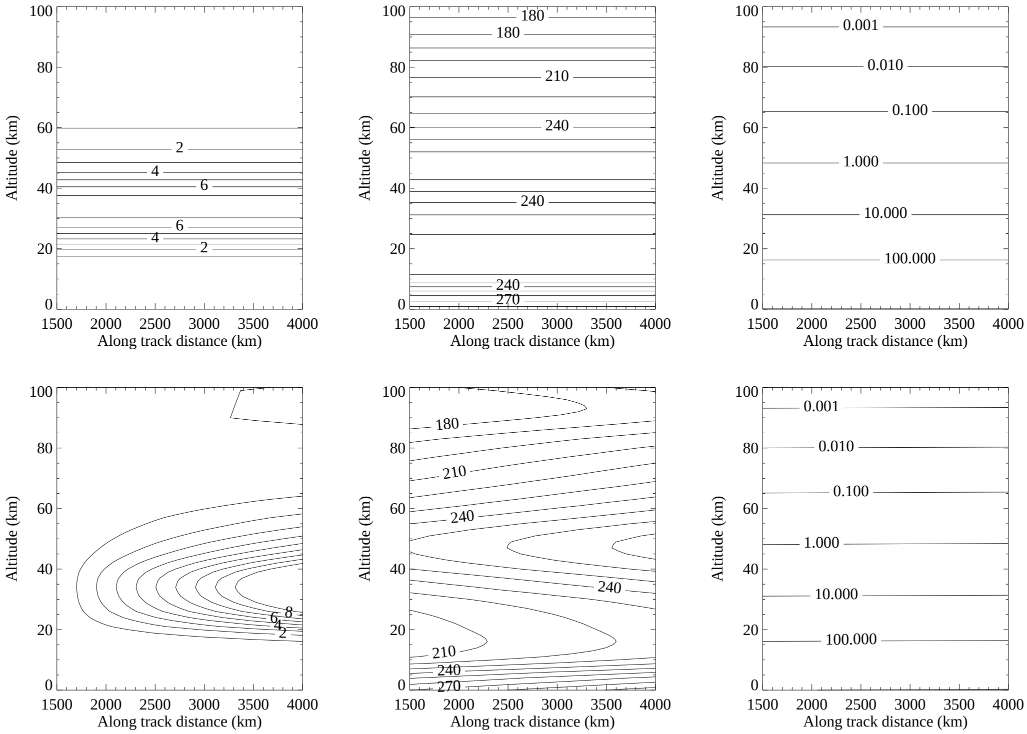

Figure 6.3: 2-D atmospheric fields used for the numerical comparison of the FM2D and RFM radiative transfer models. The upper row shows the homogeneous 2-D fields with the lower row showing the inhomogeneous 2-D fields for, from left to right, ozone (ppmv), temperature (K) and pressure (hPa).

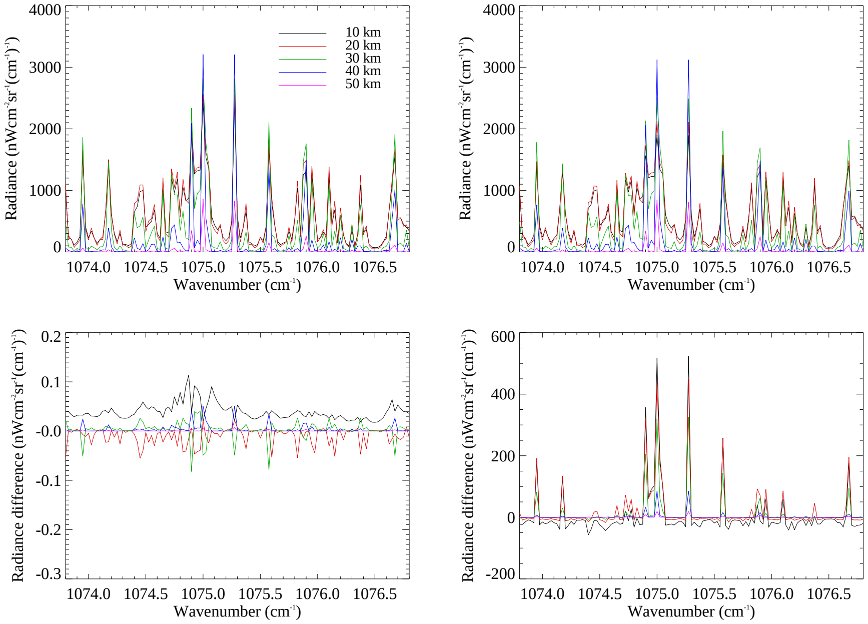

Figure 6.4: Radiance spectra, and differences, calculated by the FM2D in 1-D and 2-D for an ozone microwindow between 1073 and 1076 $\mathrm{cm}^{-1}$. The plots in the upper row show the radiance spectra calculated for 1-D vertical profiles (left-hand side) and the 2-D inhomogeneous field (right-hand side). The plots in the lower row show the differences between the 1-D and homogeneous 2-D (left-hand side) and the homogeneous and inhomogeneous 2-D fields (right-hand side). In all plots, the black, red, green, blue and pink lines show the radiance for tangent altitudes of 10, 20, 30, 40 and 50 km.

## 6.3.2 FM2D

Figure 6.4 shows the radiance spectra, and differences, for each of the defined atmospheric scenarios calculated with the FM2D in a spectral region between 1073.8 and 1076.8 $\mathrm{cm}^{-1}$. The radiance spectra show that the emissions in this spectral region due to ozone have strong features in the stratosphere at approximately 1075.0 and 1075.3 $\mathrm{cm}^{-1}$. In addition, there are signals from lower in the atmosphere with emission lines at approximately 1074.0, 1074.2 and 1076.7 $\mathrm{cm}^{-1}$. The difference plots in the lower row of Figure 6.4 show that there is negligible difference between the radiance calculated in 1-D and the homogeneous 2-D field, with the largest differences observed at a tangent altitude of 10 km of up to 0.1 $\mathrm{nW\,cm^{-2}\,sr^{-1}\,(cm^{-1})^{-1}}$ (approximately 0.003%). The difference between radiances calculated for the 2-D fields with and without horizontal gradient are more significant (between 10% and 16%) with the largest differences at the lowest tangent altitudes (10, 20 and 30 km) and at the centres of the strongest emission lines.

### 6.3.3 RFM

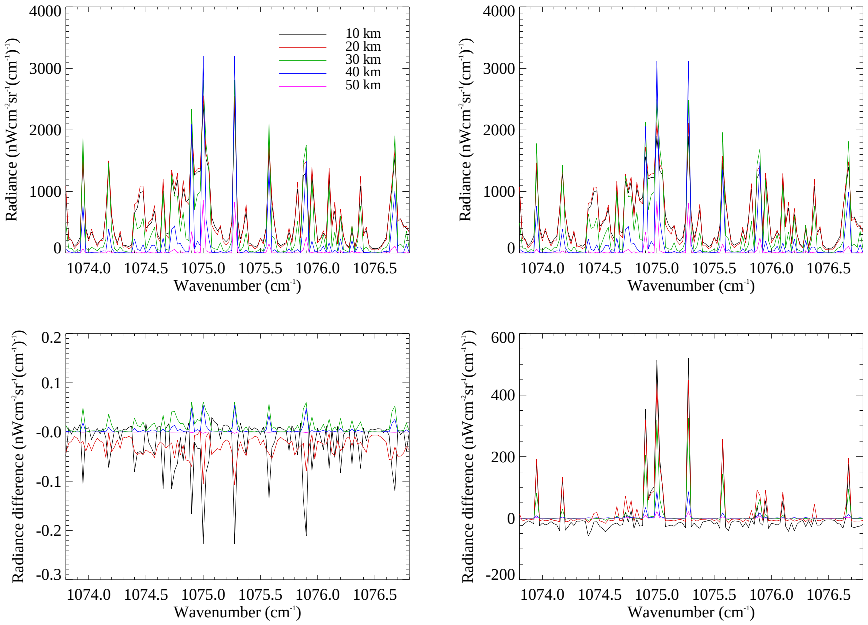

Figure 6.5: Radiance spectra, and differences, calculated by the RFM in 1-D and 2-D for an ozone microwindow between 1073 and 1076 $\mathrm{cm}^{-1}$. The plots are arranged as described for Figure 6.4.

Figure 6.5 shows the radiance spectra, and differences, for each of the defined atmospheric scenarios calculated with the RFM. The radiance spectra show the same emission features as shown for the FM2D calculations. The differences between the 1-D and homogeneous 2-D radiance calculations differ from those shown for the FM2D with differences of up to 0.25 $\mathrm{nW\,cm^{-2}\,sr^{-1}\,(cm^{-1})^{-1}}$ at a tangent altitude of 10 km and 0.1 $\mathrm{nW\,cm^{-2}\,sr^{-1}\,(cm^{-1})^{-1}}$ at a tangent altitude of 20 km. These differences are still negligible compared to the actual calculated radiance spectra (less than 0.01%). The differences between the homogeneous and inhomogeneous 2-D fields are similar to the FM2D differences, with the largest differences (between 10% and 16%) at the lowest tangent altitudes and at the line-centres.

### 6.3.4 FM2D vs RFM

Figure 6.6 shows the differences between radiance spectra calculated with the RFM and FM2D for each of the defined atmospheric scenarios. For the 1-D and homogeneous 2-D calculations, the largest differences are up to -4 nW $\mathrm{cm}^{-2}\,\mathrm{sr}^{-1}\,(\mathrm{cm}^{-1})^{-1}$ and appear to be at a tangent altitude of 30 km. This difference, although larger than the differences between the 1-D and homogeneous 2-D calculations for each forward model, are still less than 0.1%. The differences between the inhomogeneous 2-D calculations show more variability than the other differences although the order of magnitude in the differences is still the same (less than 0.1%). In this case, the largest differences are positive for lowest tangent altitudes (10 and 20 km) and negative for the highest tangent altitudes (40 and 50 km) although there are some negative differences at 20 and 30 km at the line-centres.

Figure 6.7 shows the difference between the lowest two plots in Figure 6.6 to indicate the differences between the FM2D and RFM due only to the horizontal gradient. The largest differences again appear to be at the line-centres, with positive differences up to 3 nW $\mathrm{cm}^{-2}\,\mathrm{sr}^{-1}\,(\mathrm{cm}^{-1})^{-1}$ at the lowest tangent altitudes and negative differences up to -2 nW $\mathrm{cm}^{-2}\,\mathrm{sr}^{-1}\,(\mathrm{cm}^{-1})^{-1}$ at the highest altitudes.

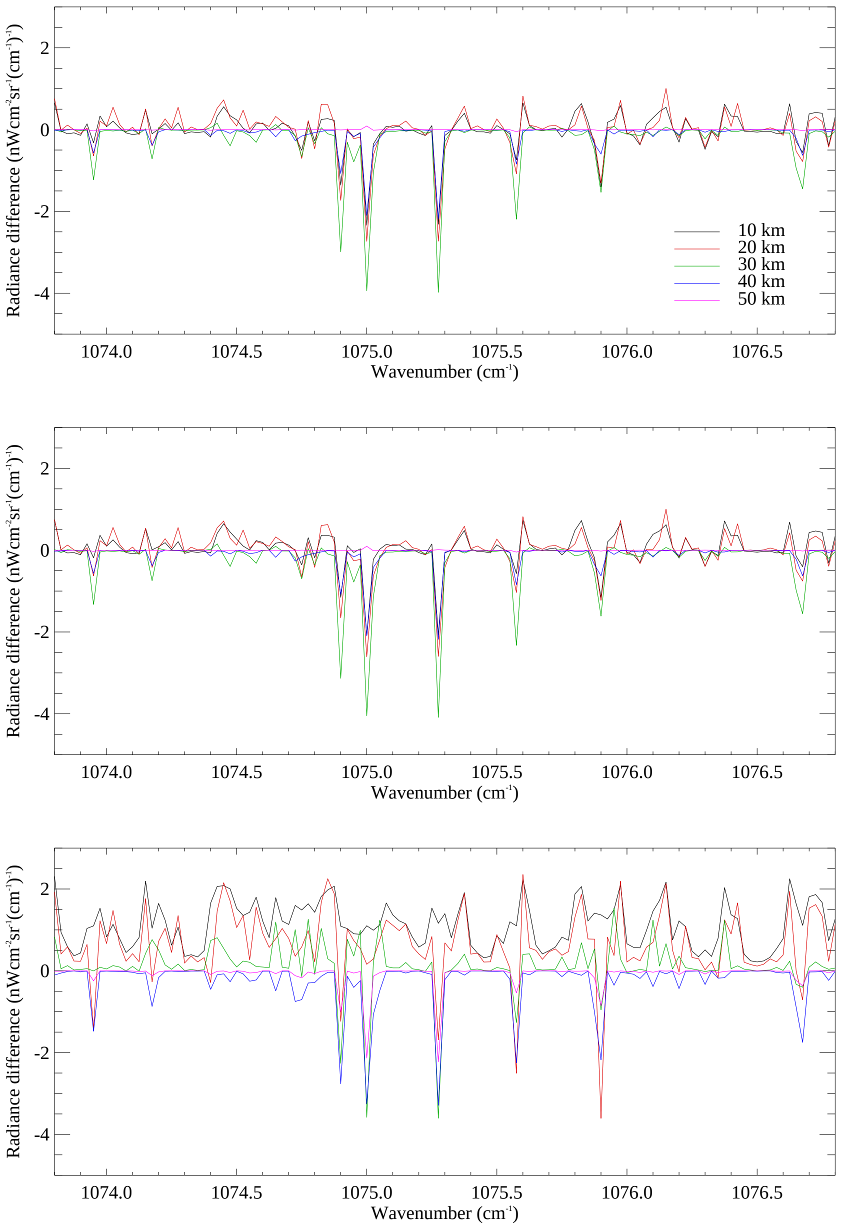

Figure 6.6: Differences in radiance spectra calculated by the RFM and the FM2D for an ozone microwindow between 1073 and 1076 cm$^{-1}$. From top to bottom the plots show the differences for the 1-D, homogeneous 2-D and inhomogeneous 2-D radiance calculations respectively. In each plot the black, red, green, blue and pink lines show the radiance calculated at 10, 20, 30, 40 and 50 km tangent altitudes.

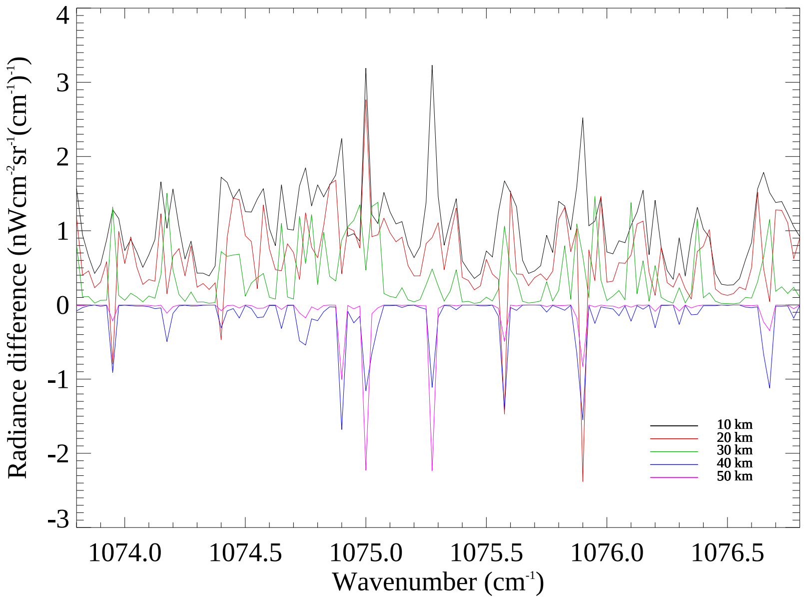

Figure 6.7: Difference between the radiances calculated with the RFM and FM2D shown for the homogeneous and inhomogeneous 2-D fields in Figure 6.6.

## 6.4 Summary

This chapter has presented the qualitative and quantitative differences in 1-D and 2-D radiative transfer calculations by two forward models: the FM2D and the RFM. The FM2D is the forward model which will be used to perform the simulated retrieval studies in the subsequent chapters of this thesis, and comparison of radiance calculations to the RFM provide a useful validation exercise. In addition, the aim of this chapter has been to illustrate:

- the differences in radiance spectra calculated by the two different models.
- the impact of horizontal gradients along the instrument line-of-sight on the accuracy of the calculation of radiance spectra by each model.

The physical principles employed by the two forward models in the integration of the equation of radiative transfer are largely the same with the main exception being the use of the Curtis-Godson approximation in the RFM.

Radiance spectra calculated for an idealised atmosphere containing only ozone have been calculated with both models for three different atmospheric scenarios based on a typical mid-latitude daytime atmosphere: 1-D, homogeneous 2-D and inhomogeneous 2-D. These radiance spectra are calculated in a spectral range from 1073.8 to 1076.8 cm$^{-1}$ and at tangent altitudes of 10, 20, 30, 40 and 50 km with the results shown in Figures 6.4, 6.5. The differences between the 1-D and homogeneous 2-D calculations are negligible in both models. The impact of a gradients along the instrument line-of-sight act to increase the calculated radiance (by up to 16% for the gradients used in this study) with the largest increases at the line-centres and at tangent altitudes in the upper troposphere and lower stratosphere.

The differences in the radiances calculated by the two models are shown to be less than 0.1% for each of the three atmospheric scenarios, indicating that, in light of the difference between the two models being the Curtis-Godson approximation, the radiance calculation in the FM2D provides suitably accurate radiance values.

Radiative transfer calculations performed by the FM2D and the RFM in 1-D have been compared to results from other radiative transfer models as part of the Advanced MIPAS Level 2 Data Analysis (AMIL2DA) project (von Clarmann et al., 2003), which was aimed at the detection of forward model deficiencies for retrievals from the MIPAS data.

# Chapter 7

# MIPAS 1-D Retrievals

Linear analysis of 1-D ozone retrievals has been performed for simulated MIPAS spectra by computing weighting functions with the FM2D. In chapter 2, the main ozone infrared bands are described as being approximately located at $\nu_1 = 1103$, $\nu_3 = 1042$ and $\nu_2 = 701$ cm$^{-1}$ and, therefore, weighting functions are only computed for spectra covering MIPAS bands A (685 to 970 cm$^{-1}$) and AB (1020 to 1170 cm$^{-1}$). Figures 7.1 and 7.2 show radiance spectra for the most significant line absorbers in MIPAS bands A and AB calculated with the RFM at a tangent altitude of 21 km. Figure 7.1 shows that the ozone radiance between approximately 850 and 950 cm$^{-1}$ is considerably less than the NESR, and for the rest of this chapter band A refers to the spectral range from 685 to 850 cm$^{-1}$.

## 7.1 Retrieval Scheme

Each MIPAS band is divided into 1 cm$^{-1}$ wide spectral regions, or *microwindows*, based on the wide spectral grid used by the FM2D to calculate radiance and Jacobian spectra. Weighting functions are computed numerically, for a 1% perturbation of the vmr profile at each level, at the MIPAS unapodised spectral resolution (0.025 cm$^{-1}$). The radiances are convolved with the instrument line

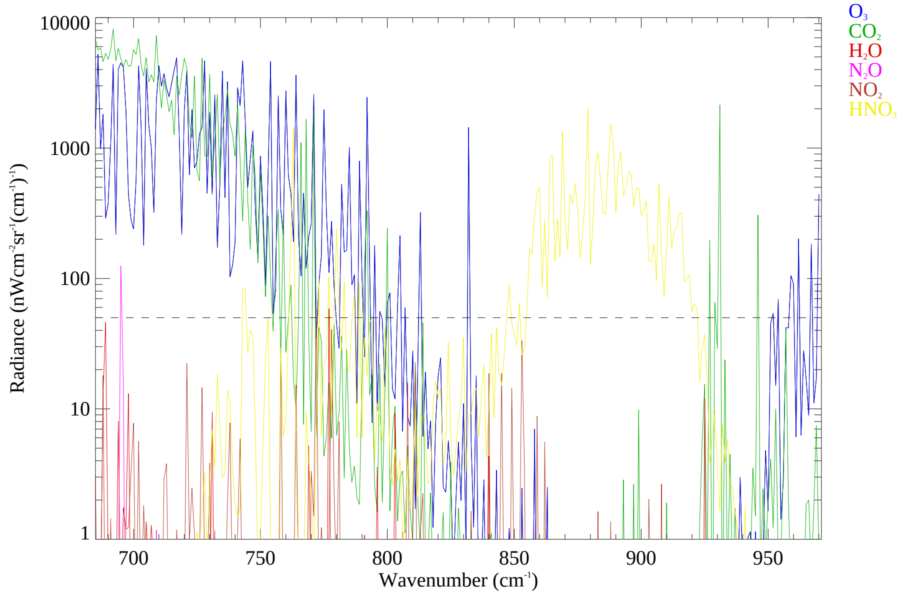

Figure 7.1: RFM radiance spectra at 21 km for $O_3$, $CO_2$, $H_2O$, $N_2O$, $NO_2$ and $HNO_3$ in MIPAS band A. The dashed line shows the NESR of 50 nW cm$^{-2}$ sr$^{-1}$ (cm$^{-1}$)$^{-1}$.

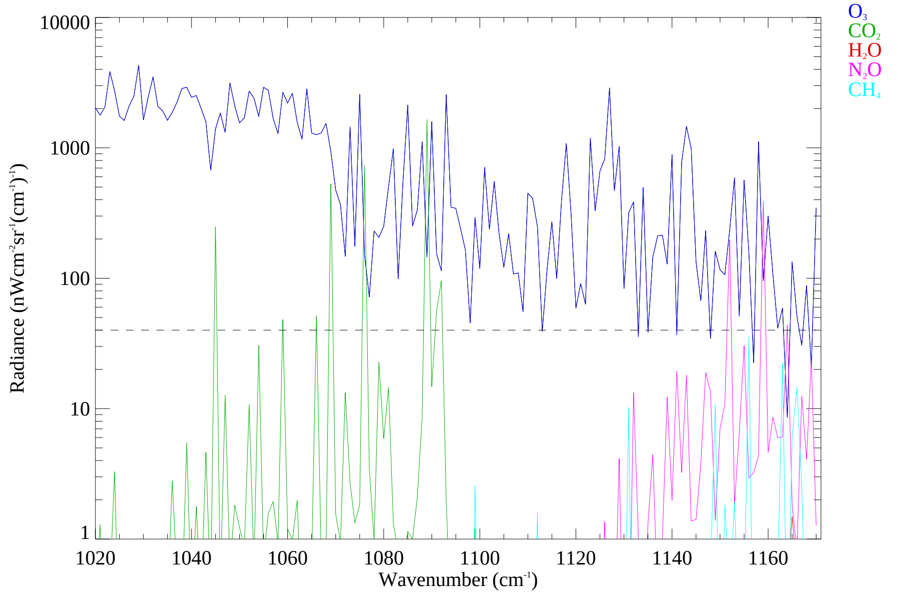

Figure 7.2: RFM radiance spectra at 21 km for $O_3$, $CO_2$, $H_2O$, $N_2O$ and $CH_4$ in MIPAS band AB. The dashed line shows the NESR of 40 nW cm$^{-2}$ sr$^{-1}$ (cm$^{-1}$)$^{-1}$.

shape at each spectral point in the microwindow.

### 7.1.1 Definition of the atmosphere and sensor

In the FM2D, the atmosphere and sensor are defined by two driver files, both of which are required in order to run the radiance and weighting function calculations.

The driver file for the sensor defines the radiance calculation in terms of the sensor characteristics and viewing geometry from the satellite. In these simulations, the total radiance is calculated, with refraction, for a satellite altitude of 820 km viewing the limb at the tangent altitudes in the MIPAS nominal observation mode: 68, 60, 52, 47 km, and 42 to 6 km in 3 km steps (see chapter 3). An extra retrieval level is added to this scan pattern at 3 km in order to take into account that the state of the atmosphere below the measurement range is not necessarily fully known. Five pencil-beam views are used to represent each MIPAS limb view; these paths are defined from 1.5 to 69.5 km in 0.5 km intervals for the nominal scan pattern. Spectral line data is provided by the MIPAS spectroscopic database, which is based on HITRAN96 but including improvements made on the basis of comparisons to spectral measurements made by the ATMOS instrument and new laboratory data. For the spectral convolution, a separate file (referred to as FILTER_FILE) is required which specifies the normalised ILS function (upper plot in Figure 7.3) at each spectral point in the microwindow. The field of view (FOV) convolution is performed at each specified tangent altitude in the scan pattern, with the normalised FOV function (lower plot in Figure 7.3). The spacing of monochromatic radiance calculations is set to 0.002 $\text{cm}^{-1}$, and the monochromatic calculations are performed with each microwindow expanded by $\pm 0.8$ $\text{cm}^{-1}$ to take into account wings of lines beyond the edges of each microwindow.

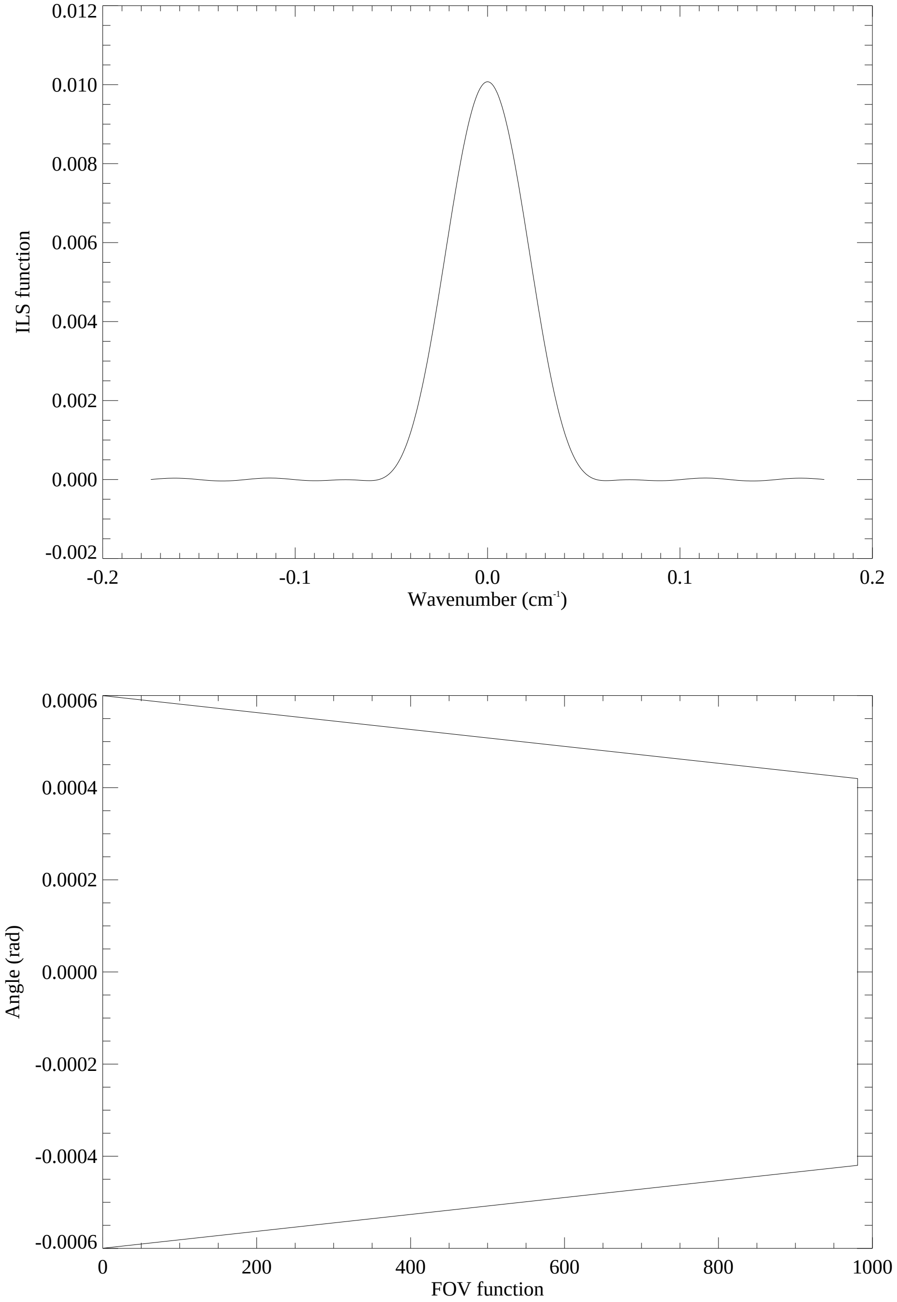

Figure 7.3: The normalised instrument line shape (upper plot) and field of view (lower plot) functions used in this retrieval study.

An important consideration for any retrieval scheme is the effect of *continuum* emissions on the spectral intensity of a measurement. There are three main sources of continuum emissions:

- instrumental continuum: due to, for example, uncorrected self-emission by the instrument which can be represented as a wavenumber dependent offset to the spectrum. This effect is removed in the radiometric calibration of the instrument.
- spectrally near continuum: due to atmospheric lines just outside the expanded microwindow.
- spectrally far or aerosol/cloud continuum: due to, for example, the wings of far lines (of which water vapour lines are the most important).

Near continuum effects (up to $\pm 25$ cm$^{-1}$ of the current microwindow) in the FM2D are calculated line-by-line for the two microwindows adjacent to the current microwindow. Far continuum effects are calculated by the FM2D for lines more than $\pm 25$ cm$^{-1}$ of the current microwindow, and quadratically interpolated to the edges and mid-point of the current microwindow. Vertical profiles of continuum used in this retrieval scheme are provided by the CKD (Clough et al., 1989) model for water vapour.

For each microwindow, the wavenumbers of the spectral points in the microwindow are determined and added to the FILTER_FILE definition (which is designed for a generalised microwindow starting at 0). The sensor driver is then updated with the spectral data for the current microwindow. The state vector is set up to include the profiles of each of the products (i.e. each specified gas and the continuum climatology) which are to be retrieved.

For the simulations presented here, the atmosphere is defined for a latitude of 45° with atmospheric levels spaced at 1 km intervals between 0 and 100 km. Reference atmospheric profiles for temperature, pressure and gas mixing ratio are as described in chapter 6 (MIPAS mid-latitude day). Weighting functions are calculated for two different atmospheres: (i) an ozone only atmosphere, and (ii) an atmosphere including ozone and the most significant line absorbers. These line absorbers are determined by running the RFM with the wildcard character in the *GAS section of the RFM driver (see the RFM User's Guide (Dudhia, 1999b)). In band A the gases included in the atmosphere are $\mathrm{O_3}$, $\mathrm{CO_2}$, $\mathrm{H_2O}$, $\mathrm{N_2O}$, $\mathrm{NO_2}$ and $\mathrm{HNO_3}$, and in band AB the gases included in the atmosphere are $\mathrm{O_3}$, $\mathrm{CO_2}$, $\mathrm{H_2O}$, $\mathrm{N_2O}$ and $\mathrm{CH_4}$. It is important to note that this is not a comprehensive list of the gases with spectral features in bands A and AB, and there are also significant contributions from trace species with broad spectral features, such as CFCs, and the impact of these on the calculated radiance and weighting functions will be discussed in section 7.5.1. The radiance spectra of the gases listed here have radiance values significantly greater than the noise value of the MIPAS band.

### 7.1.2 The Fisher information matrix

Each weighting function matrix has dimensions of ($N_y \times N_x$) which are the number of elements in the measurement vector $\mathbf{y}$ and state vector $\mathbf{x}$ respectively. For MIPAS, the number of measurements is the number of spectral points in each microwindow multiplied by the number of measurement altitudes in the selected part of the scan pattern (i.e. for spectra measured with the nominal scan pattern defined above, at 0.025 cm$^{-1}$, $N_y = 680$). The retrieval diagnostics presented in this chapter are the retrieval error covariance and averaging kernel matrices $\mathbf{S}_x$

and $\mathbf{A}$:

$$\mathbf{S}_x = (\mathbf{S}_a^{-1} + \mathbf{K}^T\mathbf{S}_y^{-1}\mathbf{K})^{-1} \tag{7.1}$$

$$\mathbf{A} = \mathbf{S}_x\mathbf{K}^T\mathbf{S}_y^{-1}\mathbf{K} \tag{7.2}$$

The computation of both of these diagnostics are dependent on the matrix $\mathbf{K}^T\mathbf{S}_y^{-1}\mathbf{K}$, which is also known as the Fisher information matrix (see chapter 4). In the RAL retrieval scheme, the $\mathbf{S}_y$ matrix is assumed to be diagonal, and the $\mathbf{K}^T\mathbf{S}_y^{-1}\mathbf{K}$ is accumulated for successive microwindows in order to calculate the retrieval diagnostics:

$$\mathbf{K}^T\mathbf{S}_y^{-1}\mathbf{K} = \sum_{i=1,N} (\mathbf{K}_i^T\mathbf{K}_i)/(\sigma_i^2) \tag{7.3}$$

where $\mathbf{K}_i$ is the weighting function matrix of the $i$th microwindow and $\sigma$ is the measurement error. The $\mathbf{K}^T\mathbf{S}_y^{-1}\mathbf{K}$ matrix has dimensions of $(N_x \times N_x)$ so accumulating this saves having to store the $(N_y \times N_x)$ weighting function and $(N_y \times N_y)$ $\mathbf{S}_y$ matrices. In the retrieval, the measurement error is set to 1 nW cm$^{-2}$ sr$^{-1}$ (cm$^{-1}$)$^{-1}$ for each microwindow, and the $\mathbf{K}^T\mathbf{S}_y^{-1}\mathbf{K}$ matrix is scaled by the required measurement error later. The measurement error is assumed to be independent of $i$ (i.e. no dependence on the limb-view or wavelength within each microwindow).

The state vector contains the ozone profile and continuum profiles, for the start and end wavenumbers of the microwindow, defined on a vertical grid from 0 to 100 km in 1 km intervals. The $\mathbf{K}^T\mathbf{S}_y^{-1}\mathbf{K}$ matrix is calculated on this grid, and *regridded* onto the MIPAS scan pattern by calculating the matrix which maps triangular basis functions on the 1 km grid to triangular basis functions on the

MIPAS scan pattern (i.e. 3 km spacing). In general

$$\mathbf{A} = \mathbf{M}^T\mathbf{B}\mathbf{M} \tag{7.4}$$

where $\mathbf{A}$ and $\mathbf{B}$ are square matrices with dimensions of $(N_a \times N_a)$ and $(N_b \times N_b)$ respectively, $\mathbf{M}$ is the mapping matrix with dimensions of $(N_a \times N_b)$. The regridding is performed by converting the matrix on the original grid to the matrix per unit grid spacing, and then convolving this function with the new basis. Figure 7.4 shows the $\mathbf{K}^T\mathbf{S}_y^{-1}\mathbf{K}$ matrix before (left-hand plot) and after (right-hand plot) the regridding procedure.

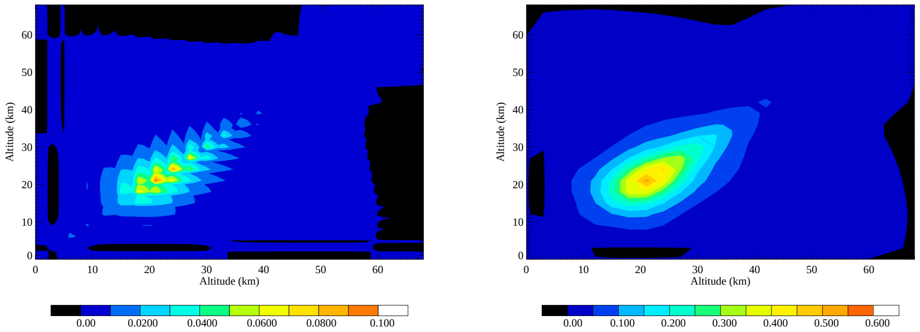

Figure 7.4: The $\mathbf{K}^T\mathbf{S}_y^{-1}\mathbf{K}$ matrix for the 750 cm$^{-1}$ microwindow on the 1 km (left-hand plot) and MIPAS nominal scan pattern (right-hand plot) retrieval grids.

### 7.1.3 Cholesky decomposition

The matrices required (i.e. $\mathbf{K}^T\mathbf{S}_y^{-1}\mathbf{K}$, $\mathbf{S}_a$ and $\mathbf{S}_x$) for the 1-D linear analysis presented here are symmetric positive definite with dimensions of $(N_x \times N_x)$. One of the fastest numerical techniques for performing linear algebra with symmetric matrices is the Cholesky decomposition. This method writes a symmetric matrix $\mathbf{A}$ as the product of a lower and an upper triangular matrix:

$$\mathbf{A} = \mathbf{T}^T\mathbf{T} \tag{7.5}$$

This operation is performed relatively quickly in $n^3/6$ operations (where, $n = N_x$) compared to Gaussian triangulation which takes $n^3/3$ operations (Press et al., 1993).

Cholesky decomposition is used in this chapter to calculate the inverse of matrices and is also used in the entropy calculation described in the next section.

### 7.1.4 Retrieval random errors

Random errors in the retrieval are calculated using equation (7.1) with the measurement error covariance replaced with the measurement noise error covariance (i.e. $\mathbf{S}_y = \mathbf{S}_\epsilon$). In this case the $\mathbf{K}^T\mathbf{S}_y^{-1}\mathbf{K}$ matrix is scaled by the measurement noise squared (see equation (7.3)) and, therefore, $\sigma$ is the NESR value for the MIPAS band. The *a priori* error covariance $\mathbf{S}_a$ is also assumed to be diagonal and the diagonal elements of $\mathbf{S}_a$ are the *a priori* error profile squared. The *a priori* errors are 100% at all levels (i.e. the *a priori* error has the same values as the *a priori* profile). Figure 7.5 shows the square root of the diagonal elements of the retrieval random error covariance matrices for each 1 cm$^{-1}$ wide microwindow in MIPAS bands A (upper plot) and AB (lower plot). The lowest errors, less than 5%, are shown to be located at the strong emission lines near the centres of the vibration-rotation bands. This is most clearly shown for band AB around the $\nu_3$ band, centred at 1042 cm$^{-1}$.

### 7.1.5 Summary

The random errors calculated for the retrieval scheme described in this section are shown, in Figure 7.5, to vary considerably with altitude and wavenumber. By using subsets of microwindows in different spectral regions, it should be possible to optimise the retrieval in order to sound different altitude ranges in the atmosphere.

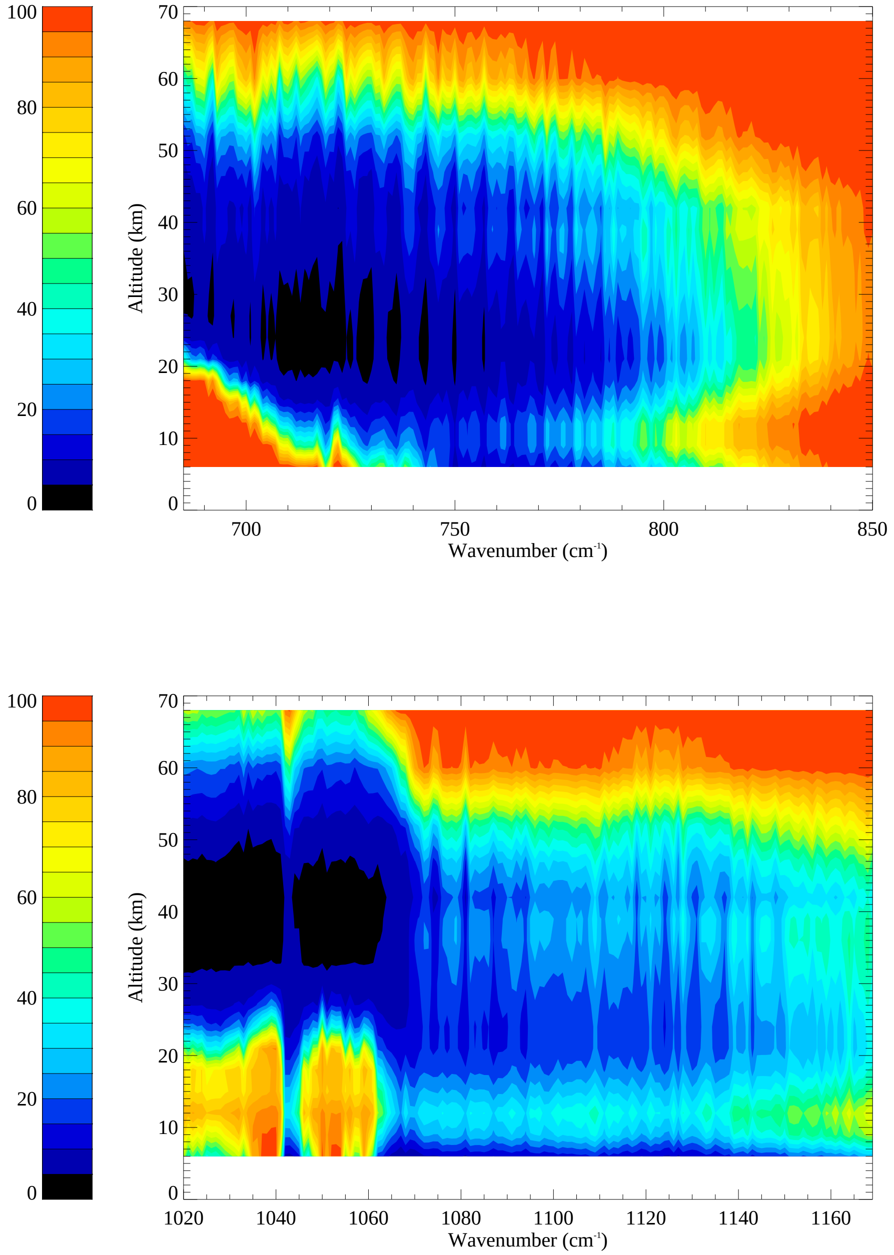

Figure 7.5: Distribution of retrieval random errors (% vmr) for each 1 cm$^{-1}$ microwindow, over altitude and wavenumber. MIPAS bands A (685 to 850 cm$^{-1}$) and AB (1020 to 1170 cm$^{-1}$) are shown in the upper plot and lower plot respectively.

Ozone has strong emission lines near the centre of its vibration-rotation bands, which saturate at between 20 and 30 km in band A ($\nu_2$), and between 35 and 45 km in band AB ($\nu_3$). The $\nu_3$ lines are much stronger than the $\nu_2$ lines and this is reflected in the higher altitude range. Away from the band centres, the emission lines are weaker, as they are also in the wings of the strongest lines, and it should be possible to sound lower in the atmosphere. Therefore, by focusing on spectral regions away from the strongest lines in the two bands it is possible to optimise the microwindows for retrieving ozone at lower altitude ranges in the atmosphere. A method for selecting subsets of microwindows appropriate for sounding lower in the atmosphere is discussed in the next section.

## 7.2 Microwindow Selection

As described above, each MIPAS spectral band is divided into 1 cm$^{-1}$ wide microwindows, and ozone retrieval random errors computed for each one. Rather than include all potential microwindows in the MIPAS band, it is more efficient to determine the *optimum* microwindows based on the improvement in $\mathbf{S}_x$ when each microwindow is included in the retrieval. This ‘microwindow selection’ is based on the information content of each microwindow, the theory for which is described in chapter 4. In this section, the microwindow selection scheme is described and microwindows selected for a full profile retrieval and a retrieval with particular emphasis on the lower atmosphere, i.e. the upper troposphere/lower stratosphere especially, are discussed.

### 7.2.1 Information content analysis

Initially, the entropy of the *a priori* error covariance is calculated, which is a measure of information about the state of the atmosphere before any measurements have been included in the retrieval.

The entropy of a given error covariance matrix is calculated via a Cholesky decomposition of the matrix to obtain the upper triangular of the matrix. The determinant of a triangular matrix is the product of its diagonal elements, and the determinant of the retrieval error covariance matrix is then simply the sum of these products squared (since $\mathbf{S} = \mathbf{T}^T\mathbf{T}$ from equation (7.5)).

The stored $\mathbf{K}^T\mathbf{S}_y^{-1}\mathbf{K}$ matrix for each of the microwindows in the required spectral range (i.e. MIPAS bands A and AB both separately and together, see below) is read into the routine, and the retrieval error covariance calculated, in order to calculate the entropy for each microwindow. The entropy for each microwindow in turn is then subtracted from the *a priori* entropy, and the microwindow which gives the largest reduction, i.e. the largest improvement in information content, is saved as the best microwindow and removed from the list. Figure 7.6 shows the variation of information content with wavenumber in the two MIPAS bands for an ozone only atmosphere before the first microwindow is selected. The entropy of the first selected microwindow is then used as the new '*a priori*' entropy (i.e. the entropy of the knowledge of the system before another measurement is included). The entropy of the remaining microwindows is recalculated, in the same way as described above, and the one which provides the highest information content is selected as the next best one and removed from the list. This process is repeated iteratively until all of the microwindows in the spectral range have been selected.

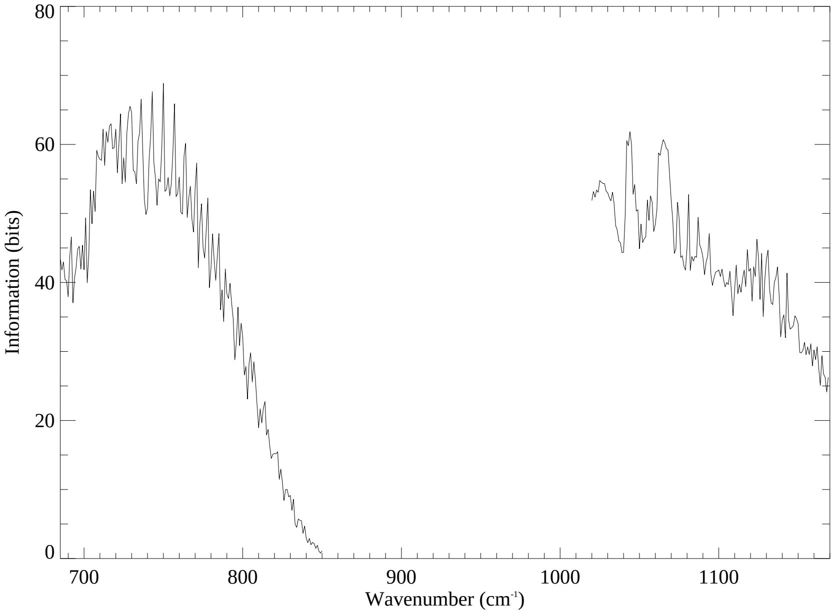

Figure 7.6: "Total" information spectrum over MIPAS bands A and AB for an ozone only atmosphere.

### 7.2.2 Selective altitude range

The information content analysis described in the previous section is for selecting microwindows for a full profile retrieval. The spectral distribution of this 'total' information content (Figure 7.6) is not necessarily the same as for a subset of altitudes in the profile. This implies that, by calculating the information content over a specified altitude range, it may be possible to select microwindows which are better optimised for that range of altitudes. The microwindow selection scheme operates in the same way as described in the previous section except only the elements of the $\mathbf{K}^T\mathbf{S}_y^{-1}\mathbf{K}$, and hence the error covariance $\mathbf{S}_a$ and $\mathbf{S}_x$, matrices corresponding to the chosen altitude range are used in the entropy calculation. That is to say, a new matrix is constructed by taking the elements corresponding to the chosen altitude range from the original matrix. Figure 7.7 shows the $\mathbf{K}^T\mathbf{S}_y^{-1}\mathbf{K}$ matrix from the right-hand plot in Figure 7.4, indicating the elements corresponding to an altitude range from 6 to 24 km with the superimposed grid.

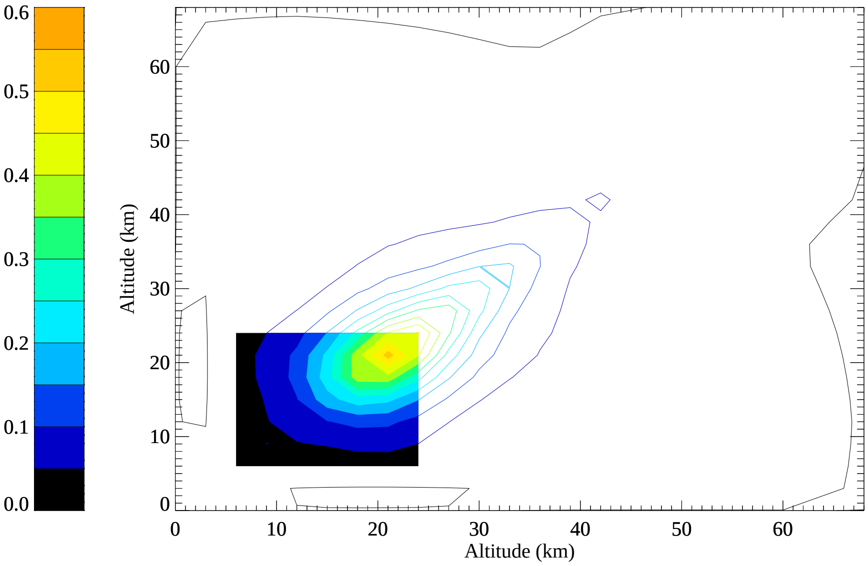

Figure 7.7: The $\mathbf{K}^T\mathbf{S}_y^{-1}\mathbf{K}$ matrix for the 750 cm$^{-1}$ microwindow on the MIPAS nominal scan pattern showing the elements of the matrix for a selected altitude range of 6 to 24 km.

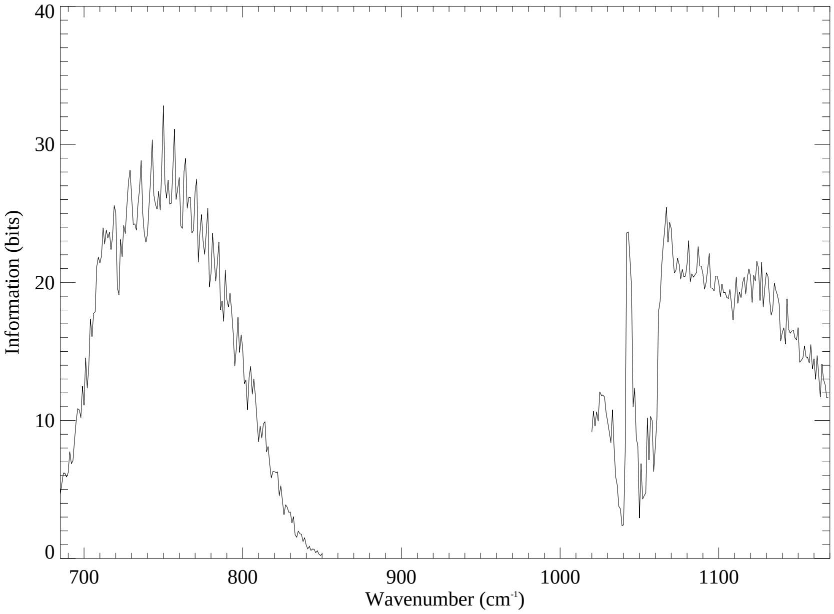

Figure 7.8: Information spectrum over MIPAS bands A and AB for an altitude range from 6 to 24 km.

The information spectrum for the selected altitude range, over MIPAS bands A and AB for an ozone only atmosphere, is shown in Figure 7.8. Comparison of this figure with Figure 7.6, for the full profile, shows that for a narrower altitude range, the total information content decreases as less measurements are being used. The information content calculated over 6 to 24 km is considerably reduced at the centres of the ozone vibration-rotation bands, especially the $\nu_3$ band, where the strongest ozone lines black out at altitudes above 24 km. In Figure 7.8, it is clear that there is more information away from the band centres and, therefore, the microwindow selection is biased towards those spectral regions compared to the full profile microwindow selection, where the band centres are slightly more dominant. This is further illustrated in Figure 7.9, which compares the spectral distribution of the microwindow selection for the full profile and lower atmosphere. The difference in microwindow selection is more obvious in band AB where the centres of the strongest ozone lines around 1042 $\text{cm}^{-1}$ saturate around 40 km.

### 7.2.3 Results for an ozone only atmosphere

The microwindow selection results for the full profile (6 to 68 km) and selected altitude range (6 to 24 km) in an ozone only atmosphere are shown in Figure 7.9. In this figure, the information content of each microwindow, after it has been selected, is plotted against wavenumber to show the distribution of the microwindow selection. The black crosses show the microwindow selection for the whole altitude range of the MIPAS measurements (i.e. 6 to 68 km), and the red crosses show the microwindow selection for the 6 to 24 km altitude range. The information content values in this plot are approximately $10^2$ smaller than the values in Figure 7.8 as the information content of each microwindow is calculated relative to the previously selected microwindow, whereas Figure 7.8 shows the information content of each microwindow relative to the *a priori* (i.e. before any microwindows have

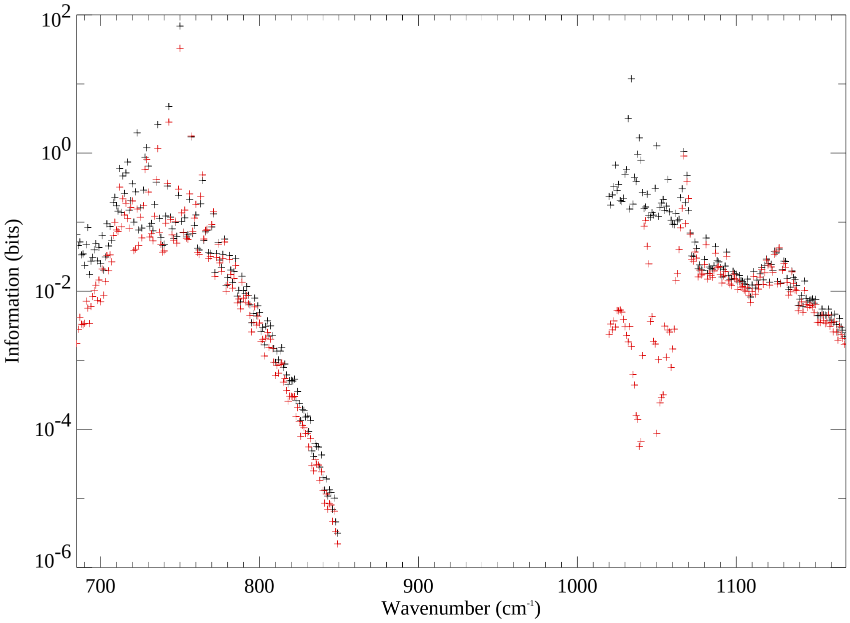

Figure 7.9: Distribution of microwindows selected from MIPAS bands A and AB for 6 to 68 km (black crosses) and 6 to 24 km (red crosses).

been selected). The shape of the information spectrum is clearly reflected in the shape of the distribution of the microwindow selection.

The purpose of selecting microwindows over the selected altitude range, as opposed to the full profile, is to optimize the retrieval for the desired altitude range. Figure 7.10 shows the difference in the random error profiles, over the full profile, for the two sets of microwindows listed in Table 7.1. The black line is the error profile for the scheme to select microwindows for the full profile, and the red line is the error profile for the microwindows selected over the 6 to 24 km altitude range. The retrieved random errors are improved below 24 km but worse than the full profile retrieval above 24 km. This should be expected as only the information below 24 km is used.

Table 7.1 shows the wavenumbers of the first 10 selected microwindows for the

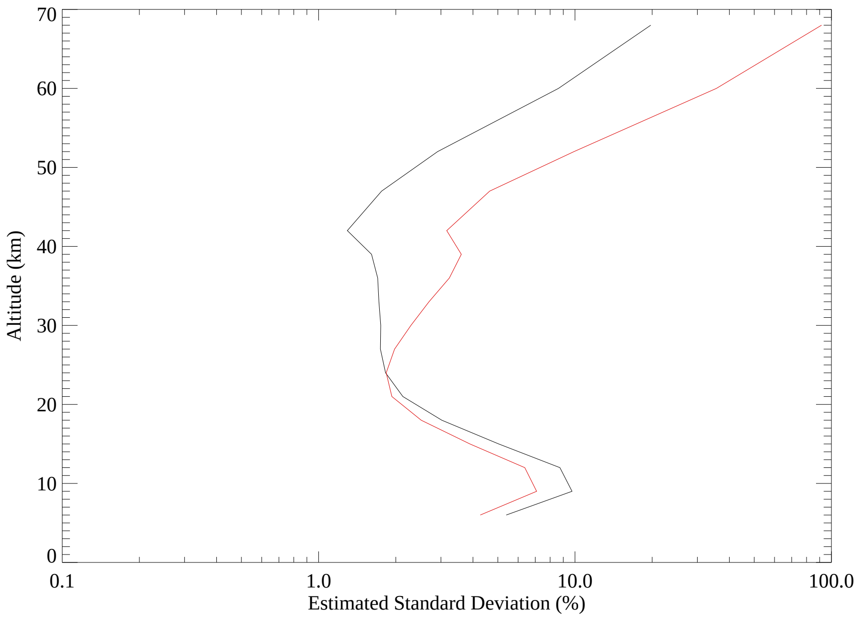

Figure 7.10: Random error profiles for the first 10 microwindows selected over the full profile (black line) compared to the microwindows selected for the 6 to 24 km altitude range (red line).

ozone only atmosphere. The 6 to 68 km and 6 to 24 km columns show the difference in the selection for the two altitude ranges. Microwindows selected from spectral band A are fairly common to both altitude ranges and lie roughly between 720 and 760 $\text{cm}^{-1}$. In spectral band AB, microwindows selected for the 6 to 68 km lie between 1030 and 1050 $\text{cm}^{-1}$ whereas from the 6 to 24 km altitude range, microwindows are only selected at wavenumbers greater than 1060 $\text{cm}^{-1}$, i.e. away from the band centre (where the radiance signal is strongest in the stratosphere around 40 km), and the information in the lower atmosphere is poor. Figure 7.11 shows the improvement in the retrieval random error in the lower atmosphere as microwindows are selected and added from MIPAS bands A, AB and the combination of the two for an ozone only atmosphere. The index on the x-axis refers to the order in which the microwindows are selected. It is clear that, for retrieving ozone in the lower atmosphere, it is considerably more efficient to select microwindows optimised for the lower atmosphere as fewer microwindows are

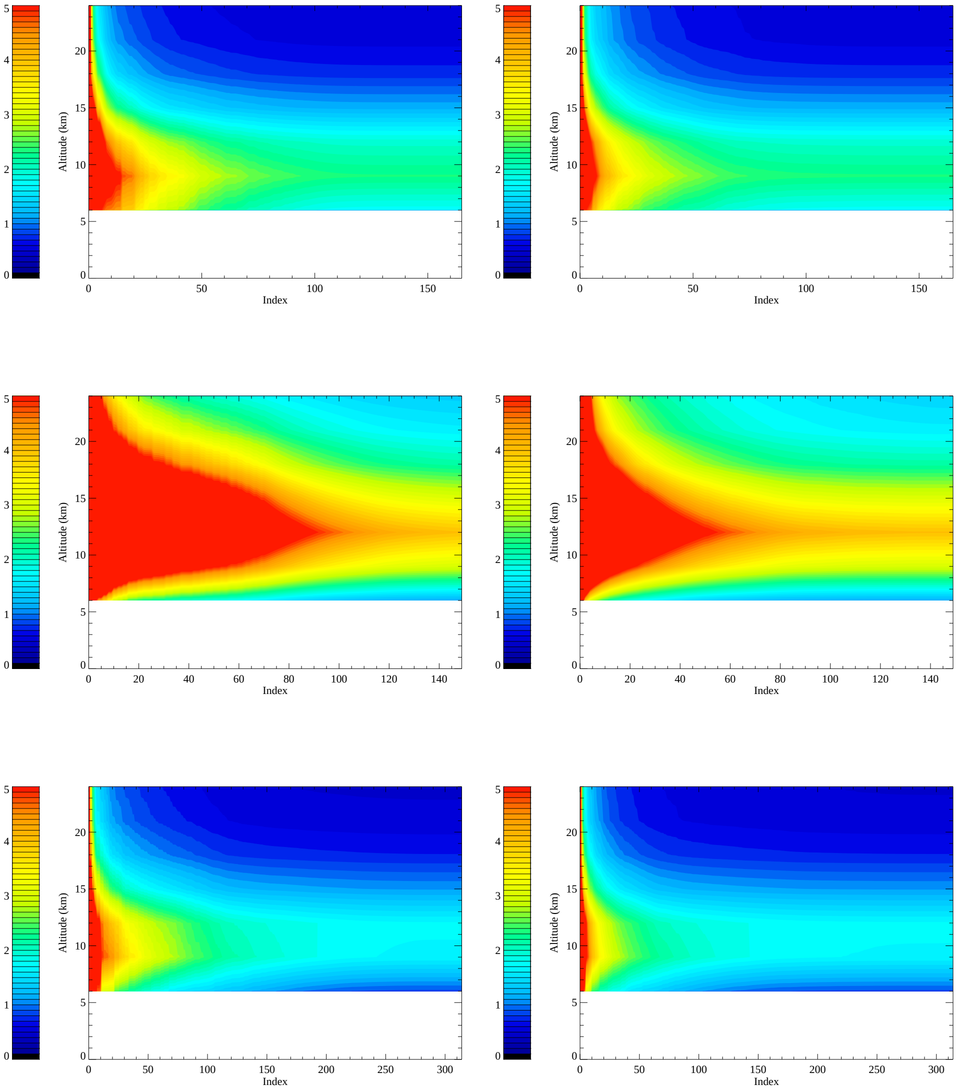

Figure 7.11: Improvement in retrieval random errors (% vmr) as microwindows selected from MIPAS band A (top row), band AB (middle row) and bands A and AB together (bottom row) are added. The plots in the left-hand column show the microwindows selected for the whole profile retrieval, and the the plots in the right-hand column show the microwindows selected for a selected altitude range of 6 to 24 km.

| Selection order | 6 to 68 km | 6 to 24 km |
|---|---|---|
| 1 | 750 | 750 |
| 2 | 1034 | 743 |
| 3 | 743 | 757 |
| 4 | 1032 | 736 |
| 5 | 736 | 1067 |
| 6 | 723 | 729 |
| 7 | 757 | 728 |
| 8 | 1039 | 764 |
| 9 | 1050 | 735 |
| 10 | 729 | 1069 |

Table 7.1: Wavenumber of the first 10 microwindows selected, over the 6 to 68 and 6 to 24 km altitude ranges, for an ozone only atmosphere.

required to obtain the same result from the full profile retrieval.

### 7.2.4 Results for an atmosphere containing line absorbers additional to ozone

So far in this chapter a hypothetical atmosphere containing ozone only has been considered as an example. In the real atmosphere, there are a large number of trace species which affect the intensity of the observed radiance. To make the microwindow selection more realistic, a number of trace gases with strong absorptions in the two MIPAS bands are included in the atmosphere and the retrieval simulation repeated to demonstrate the effect they will have on the calculated retrieval errors and information content analysis. The influence of the line absorbers on the selection is through their influence on the calculated radiance spectra, assuming that the distribution of these absorbers is well known. Vertical profiles of all of the line absorbers (including ozone) included in the atmosphere are provided by the MIPAS reference atmospheric profiles. The line absorbers included in each MIPAS band in these simulations are those listed as being of most significance at the beginning of the chapter. Figure 7.12 shows the microwindow selection results for the two altitude ranges from such an atmosphere.

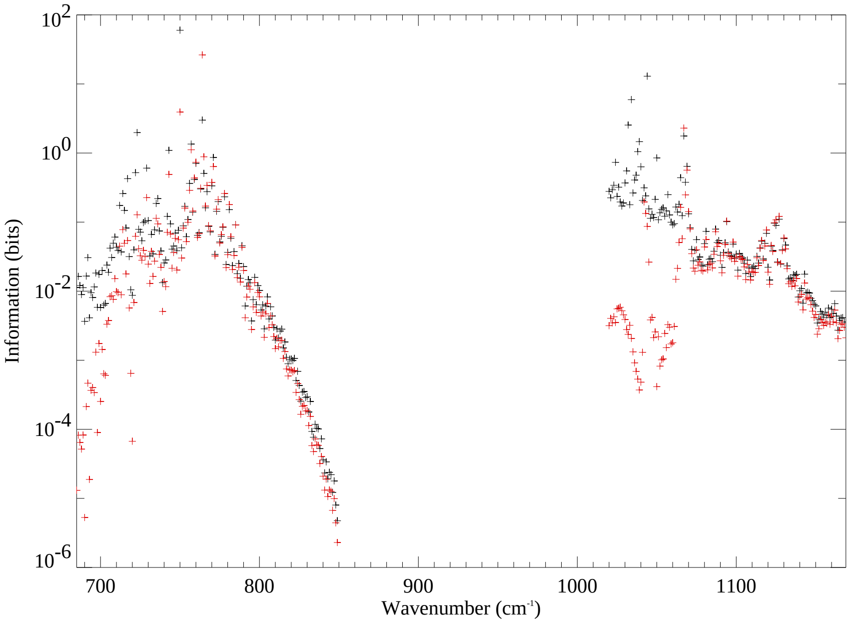

Figure 7.12: Distribution of microwindows selected from MIPAS bands A and AB for 6 to 68 km (black crosses) and 6 to 24 km (red crosses).

Table 7.2 shows the wavenumbers of the first 10 selected microwindows for the ozone and line gas atmosphere and shows the differences in the selection for the two altitude ranges. The influence of including line gas absorptions in the atmosphere on the microwindow selection can be seen by comparing Figures 7.9

| Selection order | 6 to 68 km | 6 to 24 km |
|---|---|---|
| 1 | 750 | 764 |
| 2 | 1044 | 750 |
| 3 | 1034 | 1067 |
| 4 | 764 | 757 |
| 5 | 1032 | 1065 |
| 6 | 723 | 760 |
| 7 | 1067 | 771 |
| 8 | 1039 | 1069 |
| 9 | 757 | 743 |
| 10 | 743 | 759 |

Table 7.2: Wavenumber of the first 10 microwindows selected, over the 6 to 68 and 6 to 24 km altitude ranges, for an ozone and line gas atmosphere.

and 7.12. The most obvious difference between the two figures is that microwindows selected from band A are located between 750 to 800 cm$^{-1}$ rather than lower wavenumbers, especially in the lower atmosphere, as $CO_2$ has a strong radiance signal in the 685 to 750 cm$^{-1}$ spectral range. Tables 7.1 and 7.2 show the differences in the selection of the first 10 microwindows, over the full profile and lower atmosphere, for the two atmospheres. Three microwindows are different for the full profile and four microwindows are different for the 6 to 24 km altitude range.

## 7.3 UTLS Microwindows

In this section, microwindows selected for the retrieval of ozone in the lower atmosphere are assessed in comparison to the FM2D microwindows equivalent to those selected for the ozone retrieval in the operational processor (see next section). At this stage, the most significant systematic error sources in the retrieval are also assessed, for the selected microwindows, using the Oxford University developed microwindow selection scheme MWMAKE.

### 7.3.1 Microwindow selection from MIPAS bands A and AB

Table 7.3 shows the information content calculated for the first 10, 20 and 50 UTLS ozone microwindows selected from MIPAS bands A, AB and the combination, compared to the total possible information content if all microwindows across MIPAS bands A and AB are used.

Figure 7.13 shows the random error profiles if all of the microwindows in the two MIPAS bands, seperately and in combination, are used in the retrieval. This represents the lowest achievable random errors for the described retrieval scheme. Figure 7.14 shows the random error profiles for the first 10 (solid line), 20 (dashed

| MIPAS band | 10 MWs | 20 MWs | 50 MWs | 315 MWs |
|---|---|---|---|---|
| A | 81.17 | 88.46 | 98.84 | 105.28 |
| AB | 73.65 | 81.04 | 93.37 | 113.33 |
| A + AB | 84.26 | 91.51 | 101.36 | 121.22 |

Table 7.3: Information content (bits), for the 6 to 24 km altitude range, of the first 10, 20 and 50 selected microwindows from MIPAS bands A and AB individually and in combination. The last column shows the information content if all of the 315 available microwindows are used in the selection.

line) and 50 (dot-dash line) selected microwindows in each of the MIPAS bands. The red lines show the microwindows selected from band A, the green lines represent band AB and the black line represents the combined bands. The three 3 cm$^{-1}$ wide ozone microwindows used in the ESA operational processor (763.375 to 766.375 cm$^{-1}$, 1073.800 to 1076.800 cm$^{-1}$, and 1122.800 to 1125.800 cm$^{-1}$), shown as the solid blue line in the figure, are represented by the FM2D microwindows covering the same spectral range. This figure shows that microwindow selection from the combination of bands A and AB largely reflects that from band A alone, although the microwindows in band AB help to improve the errors at 9 and 6 km. The reason for this is illustrated by comparing the two plots in Figure 7.5: it is only at 6 and 9 km where the precision in the altitude range up to 24 km is better from band AB microwindows (especially between approximately 1065 and 1150 cm$^{-1}$) than band A microwindows (730 to 810 cm$^{-1}$). It would appear from Figure 7.14 that an improvement in random error in the 6 to 24 km altitude range of factor 2 to 4 over the operational microwindows appears feasible with 10 microwindows.

### 7.3.2 Systematic error sources

The microwindow selection described here is based on the improvement in the retrieval random error alone whereas the total retrieval error is actually the sum of the random error with the systematic error. Sources of systematic error in a

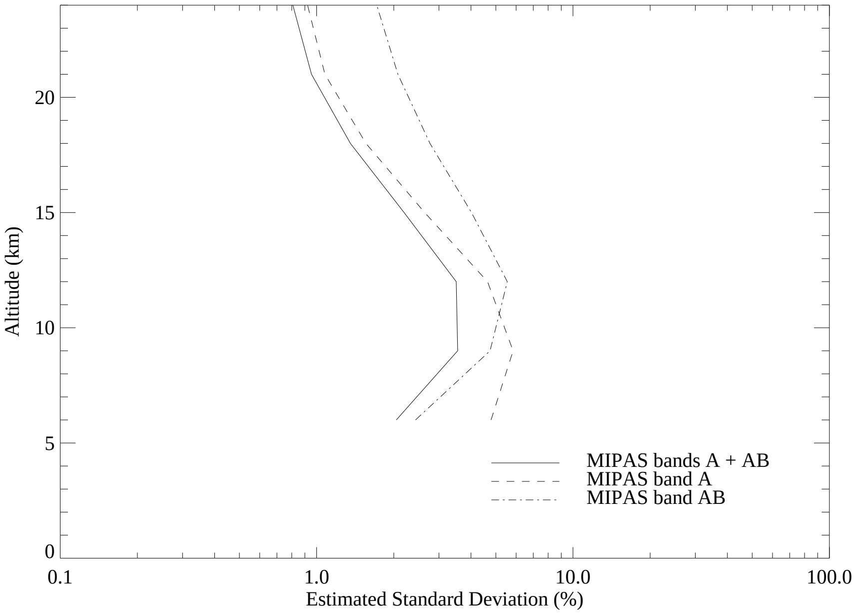

Figure 7.13: Estimated standard deviations calculated for all microwindows in MIPAS bands A and AB.

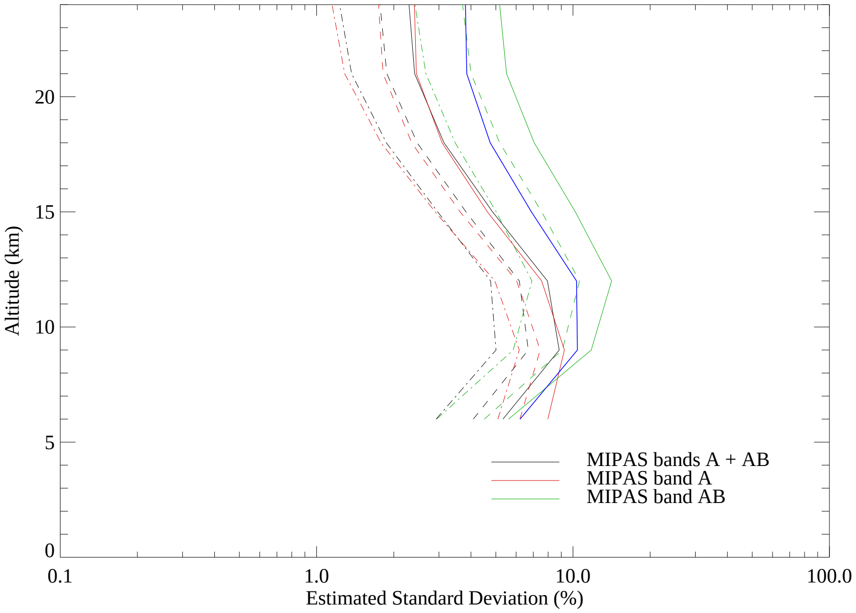

Figure 7.14: Random error profiles for microwindows selected from MIPAS bands A (red line), AB (green line) and the combination (black line) compared to the "operational" microwindows (blue line). For each set of selected microwindows, the solid, dashed and dot-dash lines represent the first 10, 20 and 50 selected microwindows respectively.

retrieval utilizing the microwindows selected for the lower atmosphere are evaluated with the Oxford University microwindow selection programme MWMAKE. It is possible with the MWMAKE programme to evaluate the improvement in retrieval error due to a given set of microwindows. The selection is performed on a pre-computed set of Jacobian spectra and it is important to note that these spectra are not identical to those computed by the FM2D for this study. In this part of the study the MWMAKE routine is used as a tool to highlight the most important sources of systematic error in the retrieval for the selected microwindows. Figure 7.15 shows the most significant sources of systematic error for the first 10

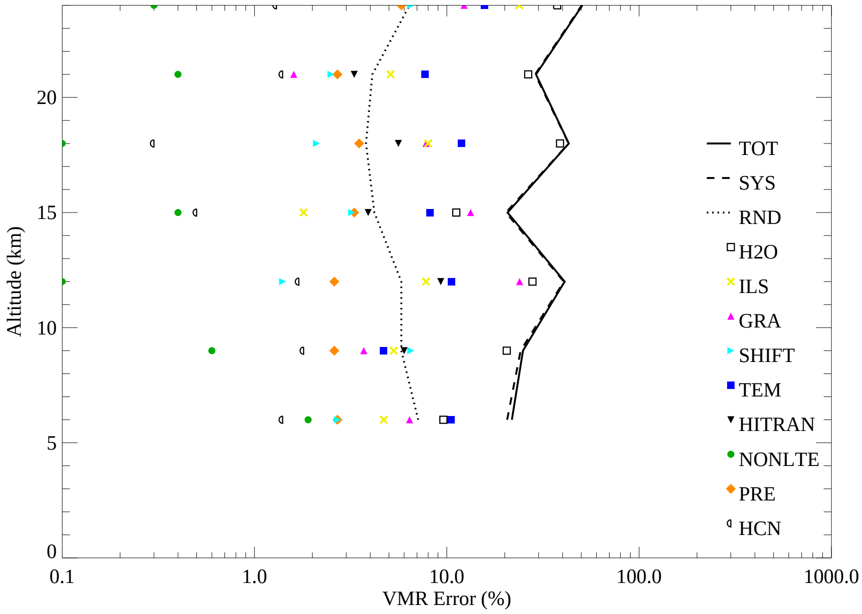

Figure 7.15: Sources of systematic error for the first 10 selected microwindows in the 6 to 24 km altitude range. See Table 7.2.

microwindows selected for an altitude range covering 6 to 24 km. The most significant systematic errors (i.e. larger than the random error) are GRA, ILS, TEM, H2O and HITRAN. Potential error sources are assessed by MWMAKE using pre-calculated perturbation spectra. Perturbation spectra for temperature are the same as the temperature Jacobian spectra (i.e. the difference in radiance spectra with and without a 1 K temperature perturbation). Uncertainties in composition represent the differences between spectra calculated for the nominal atmosphere and one perturbed by its estimated climatological variability ($\pm 1\sigma$). Other potential error sources are defined as follows:

- GRA - effect of ignoring a 1 K per 100 km horizontal gradient in temperature
- HITRAN - uncertainties in the HITRAN database (not including uncertainties in absolute line strength)
- ILS - uncertainties in the ILS function
- SHIFT - uncertainty in spectral calibration (0.001 cm$^{-1}$)

Figure 7.15 shows how the impact of these systematic error sources on the retrieval is to significantly increase the total error compared to the random error. The impact of these systematic errors can be accounted for in the selection of microwindows by including them in the measurement error covariance matrix $\mathbf{S}_y$. The magnitude of the systematic errors can also be reduced if they can be retrieved.

## 7.4 1-D Error Analysis

In this section, retrieval diagnostics are presented from FM2D calculations for the UTLS microwindows selected as described in the previous sections. These retrieval diagnostics are the random error profiles (i.e. the square root of the diagonal elements of the retrieval error covariance matrix), averaging kernels and information content. Firstly, diagnostics for the microwindows selected for the nominal MIPAS observing mode (68, 60, 52, 47 and 42 to 6 km in 3 km steps), optimized for the UTLS are presented, and these diagnostics are compared to those for a special MIPAS observing mode (labelled S6) which has a scan pattern restricted to the lower atmosphere (35, 28 and 24 to 6 km in 2 km intervals).

### 7.4.1 MIPAS nominal scan pattern

Presented here are the linear diagnostics for the MIPAS nominal scan pattern retrieval grid. The first 10 microwindows selected for the altitude range from 6 to 24 km, as described above, are used to calculate the retrieval error covariance and averaging kernels.

#### Vertical resolution

Figure 7.16 shows the averaging kernels calculated for the first 10 microwindows selected for the lower atmosphere but applied to the nominal scan pattern. The left-hand plot shows averaging kernels on a 1 km retrieval grid, and the right-hand plot shows averaging kernels on the nominal scan pattern. It is clear from the left-hand plot that a vertical resolution of 1 km is not achievable as the averaging kernel peaks between the tangent altitudes only have values of approximately 0.4 compared to peak values between 0.5 and 0.7 at the tangent altitudes. In the right-hand plot, the retrieval levels are coincident to the tangent altitudes and the averaging kernels peak at 1.0 at each tangent altitude. Therefore, only the retrieval on the MIPAS nominal scan pattern is considered.

#### Error profiles

Figure 7.17 shows the *a priori*, smoothing, noise and random error profiles for the first 10 microwindows selected for the 6 to 24 km altitude range but applied to the nominal scan range. The random errors are less than about 7% in the lower atmosphere, with the highest values at 9 and 12 km.

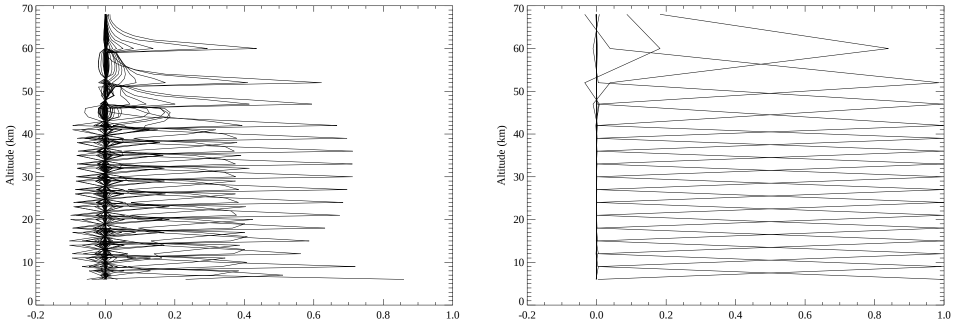

Figure 7.16: Averaging kernels for the first 10 selected microwindows in the UTLS. The left-hand plot shows averaging kernels calculated on a 1 km retrieval grid and the right-hand plot shows averaging kernels calculated on the MIPAS nominal scan pattern retrieval grid.

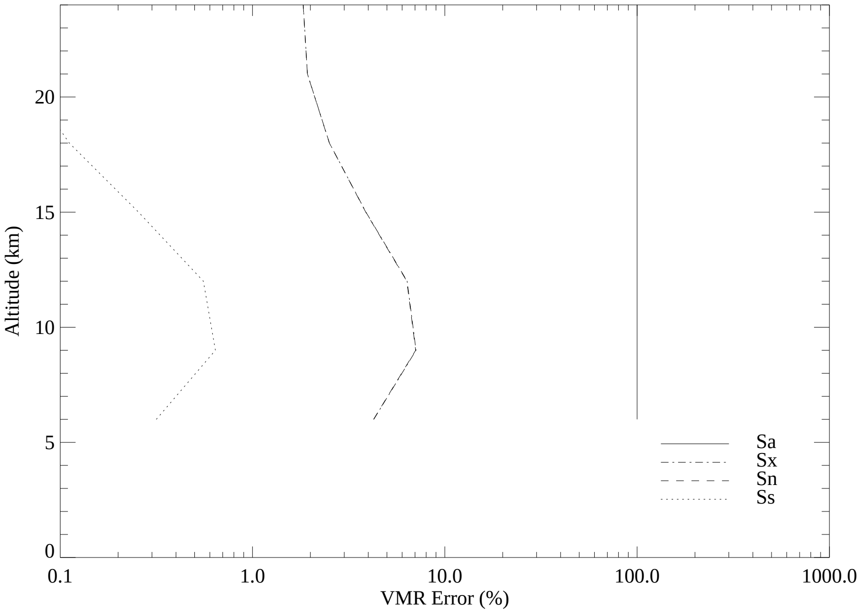

Figure 7.17: Error profiles for the first 10 microwindows selected in the lower atmosphere retrieved for the MIPAS nominal scan pattern at 3 km retrieval level spacing. The solid, dot-dash, dashed and dotted lines represent the a priori (Sa), random (Sx), noise (Sn) and smoothing (Ss) errors, respectively. Note that the random and noise errors are superimposed.

## 7.4.2 MIPAS observing mode S6

### Retrieval scheme

The retrieval scheme for the MIPAS special observing mode S6 is essentially the same as that described earlier in this chapter for the MIPAS nominal scan pattern.

There are, however, some differences in the set up to take into account the different vertical extent and resolution, and spectral resolution, of the measurements. The interferometer travel time, and hence the maximum optical path difference and spectral resolution of the measurements, is reduced by a factor of four relative to the nominal scan pattern. This means that a quarter of the interferogram is measured in a quarter of the time of the nominal scan. Assuming that the detector noise is constant, and that the noise is specified per unit wavenumber, the NESR is proportional to the square root of the scan time. For the nominal observing mode the NESR values $\epsilon_N$ for MIPAS bands A and AB have pre-calibration values of 50 and 40 $\mathrm{nW\,cm^{-2}\,sr^{-1}\,(cm^{-1})^{-1}}$ respectively, and for a spectral resolution reduced by 1/4, the NESR for the S6 observing mode, $\epsilon_{S6}$, is $\epsilon_N/\sqrt{4}$ (i.e. 25 and 20 $\mathrm{nW\,cm^{-2}\,sr^{-1}\,(cm^{-1})^{-1}}$, respectively) (V. Jay, personal communication).

### Vertical resolution

Figure 7.18 shows the averaging kernels calculated for the first 10 microwindows selected for a retrieval on simulated measurements utilising the MIPAS special observing mode S6. The left-hand plots shows the averaging kernels for a 1 km retrieval grid, and the peaks of the averaging kernels have values between 0.5 and 0.6 on all retrieval levels. This indicates that it may be possible to retrieve information with a 1 km vertical resolution although with a reduced retrieval sensitivity. The right-hand plot shows the averaging kernels for the 2 km retrieval grid, which all have peak values of 1.0 at the tangent altitudes.

### Error profiles

Figure 7.19 shows the *a priori*, smoothing, noise and random error profiles for the first 10 microwindows selected for the 6 to 24 km altitude range. The horizontal spacing of limb scans in the S6 observing mode is lower than for the nominal ob-

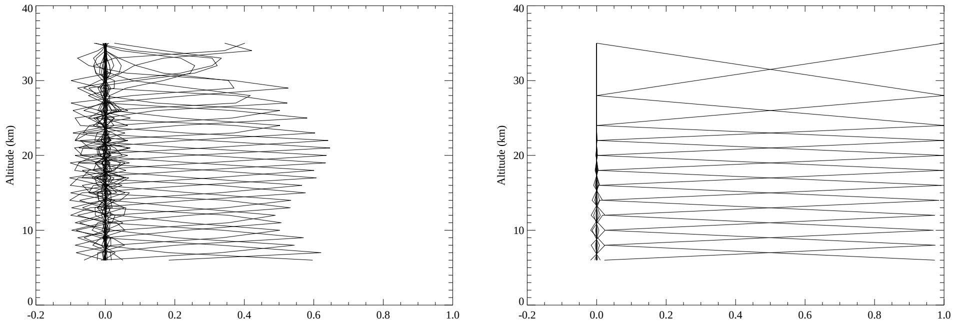

Figure 7.18: Averaging kernels for the first 10 selected microwindows in the UTLS, for the UTLS special observing mode. The left-hand plot shows averaging kernels calculated on a 1 km retrieval grid and the right-hand plot shows averaging kernels calculated on the MIPAS S6 scan pattern retrieval grid.

serving mode due to the reduced spectral resolution and a smaller range of tangent altitudes with a smaller vertical spacing (35, 28 and 24 to 6 km in 2 km steps). The retrieved random errors are not quite as low as in the nominal observing mode, but are still around 10%.

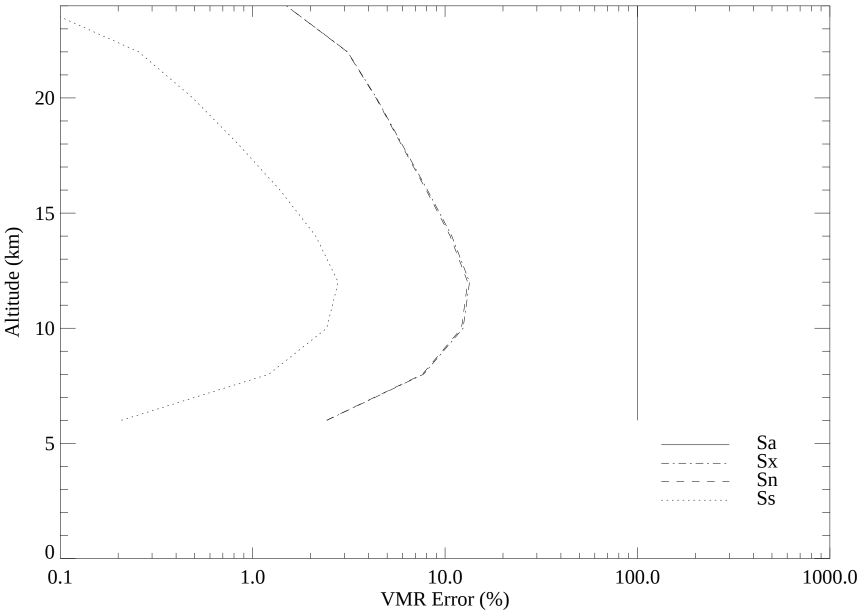

Figure 7.19: Error profiles for the first 10 microwindows selected in the lower atmosphere retrieved for the MIPAS special observing mode S6. The solid, dot-dash, dashed and dotted lines represent the a priori (Sa), random (Sx), noise (Sn) and smoothing (Ss) errors, respectively. Note that the random and noise errors are superimposed.

## 7.5 Discussion

### 7.5.1 Broadband absorption

The microwindow selection procedure described above is based on the analysis of the information content of each microwindow based on the retrieval random error. Microwindows have been selected for an ozone only atmosphere and for an atmosphere containing ozone plus other significant line absorbing gases. Atmospheric trace gases with broad spectral features (e.g. CFCs) are not modelled in the FM2D, and to quantify the effect they may have on the computed weighting functions and, hence, the error covariance and information content, a similar analysis to that described above is performed for Jacobian spectra calculated with the RFM. The upper plot in Figure 7.20 shows the information spectrum for MIPAS bands A and AB calculated using the RFM weighting functions. The black line in this plot is the information spectrum for the ozone only atmosphere, and the red line is the information spectrum for an atmosphere containing ozone and the most significant CFCs in the two bands. In band A the CFCs included in the weighting function calculations are F11, F22 and F113, and the CFCs in band AB are F11, F12, F22 and F113. The lower plot in Figure 7.20 shows the difference between the two information spectra. It is important to note that there are differences in the information spectra calculated for the RFM and FM2D weighting functions, and these are due to differences in the setup, namely the monochromatic grid, in the two calculations. In the RFM, the monochromatic grid is ‘hard-wired’ to a value of 0.0005 cm$^{-1}$ whereas the monochromatic grid for the FM2D weighting functions presented here has a spacing of 0.002 cm$^{-1}$, as described above. However, the Figure 7.20 shows that the impact of CFCs on the information content across the MIPAS bands is restricted to specific spectral regions and the information content in these spectral regions is reduced only modestly.

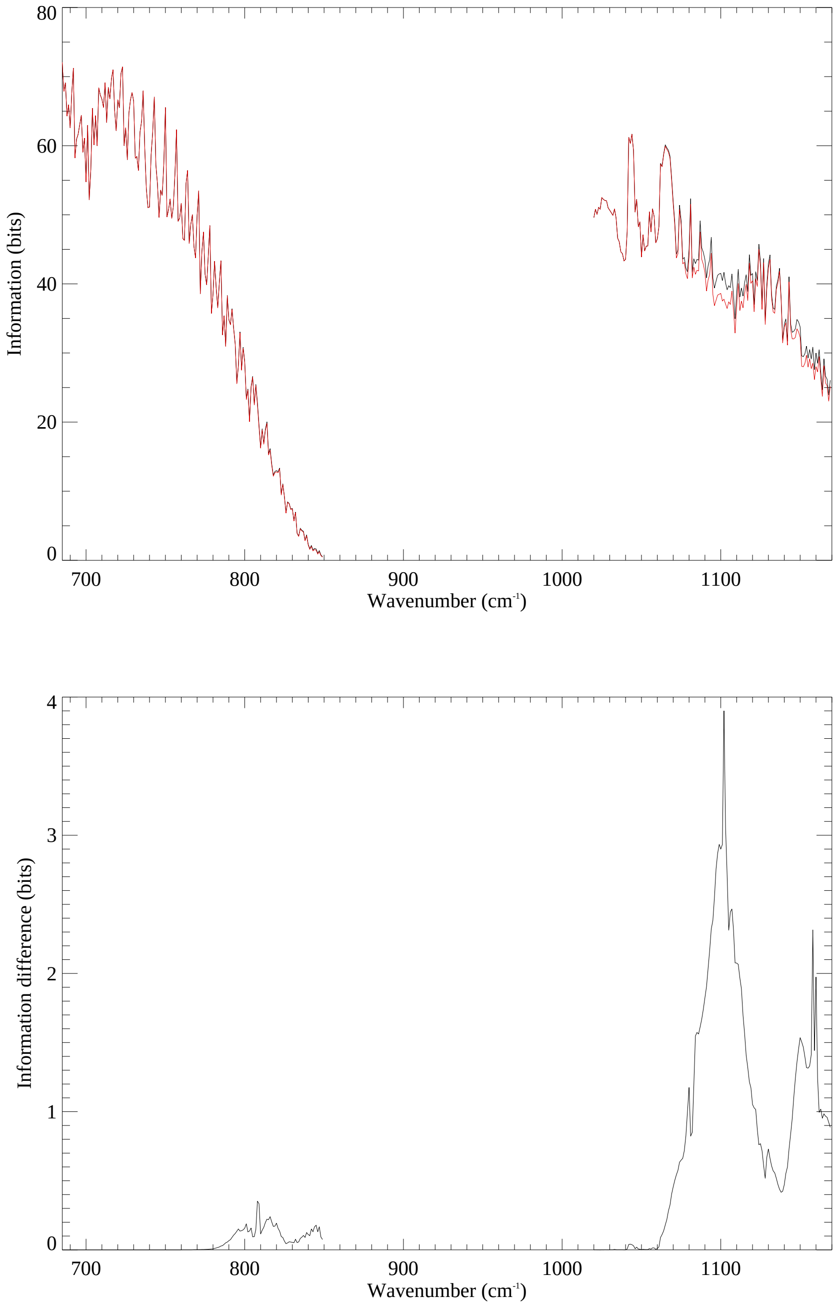

Figure 7.20: Total information spectra (top plot) calculated from RFM computed weighting functions for an ozone only atmosphere (black line) and ozone and CFC atmosphere (red line). The bottom plot shows the difference between the two spectra.

### 7.5.2 Summary

The aim of this chapter has been to assess from linear diagnostics the capability for 1-D linear retrievals of ozone in the upper troposphere and lower stratosphere, using the FM2D forward model, for a simulated mid-latitude daytime atmosphere. Weighting functions were computed with the FM2D for 1 $\text{cm}^{-1}$ wide spectral regions, known as microwindows, in MIPAS bands A and AB (685 to 850 $\text{cm}^{-1}$ and 1020 to 1170 $\text{cm}^{-1}$, respectively). A scheme based on information content was developed to optimize the retrieval for an altitude range restricted to the lower atmosphere (6 to 24 km) for the selection of microwindows. This information content analysis was based on the retrieval random errors only (i.e. the measurement error is the noise equivalent spectral radiance of the measurement) and the most significant systematic error sources were assessed 'post-selection' by the MWMAKE routine. The most significant sources of systematic error, for the microwindows selected, in the UTLS region were generally temperature, water vapour and horizontal structure in temperature along the instrument line-of-sight.

Microwindows were selected for two atmospheres: an atmosphere containing ozone only, and an atmosphere containing ozone and some of the most significant line absorbers (i.e. $\mathrm{CO_2}$, $\mathrm{H_2O}$, $\mathrm{N_2O}$, $\mathrm{NO_2}$, $\mathrm{HNO_3}$ and $\mathrm{CH_4}$). The microwindow selection results for the two atmospheres shows how the selection can change somewhat due to the effect of other absorbers on the computed weighting functions. The line gases chosen for this investigation are not a comprehensive list of the trace species which have spectra in the two MIPAS bands, but are the most important, since their radiance spectra have values which are considerably larger than the NESR in each band. The influence of other absorbers which are not modelled by the FM2D are illustrated in the previous section, using CFCs as an example and found not to be important.

The selection of microwindows from the two MIPAS bands, individually and in combination, has been assessed by comparing the best possible error profiles (i.e. including all of the potential microwindows in the retrieval) to the first 10, 20 and 50 selected and the microwindows selected for the operational processor. Figure 7.14 shows that the random error profile for the first 10 1 $\text{cm}^{-1}$ microwindows selected from MIPAS bands A and AB is lower than the 12 FM2D microwindows covering the operational subset, and these are the microwindows used in the analysis of the ozone retrieval diagnostics.

The effect of systematic errors on the retrieval are removed if those parameters are also retrieved, and the retrieval of the line-of-sight gradient is the focus of the next chapter.

To assess the potential vertical resolution that can be achieved using this scheme, averaging kernels were calculated on two retrieval grids: a 1 km retrieval grid and that of the MIPAS scan pattern. For the nominal scan pattern, it is clear that a vertical resolution of 1 km will not be achievable as the averaging kernel peak values at retrieval levels intermediate to the tangent altitudes are approximately 0.4 (compared to values of between 0.5 and 0.7 at the tangent altitudes). Retrieval diagnostics were also calculated for the MIPAS special observing mode S6 which has a scan pattern with higher vertical sampling (2 km compared to 3 km nominal) in the UTLS region and much higher horizontal sampling. For this special observing mode, the possibility to retrieve at 1 km vertical resolution may be worth attempting as the averaging kernels do peak at each retrieval level, although only with values of between 0.5 and 0.6. This particular special mode was chosen, as opposed to the other possible modes, due to the increased horizontal sampling of the profiles, which may make it possible to retrieve information along the instrument line-of-sight. This exciting possibility is the subject of the next chapter.

# Chapter 8

# MIPAS 2-D Retrievals

## 8.1 Introduction

In the previous chapter it was shown that one of the most significant sources of systematic error, in the retrieval of ozone in the lower atmosphere, is the effect of ignoring a 1 K/100 km horizontal gradient in temperature (the GRA error in Figure 7.15). A retrieval scheme capable of dealing with horizontal gradients along the instrument line-of-sight would, therefore, provide more accurate retrievals of geophysical parameters.

Horizontal variability of the atmosphere occurs due to a number of physical and chemical processes, for example at the edge of the winter polar vortex and photochemistry at the day-night terminator. Typical magnitudes of horizontal gradients in temperature, pressure and trace gas vmr have been assessed by Dudhia (1999a) as part of an ESA study into the retrieval of atmospheric trace gas profiles from infrared spectra. A typical magnitude for temperature is given above, and in the lower atmosphere (9 to 24 km), horizontal gradients in pressure of 1 to 3% and ozone of 10 to 50% per 100 km are fairly typical.

In this chapter, some of the approaches to performing 2-D retrievals from limb sounder data, are briefly discussed, and retrieval simulations for the MIPAS instrument using the RAL FM2D radiative transfer model and 2-D retrieval model are presented.

It is important to note at this stage, that there are two possible approaches to the retrieval of horizontal gradients. One approach that can be applied to measurements from FTS instruments, such as MIPAS, is to use microwindows which can ’view’ to different altitudes in the atmosphere. This approach utilises the same principles applied to the selection of microwindows optimised for the UTLS, presented in the previous chapter, as information comes from different along-track distances (in this case) at different frequencies. The other approach is to perform tomographic 2-D retrievals which utilise information from more than one measured profile to retrieve horizontal structure. The results presented in this chapter are derived with the tomographic approach.

### 8.1.1 2-D retrieval studies

In recent years there have been a number of simulation studies of 2-D retrievals from limb sounder data, some of which are briefly outlined here for comparison purposes.

#### MASTER

The 2-D retrievals from MIPAS simulations, discussed later in this chapter, are based on the retrieval code written for the MASTER study. The Millimetre-wave Acquisitions for Stratosphere-Troposphere Exchange Research (MASTER) study was a study into a possible future microwave limb sounding instrument funded by the European Space Research and Technology Center (ESTEC). The MAS-

TER instrument is a heterodyne spectrometer which observes the limb in five millimetre- and sub-millimetre-wave bands (centred at 202, 300, 320, 345 and 500 GHz). The instrument scans downward through the atmosphere from 33 to 3 km in the polar regions and 40 to 10 km in the tropics with a vertical spacing between limb views of 1 km. Vertical profiles are measured every 15 s leading to a horizontal spacing between profiles of approximately 100 km. The 2-D retrieval study for MASTER discovered that, for ozone, it was possible to perform 2-D retrievals down to approximately 15 km with a horizontal resolution of 80 km achievable between 20 and 25 km altitude (Siddans et al., 2000b).

**MIPAS**

The MIPAS instrument and limb scanning geometry is described in chapter 3. In the nominal observing mode (68 to 6 km in roughly 3 km intervals), vertical profiles are measured approximately every 75 s which leads to a horizontal spacing between profiles of approximately 510 km. Studies of 2-D retrievals from, simulated, MIPAS data have been performed using the Geo-fit method (Carlotti et al., 2001) and the IMK KOPRA radiative transfer model (Kemnitzer et al., 2002). The geo-fit approach simultaneously fits all of the observations from one complete orbit allowing full use of the information that each observation contributes to the line-of-sight. The study into utilising this approach to MIPAS observations discussed in Carlotti et al. (2001) showed that the accuracy of the retrievals are consistent with the uncertainty due to spectral noise and is not correlated with the horizontal variability of the atmosphere (i.e. systematic errors due to atmospheric variability are eliminated). The study also showed that approximately 50% of the retrieval error due to assuming a horizontally homogeneous atmosphere is due to the assumption of horizontal homogeneity with respect to temperature and pressure, which is important as the accuracy of temperature and pressure retrievals are critical to providing accurate retrievals of other parameters (i.e. vmr). The IMK approach models horizontal gradients by comparing microwindows with distinct distance-dependent radiance contributions along the line-of-sight (i.e. saturation in one microwindow is reached due to atmospheric conditions close to the satellite, with another microwindow providing information originating further along the instrument line-of-sight). Results from the IMK study show that the accuracy of profile retrievals is improved if horizontal gradients are included.

### AMIPAS

The Advanced Michelson Interferometer for Passive Atmospheric Sounding (AMIPAS) is a proposed FTS which will measure limb spectra in the 5.7 to 14.2 $\mu$m wavelength range. The instrument is a detector array, allowing a complete scan of the atmospheric limb to be performed in the integration time for one complete sweep of the spectrum. Linear 2-D retrievals have been simulated for the AMIPAS instrument as part of an ESA study into limb sounder observations in the UTLS. The approach adopted for the AMIPAS retrieval simulations is to assume a rectangular retrieval grid with 1 km vertical spacing, and 20 km horizontal spacing between profiles. The observation tangent points coincide with the retrieval grid. For each profile affecting a tangent path through the lowest level, the corresponding component of the full weighting function matrix is computed, and the retrieval error covariance calculated. This component retrieval error covariance matrix is then inserted into the full covariance matrix.

### EOS MLS

The Microwave Limb Sounder (MLS) instrument on the EOS Aura satellite will make observations of the limb at 205 and 240 GHz (for ozone) at a vertical resolution of 2 to 3 km and with a horizontal spacing between profiles of 165 km. More details on the EOS MLS instrument are given in Waters et al. (1999). The data is processed in 'chunks' of contiguous geophysical profiles, approximately a 1/4 orbit in length, with the state vector defined as a set of $N$ subvectors. The number of scans is typically defined to be equal to $N$. This leads to a relatively sparse $\mathbf{K}$ matrix with a 'block band-diagonal' form as radiances from the first profile will affect the radiances for the first scan, but not the tenth (for example). If the block bandwidth of $\mathbf{K}$ is $p$ (i.e. the number of scans affected by a given profile), then the $\mathbf{K}^T\mathbf{S}_y^{-1}\mathbf{K}$ matrix has a bandwidth of $2p$, assuming that $\mathbf{S}_y$ is diagonal. Simulated results of this 2-D approach to retrievals are shown by Livesey and Read (2000) to be more accurate than the 1-D case. In the ozone channel, the results of the 1-D retrievals tend to lead relative to the truth as the instrument 'sees through' the optically thin atmosphere to regions of higher ozone concentration and the 1-D retrieval ascribes the information to the wrong location.

### EOS TES

The Tropospheric Emission Spectrometer (TES) instrument (Beer et al., 2001), also on the EOS Aura satellite is an imaging infrared Fourier-transform spectrometer which will make observations in nadir and limb viewing modes. TES is a 16 element detector array and one scan of the limb, from 0 to approximately 33 km at 2.3 km vertical resolution, will take 16 s. This provides a horizontal spacing between vertical profiles of approximately 110 km. An approach to 2-D retrievals from TES limb observation data is to construct a state vector of 6 atmospheric profiles separated by $2^\circ$ latitude, and a measurement vector containing 3 limb scans, assumed to be the sum of the forward model evaluated at the true state and noise (Worden et al., 2003). Comparison of the degrees of freedom for signal and information content calculated for a 1-D and 2-D retrieval are shown to be significantly larger for the 2-D retrieval.

### 8.1.2 MIPAS observing modes

The challenge for performing 2-D retrievals from the MIPAS data is to measure frequently enough to provide substantial information to determine the horizontal structure along the instrument line-of-sight. Figure 8.1 shows the tangent path geometry for five consecutive limb scans utilising the MIPAS nominal observing mode. Tangent paths are plotted for successive scans and show that limb views from successive scans intersect at 10 km with the lowest altitude at which limb views from one limb view intersect the next measured profile being 20 km. In this way, the horizontal structure can be considered to be under-sampled, so we would not expect it to be possible to retrieve information on ozone, especially in the lower atmosphere, in 2-D with this scan pattern. As described in previous chapters, the MIPAS instrument has a number of special observing modes which utilise a combination of different measurement spacings (horizontal and vertical)

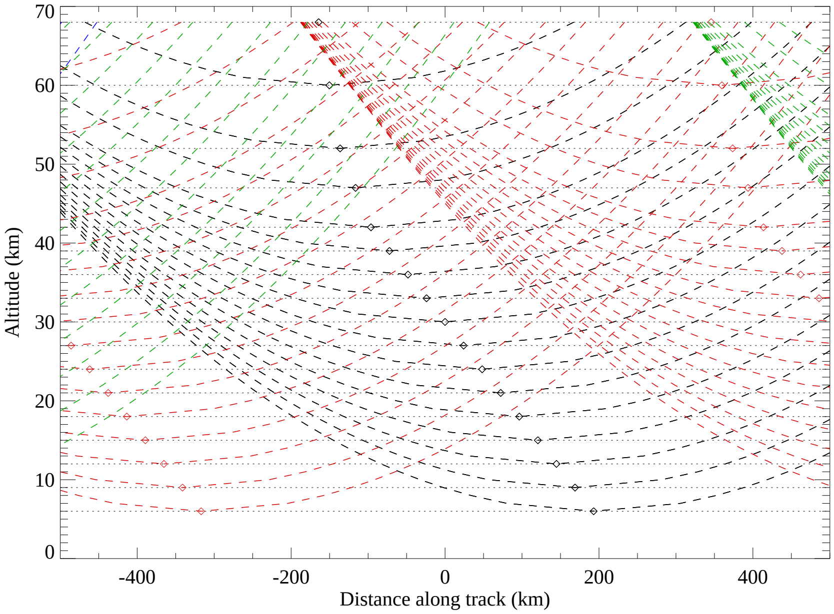

Figure 8.1: Tangent path geometry for the MIPAS nominal scan pattern. The dashed line shows the tangent path through the atmosphere, the dotted line represents the retrieval levels, and the diamonds show the tangent points.

and spectral resolutions. In chapter 7, 1-D retrieval simulations were performed for the S6 observing mode, with a view to exploiting it in a 2-D retrieval scheme. The S6 observing mode scans the limb at a much reduced (by a factor of four) spectral resolution relative to the nominal observing mode (0.1 cm$^{-1}$ compared to 0.025 cm$^{-1}$) over a reduced vertical range, and with a vertical spacing between limb measurements of 2 km. This leads to a horizontal spacing between subsequent limb scans of approximately 116 km (compared to approximately 510 km in the nominal observing mode). Figure 8.2 show the tangent path geometry for the S6 observing mode. In this case the tangent path for the lowest limb view will intersect ten other limb scans. The horizontal structure is now oversampled, so it should be possible to perform 2-D retrievals in this mode.

## 8.2 Retrieval Scheme

The main purpose of the retrieval simulations presented in this chapter is to determine the potential for performing 2-D retrievals for the MIPAS instrument operating in the nominal and S6 observing modes. These retrieval simulations were performed with the RAL 2-D retrieval model, developed originally for the MASTER study and now adapted for application to MIPAS. Retrieval simulations are performed for the 10 microwindows selected for the 6 to 24 km altitude range in the previous chapter (see Table 7.2).

As for the 1-D retrieval simulations, the most useful retrieval diagnostics are the retrieval error covariance and averaging kernel matrices (equations (7.1) and (7.2)), both of which require the Fisher information matrix: $\mathbf{K}^T\mathbf{S}_y^{-1}\mathbf{K}$. For a 2-D retrieval, the number of measurements ($N_y$) is considerably larger than for

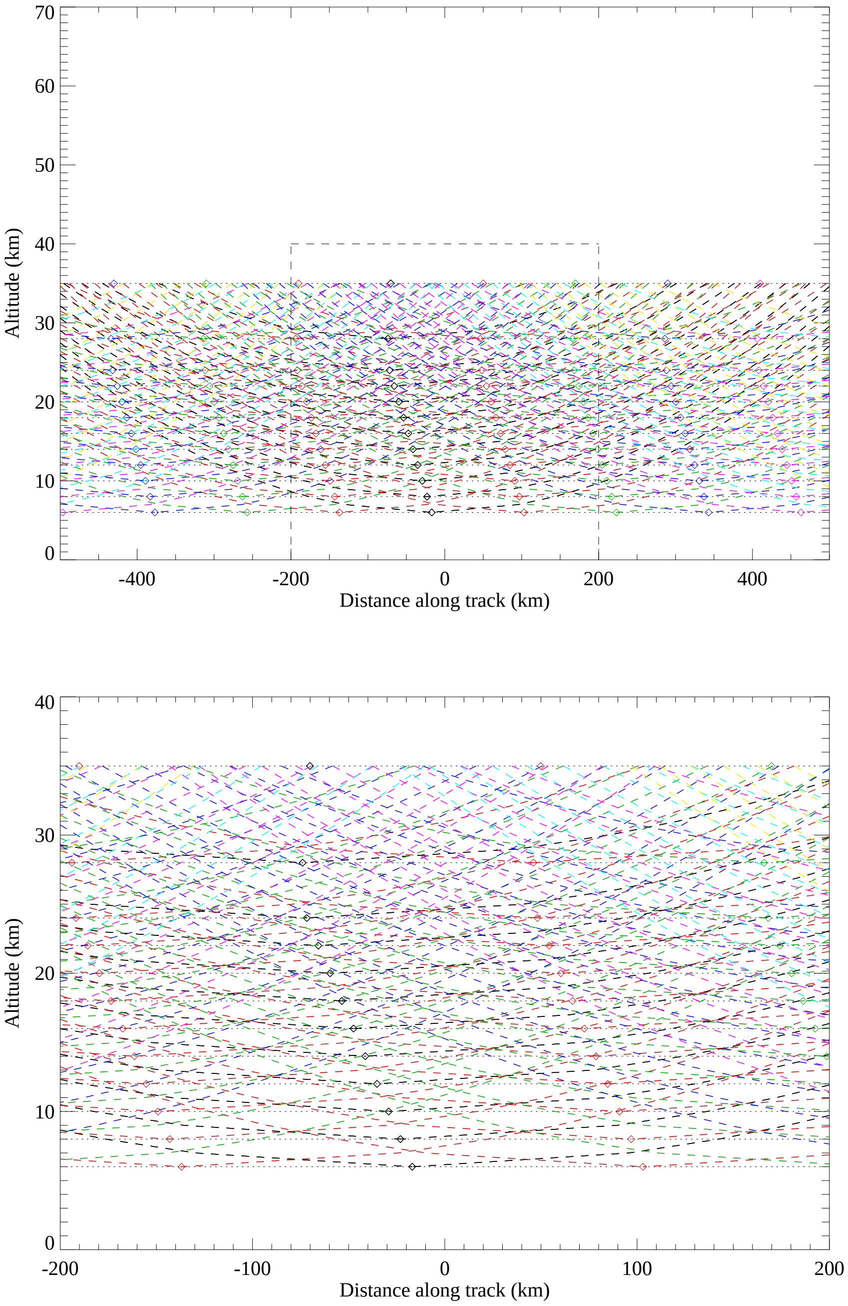

Figure 8.2: Tangent path geometry for the scan pattern utilised by the MIPAS special observing mode S6 (upper plot). The dashed line shows the tangent path through the atmosphere, the dotted line represents the retrieval levels, and the diamonds show the tangent points. The tangent paths that pass through the area defined by the dashed black line are shown in close-up in the lower plot.

a 1-D retrieval, which leads to the computational problem of having to store a potentially huge weighting function matrix. In the RAL retrieval model, after the state vector has been constructed (see below), a set of limb views are defined from which the linear retrieval diagnostics can be estimated. These limb views consist of $N_y$ spectral points at $N_{\text{view}}$ tangent views for $N_{\text{scan}}$ scan sequences. The forward model is then used to compute weighting functions, and $\mathbf{K}^T\mathbf{S}_y^{-1}\mathbf{K}$, for one limb view at a time (convolving a set of instantaneous pencil beam views defined relative to the required tangent point). By assuming that the noise error covariance matrix $\mathbf{S}_y$ is diagonal, $\mathbf{K}^T\mathbf{S}_y^{-1}\mathbf{K}$ is then accumulated for each tangent view at a time as in equation (7.3), where $i$ now represents the current tangent view. The retrieval code cycles through each tangent view and scan sequence until all $\mathbf{K}^T\mathbf{S}_y^{-1}\mathbf{K}$s have been accumulated.

### 8.2.1 2-D retrieval grid

The state vector and retrieval grid for the RAL 2-D retrieval model are determined by the scan pattern of the measurements. In the vertical domain, the retrieval grid is based on the S6 scan pattern (i.e. 2 km), with extra levels above and below to take account of radiative transfer through the atmosphere outside the measurement range, and to cover the instrument FOV at the top and bottom measurement levels.

To reduce memory and CPU requirements, the state vector is defined artificially to be *cyclic* in the horizontal domain. The horizontal retrieval grid is determined in such a way that it extends over at least the horizontal distance travelled by a limb line-of-sight with a tangent altitude of 0 km and top of atmosphere at 70 km (i.e. at least 1700 km). Retrieval simulations are performed for a sequence of limb scans which span this section, starting from the centre of the horizontal cross-section. The cyclic state vector allows any limb lines-of-sight that extend outside the edge of the horizontal section to re-emerge at the opposite end. The state vector grid is constructed to precisely coincide, or differ, by an integral number of tangent point spacings between successive limb scans. The horizontal extent of the section is then such that re-emerging limb views will eventually perfectly overlap with the first limb view. As the $\mathbf{K}^T\mathbf{S}_y^{-1}\mathbf{K}$ matrix is accumulated for one complete cycle of limb views, each block in the matrix corresponds to blocks from the ideal matrix constructed using an infinite number of limb scans over an infinite horizontal extent.

Figure 8.3 shows the geometry of a 2-D state vector constructed for a retrieval utilising the MIPAS observing mode S6. The tangent paths of each limb view is represented by a green line, and the dotted horizontal and vertical lines represent the 2-D retrieval grid. The upper plot shows limb views for the first six limb scans, and the thick black lines illustrate how limb views exiting the horizontal section re-emerge at the opposite end. The lower plot shows the geometry for all 20 limb scans used in the retrieval and illustrates the density of sampling for this pattern.

### 8.2.2 2-D linear diagnostics

The retrieval error covariance and averaging kernel matrices are calculated, separately from the retrieval scheme, for the accumulated $\mathbf{K}^T\mathbf{S}_y^{-1}\mathbf{K}$. The size of the $\mathbf{K}^T\mathbf{S}_y^{-1}\mathbf{K}$ (also $\mathbf{S}_x$ and $\mathbf{A}$) matrix is $N_x \times N_x$, as before, where $N_x$ is now $N_{\text{scan}} \times N_{\text{view}}$ since each state vector element corresponds to a scan sequence and tangent view. Therefore $N_x$ is considerably larger than in 1-D, and to conserve computer memory, the diagnostic code first calculates $\mathbf{S}_x$ and overwrites the stored $\mathbf{K}^T\mathbf{S}_y^{-1}\mathbf{K}$. After the diagonal elements of $\mathbf{S}_x$ have been saved, $\mathbf{A}$ is calculated and overwrites $\mathbf{S}_x$.

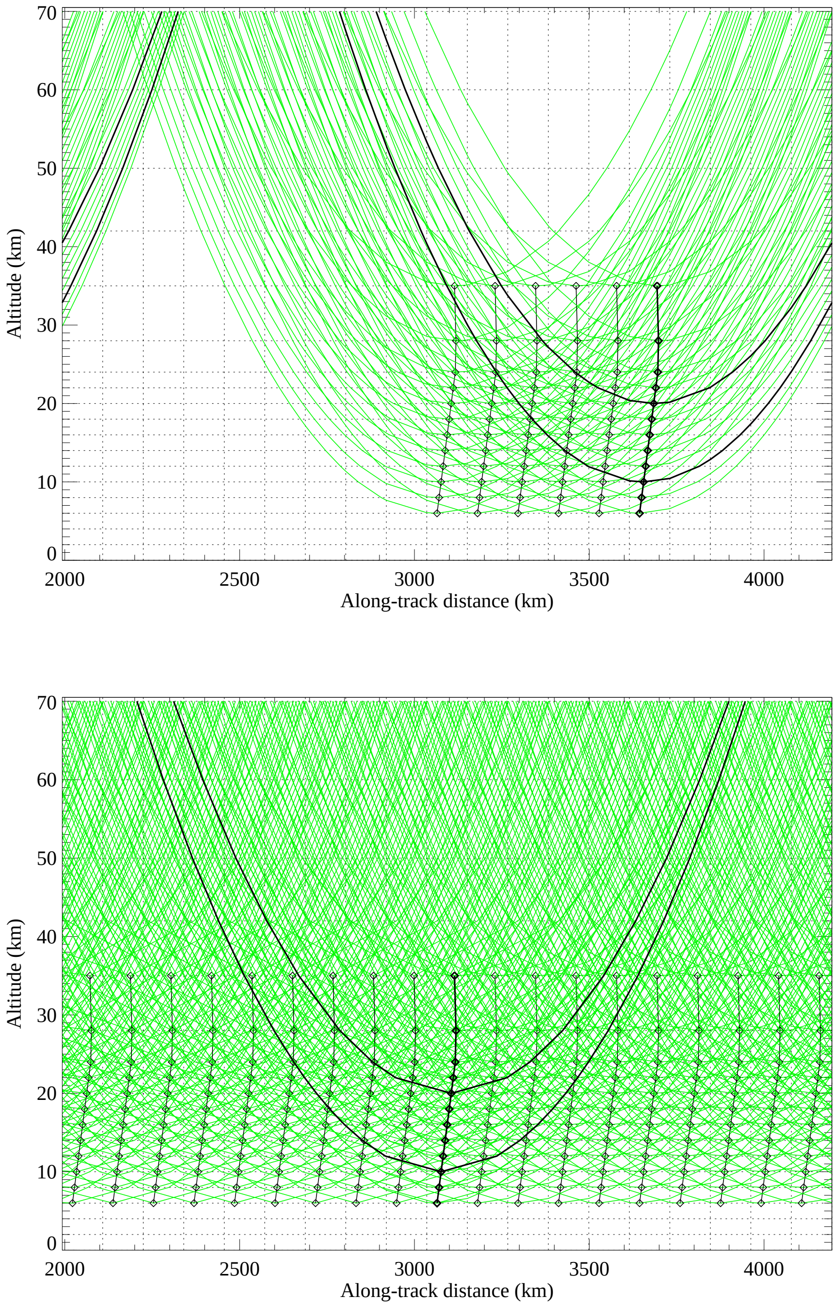

Figure 8.3: Geometry of the 2-D retrieval grid The upper and lower plots show the tangent paths of the first 6 scans and all scans, respectively. The vertical and horizontal retrieval grids are represented by the dotted lines, the diamonds show the tangent points and their loci are shown by the thin black lines. The thick black lines show how tangent paths at the edge of the 2-D cross-section re-emerge at the other side.

As the 2-D atmosphere, for this purpose, is constructed to be horizontally homogeneous, the retrieval diagnostics will also be homogeneous across the horizontal section. To avoid possible edge effects, the retrieval diagnostics are presented for the horizontal mid-point. The retrieval diagnostics presented are:

- Percentage error - the square root of the diagonal elements of the retrieval error covariance matrix at the horizontal mid-point.

- Averaging kernel peak values - the value of the averaging kernel at each retrieval level at the horizontal mid-point. The value of a 2-D averaging kernel at the $i^{\mathrm{th}}$ horizontal grid point and $j^{\mathrm{th}}$ vertical grid point is the partial derivative of the estimated state vector element ($i$,$j$) with respect to the true state vector element ($l$,$m$) (at the $l^{\mathrm{th}}$ horizontal grid point and $m^{\mathrm{th}}$ vertical grid point):

  $$A_{lm}^{ij} = \frac{\partial \hat{x}_{ij}}{\partial x_{lm}} \tag{8.1}$$

  the averaging kernel peak values should occur at $i = l$ and $j = m$.

- Vertical resolution - the full width half maxima of each averaging kernel summed over all horizontal grid points. The $m^{\mathrm{th}}$ element (for each vertical grid point) of the calculated vector is given by

  $$v_m^{ij} = \sum_l \frac{\partial \hat{x}_{ij}}{\partial x_{lm}} \tag{8.2}$$

- Horizontal resolution - the full width half maximum of each averaging kernel summed over all vertical grid points. The $l^{\mathrm{th}}$ element (for each horizontal grid point) of the calculated vector is given by

  $$h_l^{ij} = \sum_m \frac{\partial \hat{x}_{ij}}{\partial x_{lm}} \tag{8.3}$$

## 8.3 Linear Retrieval Simulations

Linear retrieval diagnostics have been calculated for simulated 2-D ozone retrievals for the nominal and S6 MIPAS observing modes for the 10 microwindows selected in the previous chapter (see Table 7.2). For these simulations, an ozone-only atmosphere is assumed, and the set-up for the sensor driver is defined as for the 1-D retrieval simulations in chapter 7. The *a priori* error in all of the retrievals presented is assumed to be diagonal and 100% at all levels.

The vertical retrieval grid is defined to coincide with the tangent points in the S6 scan pattern (35, 28 km and 24 to 6 km in 2 km steps) with extra levels at 2 and 4 km (to allow the full FOV convolution at the lowest tangent point) and at 50, 60 and 70 km (to account for radiative transfer through the atmosphere above the measurement range). The horizontal retrieval grid is defined at 20 points (19 scan sequences) extending from 2050 to 4251 km with a nominal grid spacing of 116 km. For comparison purposes, this 2-D retrieval grid is used when performing the retrieval for both MIPAS observing modes.

### 8.3.1 S6 observing mode

The linear 2-D retrieval diagnostics calculated for the S6 MIPAS observing mode are shown in Figure 8.4. Results are shown for retrievals at three different horizontal grid spacings: 116, 232 and 348 km (represented by the solid black, red and green lines, in each plot, respectively). The dashed black line, where it appears, represents the 1-D retrieval diagnostics from chapter 7. The upper left-hand plot shows the percentage retrieval error profiles, and the improvement that can be made over a 1-D retrieval for a horizontal retrieval grid spacing sufficiently oversampled by the measurements. The upper right-hand plot shows the averag-

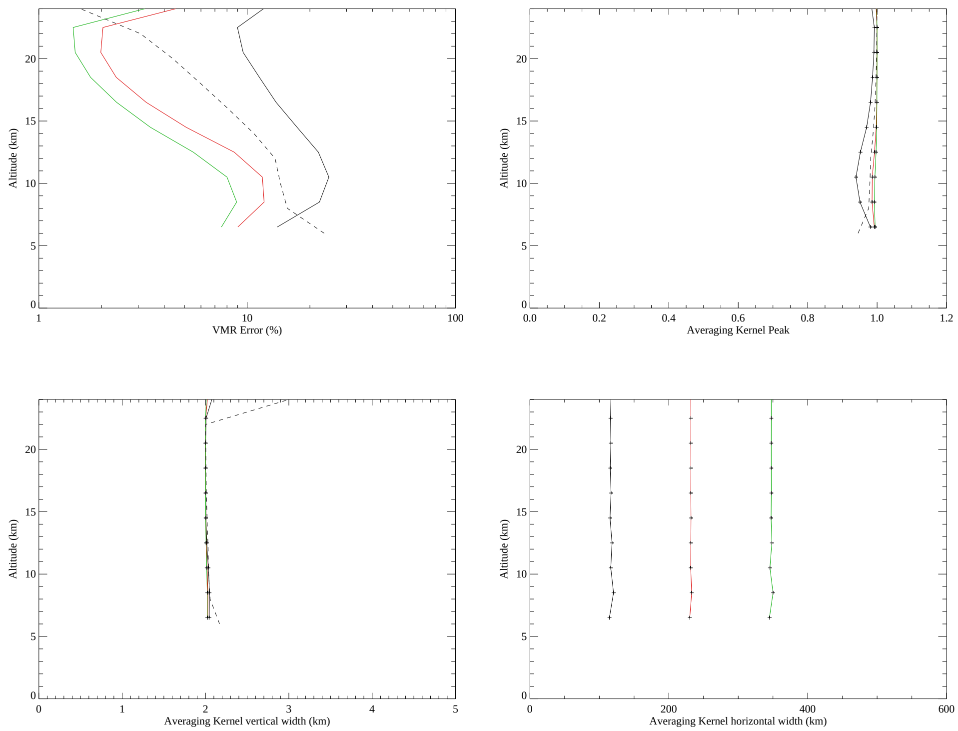

Figure 8.4: Linear 2-D retrieval diagnostics for the MIPAS special observing mode S6. In each plot, the black, red and green lines represent horizontal retrieval grid spacings of 116, 232 and 348 km respectively. The dashed black line shows results for the 1-D retrieval scheme from the previous chapter.

ing kernel peak values, which have values of approximately 1 in each case. The lower left-hand plot shows the vertical full width half maxima of the averaging kernels, which are mostly equal to the vertical spacing of the observations. The lower right-hand plot shows the horizontal full width half maxima of the averaging kernels, all of which are equal to the corresponding horizontal retrieval grid spacing.

### 8.3.2 Nominal observing mode

The linear 2-D retrieval diagnostics calculated for the nominal MIPAS observing mode are shown in Figure 8.5. In this case, results are shown for horizontal retrieval grid spacings of 116, 232, 348, 464 and 560 km and represented in each plot by the solid black, red, green, blue and pink lines respectively. As above, the dashed black line represents the 1-D diagnostics from the previous chapter. As expected, the horizontal distance between successive limb scans in the nominal observing mode is too large to be able to perform 2-D retrievals. The best results are for the 560 km horizontal grid spacing (i.e. roughly the horizontal distance between successive limb scans), although the precision is approximately a factor of 4 worse in error than the equivalent 1-D retrieval.

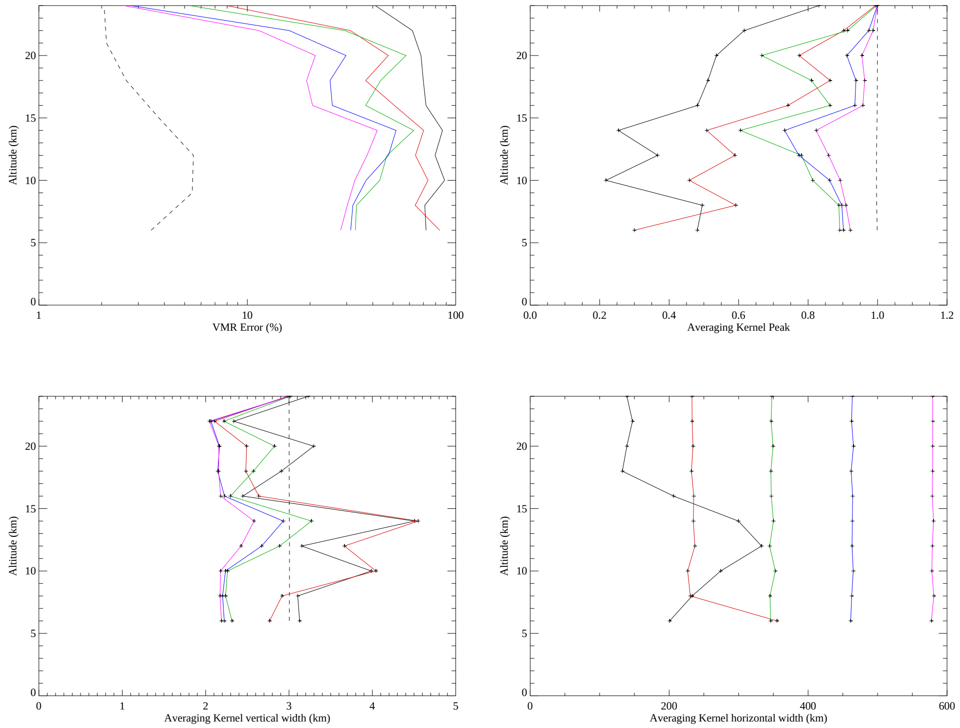

Figure 8.5: Linear 2-D retrieval diagnostics for the nominal MIPAS observing mode. In each plot, the black, red, green, blue and pink lines represent horizontal retrieval grid spacings of 116, 232, 348, 464 and 580 km respectively.

## 8.3.3 Comparison to 1-D retrievals

The above figures show how the linear retrieval diagnostics for the 2-D and 1-D retrieval schemes compare to each other. Figure 8.4 shows how the performance of the 2-D retrieval improves as the spacing of the horizontal retrieval grid is increased. The percentage retrieval error profiles show that for a horizontal retrieval grid spacing equal to the spacing between vertical profiles, the 2-D retrieval does not perform as well as the 1-D retrieval, with errors approximately a factor 2 greater than in 1-D. However, if the spacing of the horizontal retrieval grid is doubled (the red line in the figure), the errors in the 2-D retrieval are reduced. Although the 2-D retrieval errors in the nominal observing mode also improve as the horizontal grid spacing is increased, they are still approximately a factor 5 larger than for the 1-D retrieval.

Table 8.1 shows the information content of each of the ten microwindows (individually and in combination), for the 1-D retrieval and the 2-D retrieval, in the S6 observing mode, at horizontal retrieval grid spacings of 116 and 232 km. The value of the information content reflects the changes in the error profiles for the different horizontal grid spacing compared to the 1-D.

| Microwindow | 1-D | 2-D (116 km) | 2-D (232 km) |
|---|---|---|---|
| 764 | 34.58 | 26.60 | 50.94 |
| 1067 | 30.24 | 30.85 | 53.19 |
| 750 | 32.14 | 31.73 | 58.89 |
| 1069 | 29.35 | 27.39 | 49.51 |
| 757 | 30.45 | 28.62 | 55.44 |
| 760 | 31.89 | 25.38 | 46.66 |
| 771 | 33.03 | 25.87 | 49.25 |
| 765 | 31.95 | 22.71 | 40.76 |
| 759 | 29.99 | 23.17 | 41.81 |
| 743 | 25.01 | 30.03 | 55.37 |
| All | 59.88 | 57.63 | 85.37 |

Table 8.1: Information content in bits for the first ten selected microwindows for the 1-D and 2-D retrieval schemes and the S6 observing mode.

### 8.3.4 Vertical resolution

The averaging kernel widths in Figure 8.4 appear to be determined by the spacing of retrieval levels, indicating that it may be possible to retrieve at a finer vertical resolution for the S6 observing mode. The averaging kernels at 1 km vertical resolution for the 1-D retrieval simulations, shown in the left-hand plot of Figure 7.18, all peak at the retrieval level although the peak values are only between 0.5 and 0.6. The figures above demonstrate how the sensitivity of a 2-D retrieval scheme can actually be better than that of a 1-D retrieval scheme if the horizontal retrieval grid spacing is sufficiently large. To assess the potential for retrieving information at 1 km vertical resolution, 2-D retrieval simulations were performed for the S6 observing mode on a 1 km vertical retrieval grid.

The linear 2-D retrieval diagnostics for this simulation are shown in Figure 8.6. As in Figure 8.4, results are shown for horizontal retrieval grid spacings of 116, 232 and 348 km (represented by the solid black, red and green lines, in each plot, respectively), and the dashed black line represents the 1-D retrieval diagnostics from chapter 7. In the 1-D retrieval scheme, the percentage errors are greater than 60% at most levels, and this can be reduced to between approximately 30 and 50% for the 2-D retrieval scheme with a horizontal retrieval grid spacing of 348 km. It would appear that the optimum altitudes for retrieving ozone with a 1 km vertical resolution in this way are between 15 to 24 km where the averaging kernels peak between 0.9 and 0.95.

It is worth remembering that the measurement spacing is 2 km in the S6 observing mode, and so for a retrieval vertical resolution of greater than 2 km, the spectral information has to be exploited. The ability to achieve a retrieval vertical resolution of better than 2 km would be improved if the limb scanning sequence has

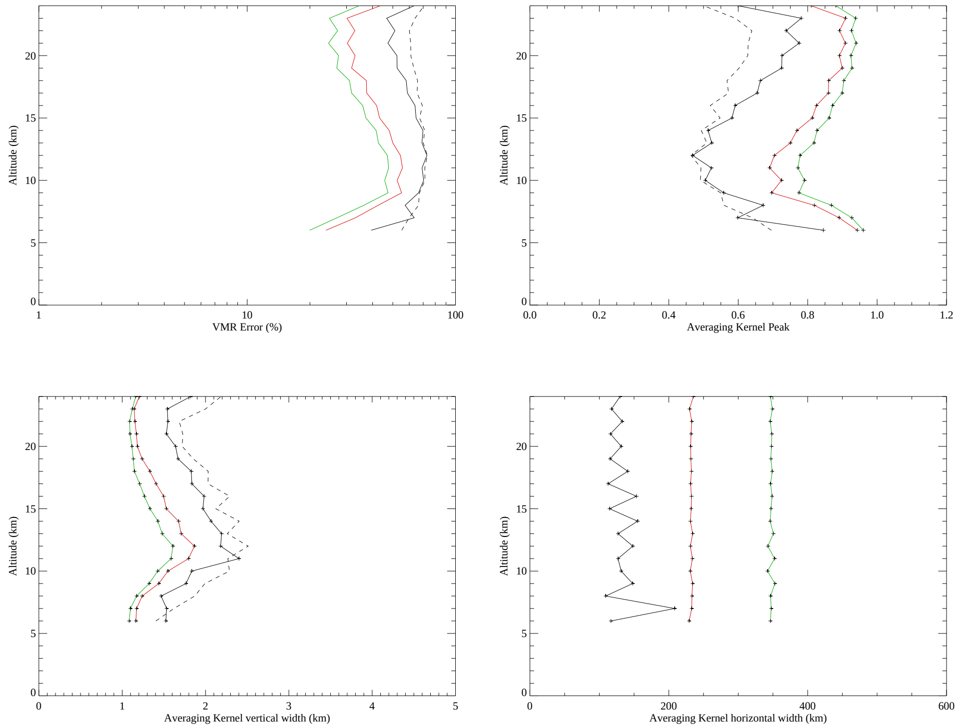

Figure 8.6: Linear 2-D retrieval diagnostics for the MIPAS special observing mode S6. In each plot, the black, red and green lines represent horizontal retrieval grid spacings of 116, 232 and 348 km respectively. The dashed black line shows the results for the 1-D retrieval scheme in the previous chapter.

a 1 km vertical spacing. In practise, however, this would require highly accurate knowledge of the FOV pattern and the pointing of the instrument.

## 8.4 Non-linear Retrieval Simulations

In the previous section the potential for retrieving a 2-D ozone field was assessed through the calculation of diagnostics for a simulated linear retrieval. The capability of a 2-D retrieval may also be assessed through the simulation of a non-linear retrieval based on an atmospheric state containing horizontal structure. The retrieval scheme used to perform these simulations is described in detail by Reburn et al. (1998) and Siddans et al. (2000b).

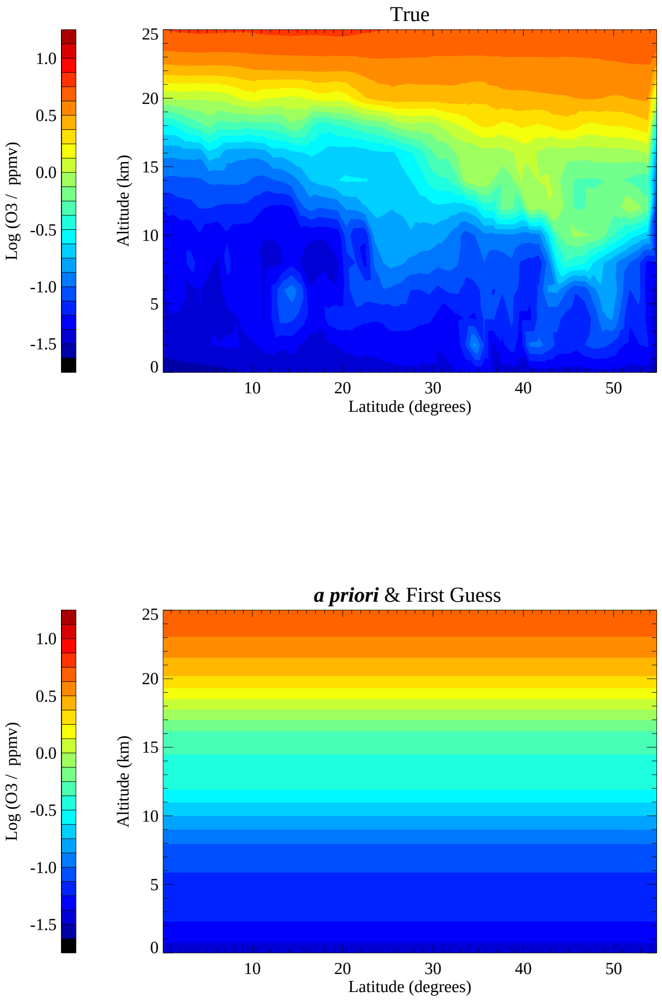

Figure 8.7: 2-D ozone true and *a priori*/first guess cross-sections for the non-linear retrieval simulations presented in this section. The upper plot shows the true field constructed from an ECMWF analysis for April 4 1998, with the *a priori*/first guess field represented by the flat field shown in the lower plot.

Figure 8.7 shows the 2-D ozone cross-sections representing the true (upper plot) and *a priori*/first guess fields for the non-linear retrieval simulations presented here. The true field extends from 0 to 55° N (approximately 6230 km) and was constructed from an ECMWF analysis on April 4 1998 as a retrieval scenario for an ESTEC study into a satellite mission for studying the chemistry of the UTLS (Kerridge et al., 2002). The *a priori* and first guess fields were both a flat field along the horizontal extent of the cross-section (i.e. the same vertical ozone profile is repeated at every point on the horizontal retrieval grid). The *a priori* error covariance matrix is assumed to be diagonal. Simulated measurements for the MIPAS instrument, in the S6 observing mode, were generated for this cross-section with the FM2D radiative transfer model. The horizontal resolution of the cross-section is approximately 1.12° (124 km) and is defined in the vertical from 0 to 50 km at 1 km intervals. Non-linear retrievals were performed for the first selected microwindow in Table 7.2 for the 6 to 24 km altitude range, i.e. 764 $\mathrm{cm}^{-1}$. Retrievals were performed on horizontal retrieval grid spacings based on the horizontal resolution of the cross-section multiplied by factors of 1, 2 and 3 (i.e. horizontal retrieval grid spacings of 1.12, 2.24 and 3.36° or 124, 248 and 372 km)[1]. The vertical retrieval grid is based on the measurement spacings in the S6 scan pattern with extra retrieval levels at 0, 2, 4, 40, 45 and 50 km.

### 8.4.1 Results

Retrieval results for the 1.12, 2.24 and 3.36° horizontal retrieval grid spacings are shown in Figures 8.8, 8.9 and 8.10 respectively. In each figure, the upper two plots show the retrieved ozone field and retrieval error, and the lower two plots show the percentage difference of the retrieved and true fields and the ratio of the estimated retrieval error to the *a priori* error.

For each of the three horizontal retrieval grid spacings, the largest differences between the retrieved and the true fields are below 6 km altitude, which is below the lowest measurement altitude in the S6 observing mode. Structure in the differences below 6 km, i.e. below the lowest measurement altitude, are due to the structure in the true field. Above 6 km and away from the edges of the section

---

[1] Recall that in the previous section horizontal retrieval grid spacing of 116, 232 and 348 km are used.

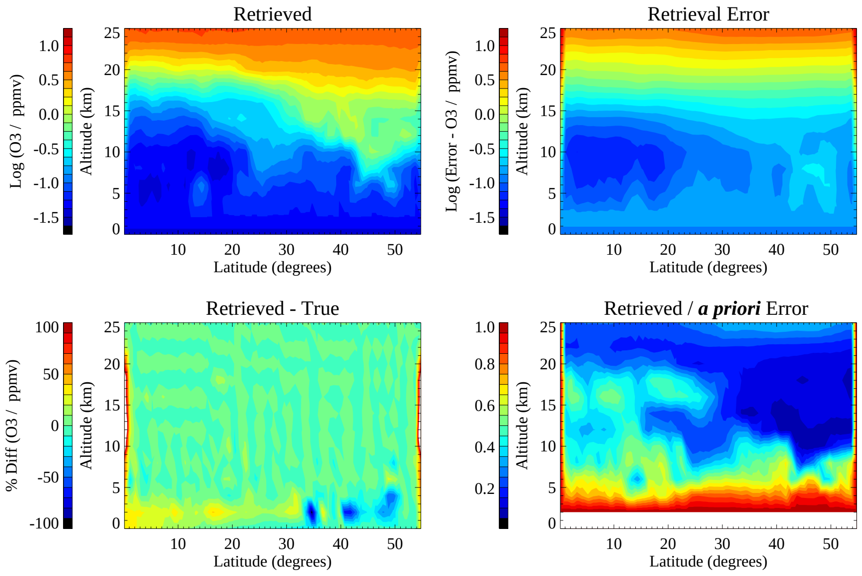

Figure 8.8: 2-D non-linear retrieval results with a horizontal retrieval grid spacing of 1.12° (124 km).

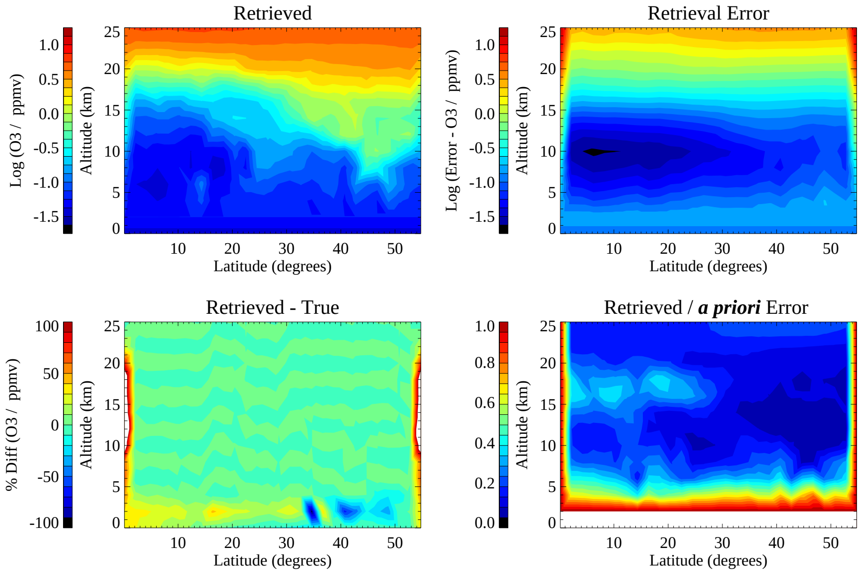

Figure 8.9: 2-D non-linear retrieval results with a horizontal retrieval grid spacing of 2.24° (248 km).

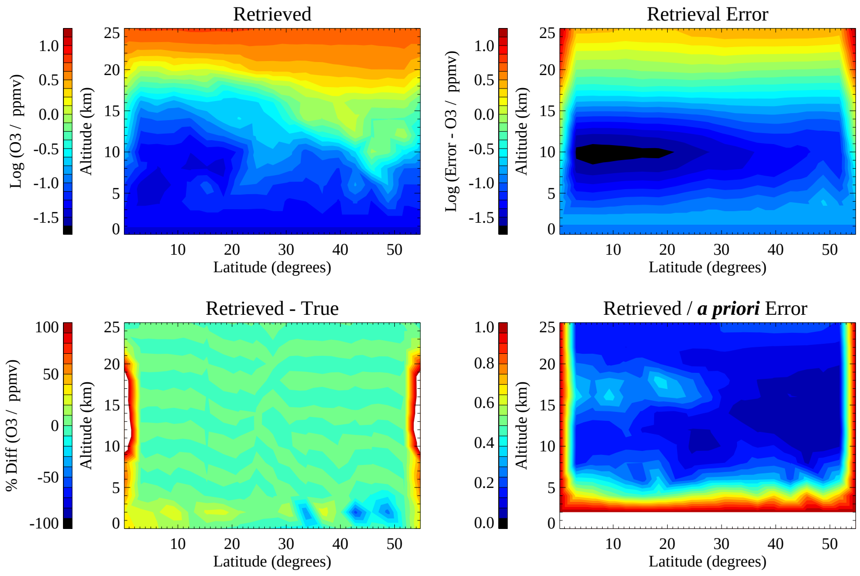

Figure 8.10: 2-D non-linear retrieval results with a horizontal retrieval grid spacing of 3.36° (372 km).

(i.e. not at 0 or 55° N), the retrieved field appears to be within approximately 10 to 15% of the true field indicating that the retrieval is recreating the horizontal structure in the true field.

In Figure 8.8, the retrieval error is relatively high as is reflected in the ratio of the retrieval error to the *a priori* error with values of between approximately 0.5 and 0.65 at latitudes between 0 and 30° N and altitudes between 5 and 20 km (i.e. altitudes and latitudes corresponding to relatively low ozone values in the true field. Between these latitudes, the estimated uncertainties are quite high relative to the rest of the field and compared to the differences between the true and retrieved fields. At other latitudes, the ratio of the retrieved to the *a priori* error appears to be less than 20% and indicate that the retrieval scheme is performing as expected. As shown in the previous section, the retrieval error improves as the horizontal retrieval grid spacing is increased (e.g. Figure 8.4), and this is reflected in Figures 8.9 and 8.10 where the horizontal retrieval grid spacing in each case is increased by a factor of 2 and 3 respectively. In these figures the ratio of the retrieval error to the *a priori* error reaches a maximum value of approximately 0.4 between 0 and 30° N, extending over an altitude range between 15 and 20 km. It is also worth noting that although there is an improvement in the retrieval error between Figures 8.9 and 8.10, it is not as significant as the difference in the retrieval error between Figures 8.8 and 8.9. This is also consistent with the improvement in the retrieval error for the linear retrieval simulations shown in Figure 8.4.

### Effect of continuum

The retrieval results in Figures 8.8, 8.9 and 8.10 are for an ozone only atmosphere with no continuum or other interference included. Figure 8.11 shows the results for a retrieval simulation, performed at the 3.36° horizontal retrieval grid spacing, including continuum. Continuum is included in the state vector as well as the radiative transfer model with the *a priori* and first guess provided by the CKD continuum as in chapter 7, the *a priori* error is taken to be 100% at all levels, as for the ozone.

The percentage difference between the retrieved and the true fields is similar to the results where the effect of continuum has been omitted, with the largest differences below 6 km and at the edges of the cross-section (i.e. close to 0 and 55° N). The retrieval error appears to be slightly worse compared to Figure 8.10, although above 6 km and between 5 and 50° N the magnitude of the ratio of the retrieved to the *a priori* error is approximately the same (0.4) and shows a similar structure.

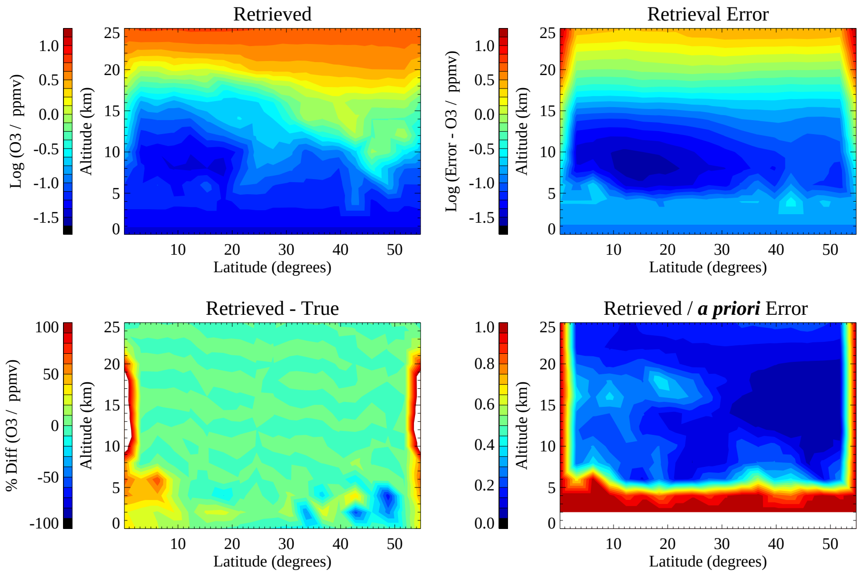

Figure 8.11: 2-D non-linear retrieval results with a horizontal retrieval grid spacing of 3.36° (372 km), including the effects of continuum.

## 8.5 Discussion and Further Work

The ability to perform 2-D retrievals of geophysical parameters from limb sounder data can be beneficial in the following ways:

- the effect of horizontal gradients along the instrument line-of-sight can be removed as a source of systematic error.
- the improvement in precision over a 1-D retrieval, providing a suitable horizontal retrieval grid spacing is used. The improvement in precision is dependent on the ratio of the measurement to the retrieval grid.
- the ability to capture horizontal structure in the ozone field at finer resolution than traditionally thought possible for limb sounding. That is to say, ‘tomographic’ compared to ‘conventional’ limb sounding.

There have been a number of studies in recent years to investigate the potential of 2-D retrievals for current and future instruments (MIPAS, MASTER, EOS MLS and TES, AMIPAS). All of these studies have shown that the assumption of horizontal homogeneity can lead to significant retrieval errors, and improved retrieval accuracy when horizontal gradients are included.

In this chapter, 2-D linear retrieval simulations have been performed with the RAL 2-D retrieval model to provide linear diagnostics for the 10 microwindows selected in chapter 7. Limb scans in the nominal MIPAS observing mode have a horizontal spacing of 510 km, which leads to the horizontal structure being undersampled along the instrument line-of-sight, and is not sufficient for performing 2-D retrievals (as shown in Figure 8.5). The MIPAS special observing mode S6 is able to provide a much shorter horizontal distance (120 km) between subsequent limb scans. The vertical spacing is also reduced compared to the nominal mode (2 km compared to 3 km). This is accomplished by observing the limb from only 6 to 35 km, and at a reduced (by a factor of four) spectral resolution compared to the nominal mode. Linear retrieval diagnostics calculated for this mode (Figure 8.4) show that it may be possible to provide improved precision over a 1-D retrieval, if a horizontal retrieval grid spaced with at least twice the measurement spacing is used. The potential for retrievals at a vertical resolution finer than the 2 km measurement spacing has also been investigated using the 2-D scheme (Figure 8.6), and although improvements in precision can be made over a 1-D retrieval scheme, the lowest percentage error attainable, for the retrieval scheme described here, is approximately 30% between 15 to 24 km. Improvements in the vertical resolution of the retrieval could potentially be improved if measurement could be provided at finer vertical spacing (i.e. 1km). However, vertical gradients in the ozone profile between 15 to 24 km can typical be between 40 and 50%, so a 30% retrieval error could potentially provide useful information. It should be noted that the *a priori* error in all of these retrievals has been assumed to be 100% at all levels, whereas the variability of the ozone concentration in the UTLS region may well be greater than 100%.

Non-linear 2-D retrieval simulations have also been performed with the RAL 2-D retrieval scheme to reproduce a realistic 2-D ozone cross-section from simulated MIPAS measurements in the S6 observing mode for the first microwindow selected in chapter 7. The results of this retrieval are consistent with the linear diagnostics also calculated in this chapter, and it is shown that the retrieval errors (i.e. the square root of the diagonal elements of $\mathbf{S}_x$) decrease as the spacing of the horizontal retrieval grid is increased. The results show that there is potential for the retrieval of horizontal structure along the instrument line-of-sight in the UTLS region of the atmosphere, at least for cloud-free scenarios, with resolutions of 2 km in the vertical and 248 km in the horizontal.

Further work on the 2-D retrieval study would be to include other trace species in the atmosphere (i.e. line absorbers), especially those which have absorption features which interfere with ozone in the spectral regions utilised for these simulations. Although it is always possible to select other ozone microwindows in which such interference is less prominent. The linear diagnostics presented here represent the best possible retrieval sensitivity that could be achieved for the microwindows selected and other assumptions adopted here in this mode, as only the measurement noise is included in $\mathbf{S}_y$. The linear mapping of other errors, especially temperature, will provide further insight into the role of 2-D retrievals of ozone in the lower atmosphere. For the non-linear retrieval simulations, only one microwindow has been used in assessing the potential for using 2-D retrievals of ozone, and including other microwindows should lead to better performance of the retrieval. One issue facing the capabilities for 2-D retrievals, and especially in the UTLS, is the presence of cloud. Further work is required to assess how cloud will affect such a retrieval, and simulations including a representation of cloud will indicate how best to deal with this issue. A possible approach could be to reject limb views in which there is cloud, which could lead to a dramatic reduction in the amount of data available.

To fully assess the benefits of a tomographic approach to retrieving horizontal structure in the atmosphere, the results should be compared to a conventional 1-D retrieval from the 2-D measurements. Previous 2-D retrieval studies (Livesey and Read, 2000; Reburn et al., 1998) have shown that a significant improvement in retrieval accuracy compared to conventional techniques. This comparison for the simulated 2-D retrievals presented for measurements from MIPAS presented in this chapter.

The key point of these non-linear 2-D retrievals is that, for an assumed NESR, one microwindow appears to provide enough precision. This tomographic approach to retrieving geophysical parameters from infrared limb sounders requires considerable investigation, but provides an exciting prospect for the MIPAS special observing mode and possible future missions.

# Chapter 9

# Summary and Further Work

## 9.1 Summary

The aim of this thesis has been to assess the potential of infrared limb emission instruments to sound ozone in the upper troposphere and lower stratosphere region of the Earth's atmosphere. The background chapters have outlined some of the most important issues concerning the distribution of ozone in the UTLS and its chemical, dynamical and radiative processes. There have been a number of satellite instruments dedicated to measuring the distribution of ozone in the atmosphere and monitoring trends, with several more currently operational and scheduled for launch. A key aspect of the latest instruments is the observation of the UTLS with good vertical resolution through FOV and/or spectral resolution. Infrared sounders are particularly important as they can provide such observations in both daytime and nighttime. To assess the potential for sounding ozone in the UTLS, the characteristics of two different instruments have been considered: the Improved Stratospheric And Mesospheric Sounder (ISAMS) experiment on the NASA UARS platform, and the Michelson Interferometer for Passive Atmospheric Sounding (MIPAS) instrument on the ESA ENVISAT-1 platform.

Retrievals of ozone from the ISAMS data are used to demonstrate that it is possible to sound into the lower stratosphere with a reasonable degree of accuracy. One of the main issues is the contamination of the radiance signals by enhanced sulphate aerosol loading of the stratosphere from the eruption of Mt. Pinatubo in 1991. It was shown (Rosen et al., 1992) that this aerosol did not enter into the Arctic polar vortex until mid-January 1992 and omitting corrections for aerosol from the ozone retrieval is shown not to have a serious impact above 46 hPa with an impact of up to 10% at 68 hPa (Figure 5.3). Ozone is retrieved from the ISAMS data with a vector-vector optimal estimation technique for the forty days of data available (December 6 1991 to January 13 1992). The retrieved ozone is compared to other data available from the same period (i.e. the MLS instrument on UARS and ozonesondes launched from Northern Europe, Greenland and Canada) within a low aerosol region defined from the 12.1 $\mu$m aerosol extinction which is one of the ISAMS retrieved products. The comparison to ozonesonde profiles requires that the considerably higher vertical resolution ozonesonde profiles are smoothed with the averaging kernels from the ISAMS ozone retrievals. A profile by profile comparison of the three datasets shows that, within the $1\sigma$ retrieval error bars, there is a reasonable agreement although this agreement degrades as the winter period progresses. This could be due to low temperatures, a small increase in aerosol extinction (even in the low aerosol region) or a combination of both. Comparison of all of the co-located satellite and ozonesonde profiles show reasonable agreement, with most of the data lying on or close to the y = x line. Profiles constrained to be within 200 km and 5 hours of each other are shown to be largely within the $1\sigma$ satellite error bars. The ISAMS ozone shows greater scatter than the MLS ozone and this could also be due to the increased sensitivity of the ISAMS signal to noise, and retrievals, at low temperatures as shown by the comparison of the factor $1/B(\partial B/\partial T)$ at infrared and microwave wavelengths.

A limiting factor on the retrieval of ozone from the ISAMS data could also be the approximations made when representing horizontal gradients along the instrument line-of-sight. Radiative transfer calculations and retrieval simulations for the MIPAS instrument presented in this thesis have been performed with the RAL 2-D forward model FM2D. This model has been developed in such a way as to explicitly integrate the radiative transfer equation along the instrument line-of-sight, as opposed to applying the Curtis-Godson or emissivity growth approximations. Results of radiance spectra calculated by the FM2D are compared to another forward model with the capability for performing 2-D radiative transfer calculations: the Oxford University Reference Forward Model (RFM). The main difference in the physics between these radiative transfer models is in the application of the Curtis-Godson approximation in the RFM. Comparison of radiance calculations for three different atmospheric scenarios (1-D, homogeneous 2-D and inhomogeneous 2-D) show that the two models produce similar results (less than 0.1% difference) in all cases. The impact of a gradient in temperature, pressure and ozone concentration along the instrument line-of-sight has a significant impact on the calculated radiance, although the magnitude of the impact will be dependent on the magnitude of the gradient. Differences between the 1-D and homogeneous 2-D calculations are shown to be negligible (approximately 0.003%) relative to the actual calculated radiance.

The MIPAS instrument is a high spectral resolution FTS and provides wide spectral coverage (including the fundamental vibration-rotation bands of the ozone molecule) with considerably more selectivity than ISAMS (which was a fixed channel radiometer) in the spectral regions in which ozone may be retrieved. In order to make efficient use of the MIPAS data it is necessary to select the optimum spectral regions (or microwindows) for the retrieval of ozone. For the MIPAS instrument, spectral bands A (685 to 970 cm$^{-1}$) and AB (1020 to 1190 cm$^{-1}$) are shown to be where the fundamental vibration bands of the ozone molecule (i.e. $\nu_1$ = 1103, $\nu_2$ = 701 and $\nu_3$ = 1042 cm$^{-1}$) are located, and the ozone microwindow selection is restricted to these two bands. The selection of 1 cm$^{-1}$ wide microwindows across both MIPAS bands is performed by assessing the information content of each in turn and selecting the best one. This is removed from the list and the process repeated until they have all been selected. Microwindow selection was performed for the full altitude range (6 to 68 km) and an altitude range spanning the UTLS (6 to 24 km) with the results showing an improvement in the retrieval random errors for the lower atmosphere over the 6 to 24 km altitude range of almost a factor of two (Figure 7.10). The impact of including the attenuation due to line gases in the atmosphere (in addition to ozone) on the ozone weighting functions does not greatly affect the microwindow selection, with microwindows selected at more or less the same spectral ranges although the ordering is slightly different. The impact of broadband emissions, and particularly CFCs, which are not modelled by the version of the FM2D used for this work is shown to be very small.

One of the most important sources of systematic error in retrievals of ozone utilising the microwindows selected is shown to be the effect of the presence of gradients along the line-of-sight of the order of 1 K per 100 km horizontal temperature gradient. The ability to perform 2-D retrievals leads to the removal of line-of-sight gradients as a source of systematic uncertainty, which is especially desirable in the UTLS where there is considerable variability of the ozone (and temperature) field. 2-D retrievals are dependent on the limb viewing strategy employed in order to provide sufficient horizontal sampling of the atmosphere. In its nominal observing mode, the MIPAS instrument provides a horizontal spacing between profiles of approximately 510 km and is not suitable for such a retrieval, however in the special observing mode S6, the horizontal spacing of profiles is approximately 120 km and this mode is more suitable. Diagnostics calculated for a simulated, linear 2-D retrieval show that there is a trade-off between the precision and the horizontal resolution, i.e. the precision of the retrieval improves as the horizontal resolution degrades relative to the horizontal spacing of the measurements. In the S6 observing mode, the precision for the smallest horizontal retrieval grid spacing (116 km) is greater than that calculated for the 1-D linear retrieval, although a precision better than the 1-D retrieval, between approximately 2 and 15%, is achieved for coarser spacing of the horizontal retrieval grid spacings of 232 (between approximately 2 and 12%) and 348 km (between approximately 2 and 8%).

The ability to reproduce horizontal structure along the instrument line-of-sight from radiance measurements in the S6 observing mode, with a non-linear 2-D retrieval, is shown to be feasible in simulations for a cloud free atmosphere. Simulated results, for a cloud-free, ozone only atmosphere and using one microwindow, show that is possible to retrieve features with good precision and horizontal resolution. As shown for the linear 2-D retrievals, the improvement in precision is dependent on the horizontal retrieval grid spacing.

## 9.2 Further Work

To further the work on the ISAMS ozone retrievals presented in this thesis, a least squares fit (for example) and calculation of correlation coefficients could be used to quantify how well the ISAMS ozone compares to the MLS and ozonesonde data. Further investigations into the definition of the low aerosol region would show how reasonable the assumed threshold is, relative to background stratospheric conditions. Assessment of potential vorticity fields, from meteorological analyses (e.g. ECMWF) could also be considered, to show the consistency of the low aerosol region to the results of Rosen et al. (1992). Investigations into the co-location constraints could also provide some insight into the variability of the ISAMS data. It should be noted, however, that strongly constraining the low aerosol threshold value or co-location could lead to a significant reduction in the amount of comparative data available. Assessment of the information content and degrees of freedom of the ISAMS measurements could provide further quantification. In addition to this, there is also the possibility of performing the retrievals with the LV2VMR retrieval scheme.

The most obvious further work for the MIPAS 1-D retrievals would be to apply the selected microwindows to a retrieval from real MIPAS spectra. However, several assumptions have been made in the selection of these microwindows and, although the results might not be expected to alter significantly, they require further assessment. Firstly, the NESR in each of the MIPAS bands have a pre-calibration value which is uniform across the band, whereas the in-flight measurements of the NESR are generally non-uniform across the band and have lower values by almost a factor two in some cases. In the retrievals presented, the measurement error covariance matrix has been assumed to be diagonal, and only the NESR of the instrument has been included. The assumption of a diagonal error covariance matrix implies that each measurement is independent, whereas in reality there are likely to be correlations between successive measurements, and the off-diagonal elements of the measurement error covariance matrix should take these into account. Secondly, to make the retrievals more realistic, mapping of errors due to the retrieval of temperature, water vapour and other parameters is necessary in the microwindow selection. Inclusion of line absorbers additional to ozone in the atmosphere should also take into account their variability, which has so far been difficult to quantify in the UTLS, in the microwindow selection. An *a priori* error of 100% has been assumed uniformly whereas, in reality, the variability in the ozone field, depending on altitude, latitude and season, will differ from 100%. In the stratosphere, variability about the monthly, latitudinal mean is considerably less than 100% but in the upper troposphere and around the tropopause region, vertical gradients give rise to much larger variability about the mean. Investigation of the prior constraints was beyond the scope of this thesis, but is necessary in providing accurate retrievals. Finally, only mid-latitude daytime atmospheric profiles have only been considered and microwindows selected for other atmospheric scenarios (e.g. tropical, polar winter, etc.) are also required.

For the MIPAS 2-D retrievals, similar assumptions to the 1-D retrievals have been made and further investigation is required before it can be applied to real MIPAS data. Retrievals of temperature and water vapour in 2-D are important as they are likely to be the most significant source of systematic uncertainty in the ozone retrieval for the microwindows selected. One of the most important issues facing the possibility to perform 2-D retrievals is the presence of cloud, as a cloud observed in one tangent path will affect the 2-D retrieval at all intersections with that tangent path. Cloud is spectrally flat across the MIPAS range, and complicates the radiative transfer as it scatters as well as absorbs. Assessment of the impact of clouds on the 2-D retrieval scheme needs to be assessed before this can be applied to real data in the upper troposphere. The aim of the 2-D retrievals presented in this thesis has been to demonstrate the potential for this type of retrieval for the MIPAS instrument, as a development of the retrieval model implemented for the MASTER instrument and described in Siddans et al. (2000b). The application of this retrieval approach to real MIPAS data requires considerable computational effort to process the amount of data with careful attention to handling retrieval system non-linearities so as, for example, to improve convergence (Siddans et al., 2000b).

# Bibliography

Anderson, J. G. and Toon, O. B. (1993). Atmospheric Airborne Stratospheric Expedition II: An overview. *Geophysical Research Letters*, 20(22):2,499–2,503.

Aumann, H. A. et al. (2003). AIRS/AMSU/HSB on the Aqua mission: Design, science objectives, data products, and processing systems. *IEEE Transactions on Geoscience and Remote Sensing*, 41(2):253–264.

Bailey, P. L. et al. (1996). Comparison of Cryogenic Limb Array Etalon Spectrometer (CLAES) ozone measurements with correlative measurements. *Journal of Geophysical Research*, 101(D6):9,737–9,756.

Barath, F. T. et al. (1993). The upper atmosphere research satellite microwave limb sounder instrument. *Journal of Geophysical Research*, 98(D6):10,751–10,762.

Baron, P., Merino, F., and Murtagh, D. (2001). Simultaneous retrievals of temperature and volume mixing ratio constituents from non-oxygen Odin submillimeter radiometer bands. *Applied Optics*, (33):6,102–6,110.

Beer, R., Glavich, T. A., and Rider, D. M. (2001). Tropospheric emission spectrometer for the Earth Observing System's Aura satellite. *Applied Optics*, 50(15):2,356–2,367.

Bernath, P. (2000). Atmospheric Chemistry Experiment (ACE): an Overview. In

Demaison, J., Sarka, K., and Cohen, E. A., editors, *Spectroscopy from Space*. Kluwer Academic Publishers.

Brasseur, G. P. et al. (1998). European scientific assessment of the atmospheric effects of aircraft emissions. *Atmospheric Environment*, 32(13):2,327–2,422.

Bruce, R. E. (1977). Experimental study of the relationship between radiosonde temperature and satellite derived temperatures. *Monthly Weather Review*, 105:493–496.

Bruhl, C. et al. (1996). Halogen Occultation Experiment ozone channel validation. *Journal of Geophysical Research*, 101(D6):10,217–10,240.

Carlotti, M., Dinelli, B. M., Raspollini, P., and Ridolfi, M. (2001). Geo-fit approach to the analysis of limb-scanning satellite measurements. *Applied Optics*, 40(12):1,872–1,885.

Clough, S. A., Kneizysm, F. X., and Davies, R. W. (1989). Line shape and the water vapour continuum. *Atmospheric Research*, 23(3-4):229–241.

Connor, B. J. et al. (1996). Ozone in the middle atmosphere as measured by the Improved Stratospheric And Mesospheric Sounder. *Journal of Geophysical Research*, 101(D6):9,831–9,841.

Connor, B. J. and Rodgers, C. D. (1989). A comparison of retrieval methods: Optimal estimation, onion-peeling, and a combination of the two. In *Advances in Remote Sensing Retrieval Methods*, pages 271–281.

Crutzen, P. J., Lawrence, M. G., and Poschl, U. (1999). On the background photochemistry of tropospheric ozone. *Tellus A*, 51(1):123–146.

Cunnold, D. M. et al. (1989). Validation of SAGE-II ozone measurements. *Journal of Geophysical Research*, 94(D6):8,447–8,460.

Dudhia, A. (1996). Development of a reference forward model algorithm for the simulation of MIPAS atmospheric limb emission spectra. ESTEC 11886/96/NL/GS.

Dudhia, A. (1999a). Assessment of horizontal inhomogeneities. Technical report, University of Oxford. Task report on Task 2.3 of ESA contract 12055/96/NL/CN.

Dudhia, A. (1999b). *MIPAS RFM Software User's Manual*. University of Oxford. http://www.atm.ox.ac.uk/RFM/sum.html.

Dudhia, A. (2001). *MWMAKE (Microwindow Selection) - User's Guide*. University of Oxford. http://www.atm.ox.ac.uk/RFM/mwmake.html.

Dudhia, A., Jay, V. L., and Rodgers, C. D. (2002). Microwindow selection for high-spectral-resolution sounders. *Applied Optics*, 41(18):3,665–3,673.

Dudhia, A. and Livesey, N. (1996). Validation of temperature measurements from the improved stratospheric and mesospheric sounder. *Journal of Geophysical Research*, 101(D6):9,795–9,809.

Endeman, M., Gare, P., Langen, J., Nett, H., and Readings, C. J. (2000). MIPAS - An Envisat instrument for atmospheric chemistry and climate research. *ESA Bulletin*, 101.

Eyre, J. R. (1990). The information content of data from satellite sounding systems - A simulation study. *Quarterly Journal of the Royal Meteorological Society*, 116(492):401–434.

Farman, J. C., Gardiner, B. G., and Shanklin, J. D. (1985). Large losses of total ozone in Antarctica reveal seasonal $\mathrm{ClO}_x/\mathrm{NO}_x$ interaction. *Nature*, 315:207–210.

Fishbein, E. F. et al. (1996). Validation of UARS Microwave Limb Sounder temperature and pressure measurements. *Journal of Geophysical Research*, 101(D6):9,983–10,016.

Flaud, J. M. and Bacis, R. (1998). The ozone molecule: Infrared and microwave spectroscopy. *Spectrochimica Acta Part A*, 54(1):3–16.

Flaud, J. M. et al. (2003). Ozone absorption around 10 $\mu$m. *Journal of Geophysical Research*, 108(D9):4269. doi:10.1029/2002JD002755.

Forster, P. M. d. F. and Shine, K. P. (1997). Radiative forcing and temperature trends from stratospheric ozone changes. *Journal of Geophysical Research*, 102(D9):10,841–10,855.

Froidevaux, L. et al. (1996). Validation of UARS Microwave Limb Sounder ozone measurements. *Journal of Geophysical Research*, 101(D6):10,017–10,060.

Froidevaux, L. et al. (1997). UARS MLS data quality document: Version 4 data. Technical report, JPL.

Gauss, M. et al. (2003). Radiative forcing in the 21st century due to ozone changes in the troposphere and lower stratosphere. *Journal of Geophysical Research*, 108(D9). 4292.

Gille, J. C. and House, F. B. (1971). On the inversion of limb and radiance measurements I: Temperature and thickness. *Journal of the Atmospheric Sciences*, 28:1,427–1,442.

Harries, J. E. (1997). Atmospheric radiation and atmospheric humidity. *Quarterly Journal of the Royal Meteorological Society*, 123(544):2,173–2,186.

Holton, J. R. et al. (1995). Stratosphere-troposphere exchange. *Reviews of Geophysics*, 33(4):403–439.

Hoogen, R. et al. (1999). $O_3$ Profiles from GOME satellite data - I: Comparison with ozonesonde measurements. *Physics and Chemistry of the Earth, Part C*, 24(5):447–452.

IPCC (2001). *Climate Change 2001: The Scientific Basis*. Cambridge University Press.

Ivanov, S. V. and Panchenko, V. Y. (1994). Infrared and microwave spectroscopy of ozone: Historical aspects. *Physics-Uspekhi*, 37(7):677–695.

Jacob, D. J. et al. (2002). Atmospheric budget of acetone. *Journal of Geophysical Research*, 107(D10). doi:10.1029/2001JD000694.

Jay, V. L. (2000). *Remote Sounding of the Atmosphere by High Spectral Resolution Spectroscopy*. PhD thesis, University of Oxford.

Kemnitzer, H. et al. (2002). Trace gas retrievals including horizontal gradients. *Advance in Space Research*, 29(11):1,631–1,636.

Kerridge, B. J. et al. (2002). Consideration of mission studying chemistry of the utls. Technical report, ESTEC. Progress Report 2 for ESTEC Contract 15457/01/ML/MM.

Kidder, S. Q. and Vonder Haar, T. H. (1995). *Satellite Meteorology: An Introduction*. Academic Press.

Krueger, A. J. et al. (1980). Satellite ozone measurements. *Philosophical Transactions of the Royal Society of London A*, 296:191–204.

Lambert, A. et al. (1996). Validation of aerosol measurements from the improved stratospheric and mesospheric sounder. *Journal of Geophysical Research*, 101(D6):9,811–9,830.

Lary, D. J. (1997). Catalytic destruction of stratospheric ozone. *Journal of Geophysical Research*, 102(D17):21,515–21,526.

Livesey, N. J. et al. (2003). The UARS Microwave Limb Sounder version 5 data set: Theory, characterisation and validation. *Journal of Geophysical Research*, 108(D13). 4378.

Livesey, N. J. and Read, W. G. (2000). Direct retrieval of line-of-sight atmospheric structure from limb sounding observations. *Geophysical Research Letters*, 27(6):891–894.

Logan, J. A. et al. (1999). Trends in the vertical distribution of ozone: A comparison of two analyses of ozonesonde data. *Journal of Geophysical Research*, 104(D21):26,373–26,399.

Louet, J. (2001). The Envisat Mission and System. *ESA Bulletin*, 106.

Marks, C. J. and Rodgers, C. D. (1993). A retrieval method for atmospheric composition from limb emission measurements. *Journal of Geophysical Research*, 98(D8):14,939–14,953.

McNally, A. P. (1990). *Satellite Sounding of Tropospheric Temperature and Humidity*. PhD thesis, University of Oxford.

Menke, W. (1984). *Geophysical data analysis: Discrete inverse theory*. Academic Press, New York.

Miller, A. J. (1989). A review of satellite observations of atmospheric ozone. *Planetary and Space Science*, 37(12):1,539–1,554.

NASA (1978). *The Nimbus 7 Users' Guide*. National Aeronautic and Space Administration.

NASA (1999). *1999 EOS Reference Handbook*. National Aeronautic and Space Administration. NP-1999-08-134-GSFC.

Noel, S. et al. (2002). Nadir, limb and occultation measurements with SCIAMACHY. *Advances in Space Research*, 29(11):1,819–1,824.

Peckham, G. E. (1974). The information content of remote measurements of atmospheric temperature by satellite infrared radiometry and optimum radiometer configurations. *Quarterly Journal of the Royal Meteorological Society*, 100:406–419.

Penner, J. E., Lister, D. H., Griggs, D. J., Dokken, D. J., and McFarland, M., editors (1999). *Aviation and the Global Atmosphere. A Special Report of Working Groups I and III of the Intergovernmental Panel on Climate Change (IPCC)*. Cambridge Univ. Press, New York.

Press, W. H., Flannery, B. P., Teulosky, S. A., and Vetterling, W. T. (1993). *Numerical Recipes in FORTRAN 77: Volume 1 of Fortran Numerical Recipes: The Art of Scientific Computing*. Cambridge University Press.

Pyle, J. A. et al. (1994). An overview of the EASOE campaign. *Geophysical Research Letters*, 21(13):1,191–1,194.

Rabier, F., Fourrie, N., Chafai, D., and Prunet, P. (2002). Channel selection methods for the Infrared Atmospheric Sounding Interferometer radiances. *Quarterly Journal of the Royal Meteorological Society*, 128(581):1,011–1,027.

Ratier, G. et al. (1999). GOMOS: ENVISAT's contribution to measuring long-term trends in ozone and other trace gases. *ESA Bulletin*, 97.

Reburn, W. J., Siddans, R., Kerridge, B. J., et al. (1998). Study on upper troposphere / lower stratosphere sounding: Final report. Technical report, ESTEC. ESA Contract 12053/97/NL/CN.

Remsberg, E. E. et al. (1984). The validation of Nimbus-7 LIMS measurements of ozone. *Journal of Geophysical Research*, 89(ND4):5,161–5,178.

Rodgers, C. D. (1990). Characterisation and error analysis of profiles retrieved from remote sounding measurements. *Journal of Geophysical Research*, 95(D5):5,587–5,595.

Rodgers, C. D. (1998). Information content and optimisation of high spectral resolution remote measurements. *Advances in Space Research*, 21(3):361–367.

Rodgers, C. D. (2000). *Inverse Methods for Atmospheric Sounding: Theory and Practice*. World Scientific.

Rodgers, C. D., Wells, R. J., Grainger, R. G., and Taylor, F. W. (1996). Improved stratospheric and mesospheric sounder validation: General approach and in-flight radiometric calibration. *Journal of Geophysical Research*, 101(D6):9,775–9,793.

Rosen, J. M. et al. (1992). Penetration of Mt. Pinatubo aerosols into the North polar vortex. *Geophysical Research Letters*, 19(17):1,751–1,754.

Rosier, S. M. and Shine, K. P. (2000). The effect of two decades of ozone change on stratospheric temperatures as indicated by a general circulation model. *Geophysical Research Letters*, 27:2,617–2,620.

Rothman, L. S. et al. (1998). The HITRAN molecular spectroscopic database and HAWKS (HITRAN workstation): 1996 edition. *Journal of Quantitative spectroscopy and Radiative Transfer*, 60(5):665–710.

Rusch, D. W. et al. (1997). Validation of POAM ozone measurements with coincident MLS, HALOE and SAGE II observations. *Journal of Geophysical Research*, 102(D19):23,615–23,627.

Seinfeld, J. H. and Pandis, S. N. (1998). *Atmospheric Chemistry and Physics: From Air Pollution to Climate Change*. Wiley-Interscience.

Siddans, R. et al. (1997). Height-resolved ozone information in the troposphere and lower stratosphere from GOME. In *Third ERS Symposium on Space at the Service of Our Environment*, volume II, pages 615–620. ESA. SP-414.

Siddans, R., Reburn, W. J., and Kerridge, B. J. (2000a). 2-D MM-wave forward modelling and retrieval simulations. In *Proceedings of the second International Workshop on Millimetre and Sub-mm Wave Radiative Transfer Modelling*.

Siddans, R., Reburn, W. J., and Kerridge, B. J. (2000b). Critical assessments in millimetre-wave atmospheric limb sounding: Final report. Technical report, ESTEC.

Smit, H. G. J. (2002). Ozone Sondes. In *Encyclopedia of Atmospheric Sciences*, pages 1,469–1,476. Academic Press.

SPARC (1998). *Assessment of Trend in the Vertical Distribution of Ozone*. World Meteorological Organization. WCRP-SPARC, Report No. 1.

Stephens, G. L. (1994). *Remote Sensing of the Lower Atmosphere: An Introduction*. Oxford University Press.

Stohl, A. et al. (2003). Stratosphere-troposphere exchange: A review and what we have learned from STACCATO. *Journal of Geophysical Research*, 108(D12):8516.

Sugita, T. et al. (2002). Validation of ozone measurements from the Improved Limb Atmospheric Spectrometer. *Journal of Geophysical Research*, 107(D24). art. no. 8212.

Taylor, F. W. (1983). *Spectrometric Techniques*, volume III, chapter 3, pages 137–197. Academic Press.

Taylor, F. W. et al. (1993). Remote sensing of atmospheric structure and composition from space: The ISAMS experiment on UARS. *Journal of Geophysical Research*, 98(D6):10,799–10,814.

Taylor, F. W., Lambert, A., Grainger, R. G., Rodgers, C. D., and Remedios, J. J. (1994). Properties of Northern hemisphere polar stratospheric clouds and volcanic aerosol in 1991/92 from UARS/ISAMS satellite measurements. *Journal of the Atmospheric Sciences*, 51(20):3,019–3,026.

von Clarmann, T. and Echle, G. (1998). Selection of optimised microwindows for atmospheric spectroscopy. *Applied Optics*, 37(33):7,661–7,669.

von Clarmann, T. et al. (2003). Modelling of atmospheric mid-infrared radiative transfer: the AMIL2DA algorithm inter-comparison experiment. *Journal of Quantitative Spectroscopy and Radiative Transfer*, 78:381–407.

von Savigny, C. et al. (2003). Stratospheric ozone profiles retrieved from limb scattered sunlight radiance spectra measured by the OSIRIS instrument on the Odin satellite. *Geophysical Research Letters*, 30(14):1755. doi:10.129/2002GL016401.

Wang, H. J., Cunnold, D. M., Froidevaux, L., and Russell, J. M. (1999). A reference model for middle atmospheric ozone in 1992-93. *Journal of Geophysical Research*, 104(D17):21,629–21,643.

Waters, J. W. et al. (1999). The UARS and EOS Microwave Limb Sounder (MLS) experiments. *Journal of the Atmospheric Sciences*, 56:194–218.

Wayne, R. P. (2000). *Chemistry of Atmospheres*. Oxford University Press, third edition.

WMO (1999). *Scientific Assessment of Ozone Depletion: 1998*. *Global Ozone Research and Monitoring Project*, *Report No. 44*. Geneva.

WMO (2003). *Scientific Assessment of Ozone Depletion: 2002*. *Global Ozone Research and Monitoring Project*, *Report No. 47*. Geneva.

Worden, J. R., Bowman, K., and Jones, D. B. A. (2003). Characterisation of atmospheric profile retrievals from limb sounding observations of an inhomogeneous atmosphere. *In press*.